AVERTISSEMENT

Ce document est le fruit d'un long travail approuvé par le jury de soutenance et mis à disposition de l'ensemble de la communauté universitaire élargie.

Il est soumis à la propriété intellectuelle de l'auteur. Ceci implique une obligation de citation et de référencement lors de l'utilisation de ce document.

D'autre part, toute contrefaçon, plagiat, reproduction illicite encourt une poursuite pénale.

Contact : ddoc-theses-contact@univ-lorraine.fr

LIENS

Code de la Propriété Intellectuelle. articles L 122. 4
Code de la Propriété Intellectuelle. articles L 335.2- L 335.10
http://www.cfcopies.com/V2/leg/leg_droi.php
http://www.culture.gouv.fr/culture/infos-pratiques/droits/protection.htm

UNIVERSITÉ DE LORRAINE

NORTHEASTERN UNIVERSITY

DISSERTATION

Presented at
Université de Lorraine and Northeastern University

Meishuai LIU　刘梅帅

To obtain the doctor's degree of
University of Lorraine and Northeastern University

SPECIAL FIELD: Engineering Sciences

OPTION: Materials Science

Study on microstructural and crystallogarphic characteristics of phase transformation induced by ECP in annealed Cu-40%Zn alloy

Defended on July 19th, 2019 in front of the jury:

Werner Skrotzki	Professor	Technische Universität Dresden, Germany	Reviewer & Jury member
Zhanjie Wang	Professor	Shenyang University of Technology, China	Reviewer
Gang Ji	Chargé de recherche et Doctor HDR	Université de Lille, France	Jury member
Zheng Liu	Professor	Shenyang University of Technology, China	Jury member
Pingli Mao	Professor	Shenyang University of Technology, China	Jury member
Yudong Zhang	Doctor HDR	Université de Lorraine, France	Supervisor
Benoît Beausir	Doctor	Université de Lorraine, France	Co-Supervisor
Xiang Zhao	Professor	Northeastern University, China	Supervisor
Xinli Wang	Associate Professor	Northeastern University, China	Co-Supervisor
Claude Esling	Professor	Université de Lorraine, France	Invited

Laboratoire d'Étude des Microstructures et de Mécanique des Matériaux, LEM3

7 rue Félix Savart, 57070 Metz, France

Abstract

A thorough investigation has been conducted on the microstructural and crystallographic features of Electric Current Pulse (ECP) treated Cu-40%Zn alloys. The phase transformation orientation relationship (OR) and its correlation with crystal defects have been studied and the formation mechanisms of ECP induced crystal defects in the parent phase and the sub-structures in the β precipitates were also analyzed.

The α to β heating phase transformation can be induced by ECP treatment with the formation of fine β precipitates that can be remained to the room temperature. With the increase of the electric current density, the amount of precipitates is increased and the formation sites increase from α grain boundaries to grain interiors. The β precipitates follow different ORs depending on the formation site. The grain boundary β phase obeys the Kurdjumov-Sachs (K-S) OR; whereas the intragranular β respects the Nishiyama-Wasserman (N-W) OR. In the former sites, the $\{111\}_\alpha/<1\bar{1}0>_\alpha$ dislocations are observed, whereas in the latter, the $\{111\}_\alpha/<11\bar{2}>_\alpha$ stacking faults are found. Transformation strain analyses revealed that under the K-S OR the maximum lattice deformation required is a shear on the $\{111\}_\alpha/<1\bar{1}0>_\alpha$ slip system, whereas under the N-W OR the maximum deformation is a shear on the $\{111\}_\alpha/<11\bar{2}>_\alpha$ system. Thus the existing $\{111\}_\alpha/<1\bar{1}0>_\alpha$ dislocations along the α grain boundaries provide pre-strain required by the transformation via the K-S path, whereas the $\{111\}_\alpha/<11\bar{2}>_\alpha$ stacking faults boarded by $\{111\}_\alpha/<11\bar{2}>_\alpha$ partial dislocations offer pre-strain facilitating the transformation via the N-W path.

Different types of crystal defects are formed in the α matrix by the ECP treatments depending on the current density. At low density, large amount of $\{111\}_\alpha/<11\bar{2}>_\alpha$ stacking faults and then nano twins are produced in the α matrix. At high density, dislocation nets are formed near the β precipitates that are composed of edge typed $\{111\}_\alpha/<1\bar{1}0>_\alpha$ perfect dislocations and the Frank typed dislocations. The volume misfit between the α and the β phase

analyzed with transformation deformation reveals that the transformation from α to β requires an expansion along $[1\bar{1}0]_\alpha$ direction and a contraction along $[111]_\alpha$ direction. The former results in the appearance of the $\{111\}_\alpha/<1\bar{1}0>_\alpha$ edge typed dislocation arrays in front of the $\{3\bar{1}1\}_\alpha$ broad faces and the latter induces the formation of the Frank typed dislocations in front of the $\{121\}_\alpha$ broad faces. Thus, dislocation nets formed along the edges of the broad faces of the β precipitates where the two kinds of dislocations meet.

Furthermore, the β precipitates contain two kinds of nano-sized and diffuse atomic clusters with the η structure obeying the Burgers OR and with the ω structure obeying the Blackburn OR with the β matrix. They were each formed through a two-stepped atomic displacement. For the η structure, the first step is the atomic shuffle of each second $\{110\}_\beta$ plane in the $<1\bar{1}0>_\beta$ direction and the second is a structure change mainly by a shear on the $\{1\bar{1}2\}_\beta/<\bar{1}11>_\beta$. For the ω structure, the first is an atomic shuffle on each second and third $\{11\bar{2}\}_\beta$ plane in the $\pm[111]_\beta$ directions and then normal strains in three mutually perpendicular directions ($<111>_\beta$, $<11\bar{2}>_\beta$ and $<1\bar{1}0>_\beta$). The concomitant appearance of the two structures lies in the fact that the volume increase accompanying the η formation can be canceled by the volume decrease accompanying the ω distortion, which minimizing the transformation strain energy.

The results of this work provide fundamental information on the Cu-40%Zn alloys for interpreting the impact of the crystal defects on the solid phase transformation ORs, on the formation of various types of crystal defects induced by the ultra-rapid phase transformation and on the formation mechanisms of sub structures in the product phase.

Keywords: Cu-40%Zn alloys; Orientation relationship; Phase transformation; Crystal defect; Crystallography; Deformation gradient tensor.

Résumé

Ce travail porte sur les caractéristiques microstructurales et cristallographiques des alliages Cu-40%Zn traités par Electric Current Pulse (ECP) La relation d'orientation (RO) de transformation de phase et sa corrélation avec les défauts cristallins ont été étudiés. Les mécanismes de formation des défauts cristallins dans la phase mère et des sous-structures dans les précipités β induit par L'ECPont également été étudiés.

La transformation de la phase α en β peut être induite par un traitement ECP avec formation de précipités fins β pouvant persister à température ambiante. Avec l'augmentation de la densité de courant électrique, la quantité de précipités et les sites de formation augmentent des joints de grains α à l'intérieur des grains. Les précipités β suivent différentes RO en fonction du site de formation. Les joints de grains β sont en RO Kurdjumov-Sachs (KS); tandis que les β intragranulaires sont en Nishiyama-Wasserman (NW). Dans les premiers sites, on observe des dislocations $\{111\}_\alpha/<1\bar{1}0>_\alpha$, alors que dans les seconds, les fautes d'empilements $\{111\}_\alpha/<11\bar{2}>_\alpha$ sont présentes. Les analyses de déformation de transformation ont révélé que, en RO KS, la déformation maximale du réseau requise est un cisaillement sur le système $\{111\}_\alpha/<11\bar{2}>_\alpha$, tandis qu'en NW, la déformation maximale correspond à un cisaillement sur le système $\{111\}_\alpha/<11\bar{2}>_\alpha$. Ainsi, les dislocations $\{111\}_\alpha/<1\bar{1}0>_\alpha$ existants le long des joints de grains α fournissent la précontrainte requise par la transformation KS, alors que les fautes d'empilement $\{111\}_\alpha/<11\bar{2}>_\alpha$ entourées par les dislocations partielles $\{111\}_\alpha/<11\bar{2}>_\alpha$ offrent une précontrainte facilitant la transformation NW.

Différents types de défauts cristallins sont formés dans la matrice α par les traitements ECP en fonction de la densité de courant. À faible densité, une grande quantité de fautes d'empilement $\{111\}_\alpha/<11\bar{2}>_\alpha$, puis des nano-mâcles sont produites dans la matrice α. A haute densité, des réseaux de dislocations sont formés à proximité des précipités β composés de dislocations coins parfaites $\{111\}_\alpha/<1\bar{1}0>_\alpha$ et des dislocations de Frank. La différence de

volume entre le phases α et β analysée avec la déformation de transformation révèle que cette dernière nécessite une dilatation dans la direction $[1\bar{1}0]_\alpha$ et une contraction dans la direction $[111]_\alpha$. La première entraîne l'apparition de dislocations coins $\{111\}_\alpha/<1\bar{1}0>_\alpha$ devant les larges faces $\{3\bar{1}1\}_\alpha$ et la dernière induit la formation des dislocations de Frank devant les larges faces $\{121\}_\alpha$. Ainsi, des réseaux de dislocations se forment le long des bords des grandes faces des précipités β où les deux types de dislocations se rencontrent.

De plus, les précipités β contiennent deux types d'agrégats atomiques de taille nanométrique de structure η en RO Burgers et de structure ω en RO Blackburn avec la matrice β. Ils ont été formés par un déplacement atomique en deux étapes. Pour la structure η, la première étape est le brassage atomique de chaque second plan $\{110\}_\beta$ dans la direction $<1\bar{1}0>_\beta$ et la seconde consiste en un changement de structure principalement par un cisaillement selon $\{1\bar{1}2\}_\beta/<\bar{1}11>_\beta$. Pour la structure ω, le premier est un mélange atomique sur chaque deuxième et troisième plan $\{11\bar{2}\}_\beta$ dans les directions $\pm[111]_\beta$, puis des déformations normales dans trois directions perpendiculaires ($<111>_\beta$, $<11\bar{2}>_\beta$ et $<1\bar{1}0>_\beta$). L'apparence concomitante des deux structures réside dans le fait que l'augmentation de volume accompagnant la formation de η peut être annulée par la diminution de volume accompagnant la distorsion ω, ce qui minimise l'énergie de déformation de transformation.

Ce travail fournit des informations fondamentales sur les alliages Cu-40%Zn pour interpréter l'impact des défauts sur les relations d'orientation de transformations en phase solide, sur la formation de divers types de défauts induits par la transformation de phase ultra-rapide ainsi que sur les mécanismes de formation des sous-structures des phases produites.

Mots clés: Alliages Cu-40%Zn; Relation d'orientation; Transformation de phase; Défauts cristallins; Cristallographie; Tenseur gradient de déformation.

List of the frequently-used abbreviations

ECP	Electric Current Pulse
η_1	Twinning direction
γ	Magnitude of shear
K_1	Twinning plane
OR	Orientation relationship
XRD	X-ray diffraction
SEM	Scanning electron microscope
EBSD	Electron backscatter diffraction
TEM	Transmission electron microscope
SAED	Selected area electron diffraction
STEM	Scanning transmission electron microscope
HAADF	High-angle annular dark field
EPMA	Electron probe microanalysis

Contents

Abstract ..... **I**

Résumé ..... **III**

List of the frequently-used abbreviations ..... **V**

Contents ..... **VII**

Chapter 1 Literature review **1**

1.1 General introduction 1

1.2 The Electric Current Pulses (ECP) technology 1

1.2.1 Introduction 1

1.2.2 The phase transformation induced by ECP 2

1.3 Crystal defect associated solid-state phase transformation 7

1.3.1 Basic crystal defects of metallic materials 7

1.3.2 The effect of the defects on the phase transformation 8

1.3.3 The dislocation mechanism on the phase transformation 11

1.3.4 Crystal defect type associated transformation OR selection 15

1.4 Phase transformations in Cu-Zn alloys 17

1.5 Content of the present work 18

Chapter 2 Experimental and calculation methods **21**

2.1 Experimental details 21

2.1.1 Alloy preparation and heat treatment 21

2.1.2 ECP treatments 22

2.1.3 X-ray diffraction measurement 24

2.1.4 Microstructural characterization 24

2.1.5 Chemical composition analysis 25

2.2 Basic crystallographic calculations 25

2.2.1 Coordinate system 25

2.2.2 Coordinate transformation and orientation relation 26
2.2.3 Stereographic projection 32
2.2.4 Deformation gradient tensor 33
2.2.5 Trace analysis method 36
2.2.6 Twinning elements 38
2.2.7 Hexagonal coordinates 39
Chapter 3 Microstructure and crystallographic characteristics of Cu-40％Zn alloy after the ECP treatments 41
3.1 Introduction 41
3.2 Experimental 41
3.3 Results 42
3.3.1 Phase constituents and lattice constants 42
3.3.2 Microstructure characteristics 43
3.3.3 Chemical composition distribution characteristics 47
3.3.4 Orientation relationship (OR) between α/ β 48
3.3.5 Morphology of intragranular β (β_{GI}) 52
3.4 Discussion 54
3.4.1 The thermal effect of the ECP 55
3.4.2 The electrical effect of the ECP 55
3.4.3 The lattice strain effect 57
3.5 Summary 60
Chapter 4 Crystal defects produced by α to β phase transformation during ECP in Cu-40％Zn alloy 63
4.1 Introduction 63
4.2 Experimental 63
4.3 Results 64
4.3.1 Microstructural characteristics 64
4.3.2 Crystal defect characteristics 65

4.4 Discussion 76
4.5 Summary 82
Chapter 5 Sub-structure of β precipitates formed by ECP treatment in Cu-40％Zn alloy 83
5.1 Introduction 83
5.2 Experimental 83
5.3 Results 84
5.3.1 Microstructural characteristics 84
5.3.2 Identification of sub structures in β precipitates 85
5.3.3 Identification of atomic shuffling and displacement system to realize the structure change 92
5.3.4 Origin of concomitant formation of the two hexagonal structures 97
5.4 Summary 99
Chapter 6 Conclusions and Perspectives 101
6.1 Conclusions 101
6.2 Perspectives 103
References 105
Publication list 121
I: Publications in international journals 121
II: Contributions to International Conferences 122
Acknowledgements 123

Chapter 1 Literature review

1.1 General introduction

The metallic materials have been widely used in industry due to its superior mechanical properties and physical properties, such as high strength, high plasticity, high electrical conductivity and so on. With the development of the science and technology, there are higher requirements on the performance of metallic materials. So, it is required to develop new technology to improve the performance of these materials.

As we known, metallic materials properties are deeply affected by its internal factors, such as the chemical composition, the structure, the defects, the phase distribution, the morphology and so on. The crystal defects caused by the treatment (such as heat treatment, electric treatment and so on) are the direct factors to influence materials properties in production and in practical applications. In addition, the non-equilibrium transformation usually plays an important role to change the microstructure during the process of the materials preparation.

In recent years, the non-equilibrium technologies (electric field and electric current) in materials preparation are used in the manufacturing process [1-5]. This kind of technology can produce high density energy during a very short time in the reaction systems. Thus, some process and structures could be obtained which are difficult to obtain in the equilibrium state to endow the treated materials with specific properties. Due to such specific feature of the non-equilibrium treatment technologies, lots of studies have been conducted on the microstructure evolution of the treated materials.

1.2 The Electric Current Pulses (ECP) technology

1.2.1 Introduction

Since 1963, when Troitskii and Lichtman first reported that the movement of electrons in a metal crystal may interact with dislocations [6], the electric current pulse (ECP) treatment as a relatively new kind of non-equilibrium processing techniques has attracted increasing

attention and been widely explored in the field of materials science and engineering. It had been carried out on many metals and alloys including Cu-based alloys [7, 8], steels [9, 10], titanium alloys [11, 12], iron-based amorphous alloys [13, 14], aluminum alloys [15], magnesium alloys [16, 17] and metallic glass of various compositions [18]. Throughout the research in this domain, many different physical effects possessed by the electric current have been observed, such as the electromigation effect, the electroplastic effect, the Joule heating effect and the skin effect. Until now, the ECP has been successfully used to realize the phase transformation [31-64], the recrystallization [19-27], the crack healing [28], the electroplasticity [29, 30] and so on in a number of metals and alloys.

1.2.2 The phase transformation induced by ECP

High density ECP treatment as an effective, high-speed, and short duration approach to heat a bulk material up to a high temperature. Many studies have demonstrated the capacity for ECP treatment to realize the phase transformation, such as some investigations into the effects of electric current on solid state phase transformations in metals [31-33].

In the 90s, many theoretical investigations have been developed on the effect of electric current on the phase transformation [34-41]. Yu *et al.* studied theoretically the thermodynamics of phase transition of the current-carrying conductors of which the transitions are accompanied by a sharp change of the electrical conductivity [34-38]. They proposed that the effect of the electric current on the phase transformation is attributed to the Joule heating, the thermodynamic pressure and the electric conductivities of the parent and the product phase. It is demonstrated that the electric current promoted the formation of the phase with a higher electric conductivity and prevented the formation of the phase with a lower electric conductivity during the phase transformation process. Then Qin *et al.* studied and calculated the nucleation rate in metallic media with and without the pulse electric current, the relationship between electric current and the undercooling, the temperature distribution due to pulse electric current using the theory of thermodynamics and electrodynamics of continuous media [39-41]. It is suggested that the electric current can increase nucleation rate by decreasing the thermodynamic barrier and thus can refine the microstructure during solidification. On this basis, Zhou *et al.*

further studied the influence of the ECP on the nucleation rate in the solid-state phase transformation [42-44]. They consider that the effect of the electric current on the phase transformation lies in the different electric current distribution in the parent and product phase due to their different electric conductivities. **Fig. 1.1** showed a schematic illustration of the electric current distribution in the parent and in the product phase [45]. In the early stage during

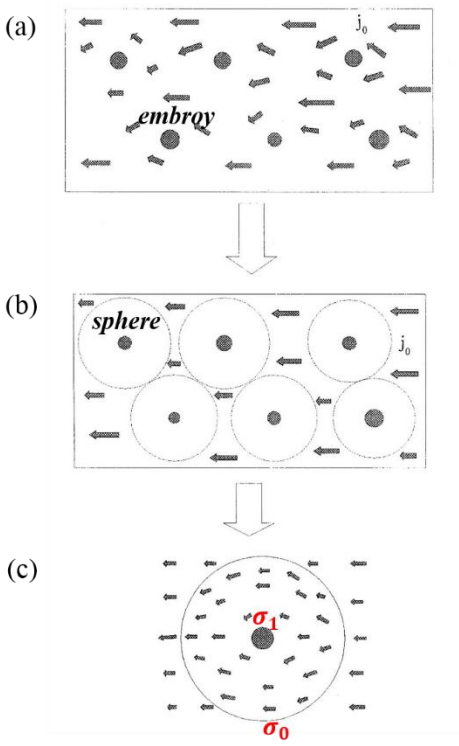


Fig. 1.1 schematic illustration for the current distribution of the parent phase σ_0 and product phase σ_1 [45].

the phase transformation process, lots of embryo formed with small volume compared with the matrix resulting the current distribution inhomogeneous in **Fig. 1.1 (a)**. Considering that a sphere could be built where the embryo as the center and the distance between the center and the nearest neighbor embryo as the half radius in **Fig. 1.1 (b)**. Due to the radius of the sphere larger than the embryo, the matrix and the surface of the sphere is less effected by the embryo. Thus, the current distribution is uniform in the system after the renormalization. In that case, only the current distribution within the sphere should be considered. When the current j_0 passed, the current distribution are changed depending on the electric conductivity of parent phase σ_0 and product phase σ_1 as seen **Fig. 1.1 (c)**. On the basis of the model, the non-equilibrium phase transformation theory induced by the ECP treatment can be establishment [34-41].

Following the above theoretical model, the effects of the ECP on microstructure evolution of metals and alloys were systematically studied. The authors reported that a refined microstructure could be formed in Cu-Zn alloys, steels, superduralumin alloys and TIC/NiCr cermets by applying high current ECP in their solid state [42, 43, 46-49]. It was thought that the microstructure changes were related to a solid-state phase transformation. Those experimental results were in good agreement with the theoretical model that electric current can increase nucleation by decreasing the thermodynamic barrier during the phase transformation process. In addition, high heating rate and high cooling rate, very short treating time are also the main factors for the formation of the refined microstructure as indicated by Zhou *et al.* [42]. The authors described the grain refinement process using a schematic illustration as shown in **Fig. 1.2**.

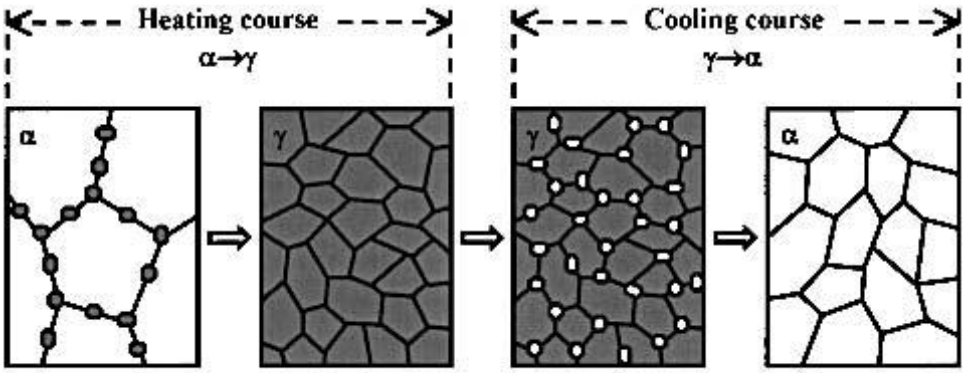


Fig. 1.2 Schematic illustration for grain refinement [42].

Further research carried out by Zhou *et al.* showed that the effect of rapid heating or rapid cooling alone is not sufficient to induce phase transformation in a single α-phased Cu-Zn alloys [44]. To prove the role of high heating and cooling rate on nucleation during phase transformation, they made a comparison of the effect of ECP with that of a pulsed laser with equivalent heating rate. It was evidenced that with an ECP treatment the number of nuclei during the phase transformation could be dramatically enhanced and the precipitation nucleation was more homogeneous, but no microstructural changes were observed in the laser treated samples as shown in **Fig. 1.3**. So, the increased nucleation rate did not result from the effect of rapid heating or rapid cooling during the ECP but resulted from the electric current itself.

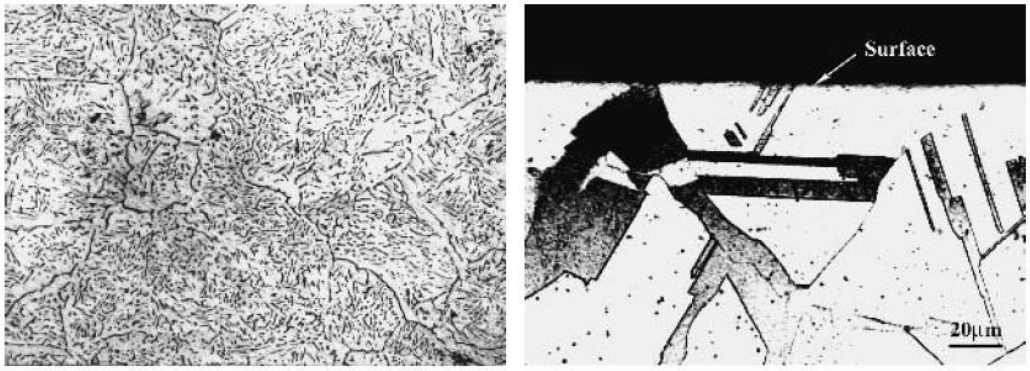


Fig. 1.3 Optical micrographs of the microstructure of ECPed sample and pulsed laser treated sample [44].

It should be noted that the Joule heating rate can be as high as the order of ~10^6 Ks^{-1} and the exposure duration at high temperatures is extremely short (in the order of microseconds) for the treated sample during the application of a ECP [50, 51]. Thus, theoretically the type of phase transformation should be changed from the diffusive transformation to the non-diffusive transformation in metallic materials. Zhang *et al.* proposed that the ECP technique is suitable for studying the heating phase transformation in metallic materials and a commercial Ti-6Al-4V alloy sheet was used for the heating phase transformation by applying an ECP via the capacitor banks discharging to the sample at ambient temperature [51]. It was firstly shown that unusual martensitic transformation from α-Ti to β-Ti induced by the ECP and a large amount of the high-temperature martensitic phase with lamella-shape remained at the ambient temperature as seen in **Fig. 1.4** [51]. The observed martensitic phase transformation was stated as being the results of rapid heat treatment. This result demonstrated new opportunities for studying the heating phase transformation and the high-temperature products.

However, the diffusive phase transformation from α to β phase was found to still occurred in the Cu-Zn alloys during the course of heating by ECP treatment [52]. It should be noted that it is unusual to observe this type of phase transformation under rapid heating conditions, as long-range diffusion is required. They thought that the diffusive transformation is related to a dramatic enhancement of the diffusion coefficient in the Cu-Zn systems induced by the ECP treatment. Many studies of the ECPed Cu-Zn alloys have demonstrated that the high temperature β phase can be retained to the room temperature [52-59]. Wang *et al.* proposed that

the new β phase prefers to be nucleated on the $\{111\}_\alpha$ planes with higher electric conductivity than other crystalline planes during the heating phase transformation process in the Cu-Zn alloys treated by ECP [54-55]. Further studies demonstrated that such a β phase maintains an OR of 44.3° /<114> close to the K-S OR with the parent α phase [57].

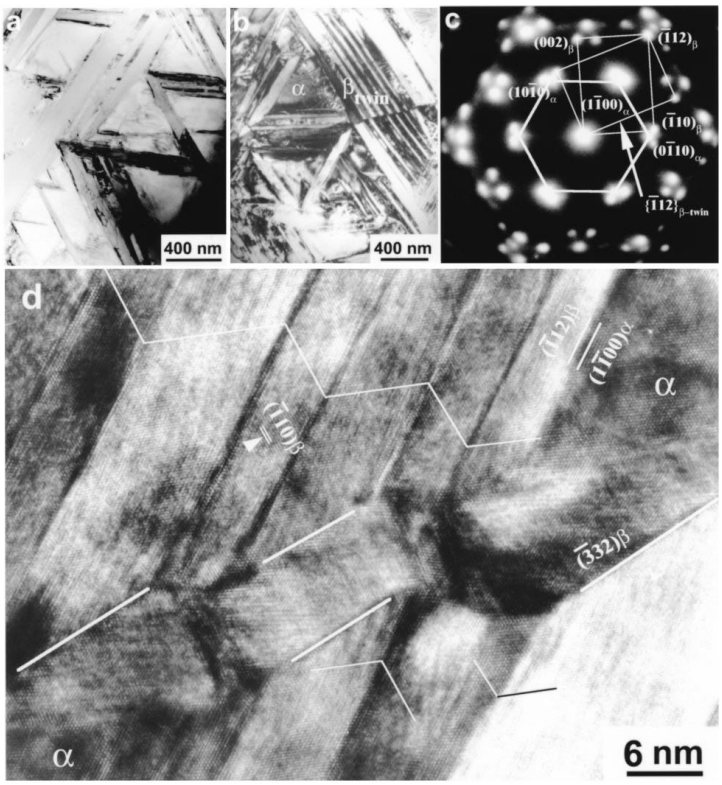


Fig. 1.4 TEM observation of the sample treated by an electric current pulse. Bright-filed images of (a) lamellar features formed in the original grains and (b) edge-on lamellar bands along $[0001]_\alpha$ axis, (c) SAED pattern [51].

ECP treatment has also been applied in combination with other processing methods to achieve various effects [60-63]. Jiang *et al.* studied dynamic ECP-induced phase transformation in magnesium alloys. ECP was applied simultaneously with rolling deformation; a schematic of the apparatus is shown in **Fig. 1.5** [61]. They found that compared with the conventional heat treatment, the ECP treatment accelerated the diffusional phase transformation from β-$Mg_{17}Al_{12}$ to α-Mg in the aged Mg-9Al-1Zn alloy due to the reduction of the nucleation thermodynamic barrier and the enhancement of the atomic diffusion based on the effect of Joule heating and the effect induced by the interaction between electrons and atoms [60, 61]. Zhang *et al.* further studied ECP-induced phase transformations in AZ91 magnesium alloys [63]. For comparison,

static ECP was also conducted [64]. It was found that the ECP was capable of inducing phase transformation with increasing pulse frequency and the static ECPed samples showed a more accelerated phase transformation.

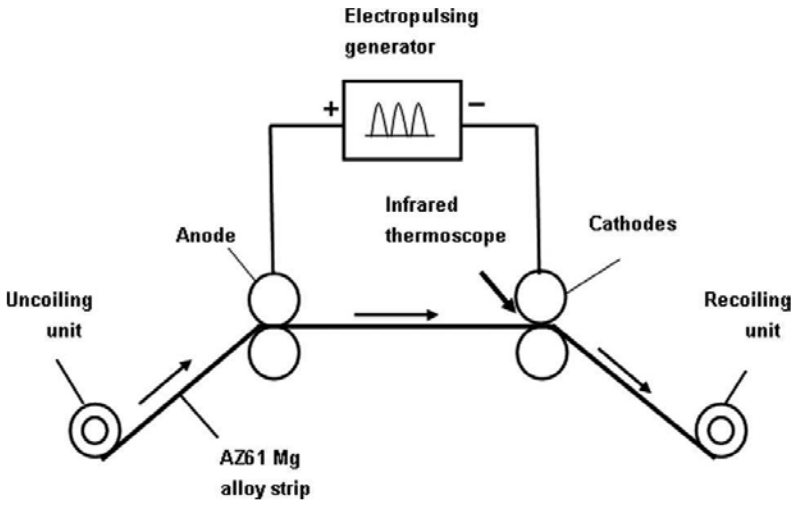


Fig. 1.5 An example schematic of the dynamic ECP process [61].

As summarized above, the ECP treatment as a special treatment method can realize ultra-rapid heating and cooling of a bulk material, allowing the conservation of the high temperature phase to the room temperature and offering possibility for the investigation of phase transformation. However, the microstructural investigations in metals and alloys were only focused on the morphological features and there is little information on the crystallographic characters of the phase transformation in the literature. Therefore, a thorough microstructural study needs conducting for the development of the metallic materials.

1.3 Crystal defect associated solid-state phase transformation

1.3.1 Basic crystal defects of metallic materials

Atom arrangements in real materials do not follow the perfect crystalline patterns in nature. Those irregular atom arrangements always exist as crystal defects in real materials. The presence of crystal defects has a profound impact on the materials mechanical properties, and the control of crystal defects is important in materials processing.

In the crystalline solids, the various defects could be classified as point defects, linear

defects, planer defects and volume defects by their dimensions [65]. For the point defects, it often occurs as vacancy, interstitial, substitutional and interstitial impurity. For the linear defects, they present as dislocations that separates the slipped and unslipped portion of the crystal. In general, two main types of dislocations exist: edge dislocations and screw dislocation. They are characterized by two direction vectors: the dislocation line vector and the Burgers vector. The planer defects are composed of grain boundaries, stacking faults, twin boundaries. The volume defects change the crystal pattern over a finite volume. They include, large voids and inclusions of second-phase particles.

Phase transformations represented by either a pure crystal structure change (displacive) or a crystal structure change accompanied by a chemical composition change (diffusive) from the parent state to the product state happen in many solids when they are subjected to an environmental constraint (thermal, mechanical, magnetic or electric field). In either of the two cases (displacive or diffusive), the structure change is always effect by the above crystal defects. In fact, the crystal defects of the alloys play an important role to ensure phase transformations.

1.3.2 The effect of the defects on the phase transformation

1.3.2.1 Dislocations

Until now, many investigations have been demonstrated that the crystal defects influenced the nucleation of the new phase during phase transformation process in Fe-based alloy [66-70], in Ni-based alloy [71], in Ti-based alloy [72-80], in Cu-based alloy [81] and so on. The dislocation as one of the preferential nucleation sites inside matrix grains has been studied by many authors [82-85]. Studies demonstrated that the existing dislocations in the matrix facilitated or inhibited the nucleation of the new phase during the phase transformation [86, 99]. Moreover, the phase transformations can also induce different types of dislocations formed in the matrix near the new phase [70].

On the dislocations assisted nucleation of a new phase, the early investigations were proposed by Knapp *et al.* [86]. Olson used the basic concepts of classical nucleation theory [68, 69] in the Fe-based alloy. Then Fukuda *et al.* provided a direct microscopic evidence for

nucleation of martensite on dislocations in NiTi [72] and in a Cu-Al-Ni shape memory alloy [81]. Later, it was also found that the interface dislocation type change caused by deformation also makes a favorable contribution to the phase transformation [90]. Furthermore, the phase field approaches [91, 92] and numerical simulations [93-96] were used to analysis the nucleation of martensite on dislocations during phase transformation. Harry and Bacon suggested that screw dislocation cores might assist precipitate transformation into a face-centred-cubic (fcc)-like structure, based on molecular statics simulations (0K) [97]. Osetsky *et al.* showed that precipitate bypass by edge dislocations occurs mainly by cutting through the precipitates by molecular dynamics simulations [98]. They further reported that partial transformation of the larger Cu precipitates into a fcc structure occurs after dislocation detachment. However, the phase transformation mechanism influenced with the dislocations were not discussed in detail.

On the other hand, dislocations also inhibited the growth of q new phase during the phase transformation process. Ibarra *et al.* studied dislocation microstructures after cyclic pseudoelastic compression in Cu–Al–Ni single crystals and identified two dislocation families (A and B) [99]. The type A dislocations represent obstacles to the growth of martensite formed as the result of the interaction of different plates of martensite while the type B results from the plastic deformation of martensite promote the growth of martensite. Then, Lozano-Perez *et al.* performed an *ex-situ* straining experiment on an aged binary Fe–1.3wt%Cu alloy at room-temperature [71]. They directly observed the pinning of dislocations by precipitates though unsuccessful in directly observing the bcc to 9R transformation. The results are in large agreement with the molecular dynamics simulations of the interaction of dislocations with copper precipitates carried out by Bacon *et al.* [87-89].

Furthermore, during the phase transformation process, many dislocations can be formed near the new phase. T. Simon *et al.* observed that elongated dislocation loops from as a result of the martensitic transformation in an *in-situ* TEM cooling/ heating experiment in a NiTi shape memeory alloy [71]. They proposed that the stress field of an approaching martensite needle activated an in-grown dislocation segment and generated characteristic narrow and elongated

dislocation loops. Levitas *et al.* further used the phase field approach to the coupled evolution of martensitic phase transformation and dislocations and reproduced various experimental phenomes, such as dislocations nucleated at the tip of the martensite plate and propagate within the sample [100]. Although, many investigations have been conducted on the dislocation evolution with the formation of the new phase, the corresponding mechanism during the phase transformation process is still unclear.

1.3.2.2 Stacking faults

Until now, many studied have been pointed that stacking faults play an important role during the phase transformation process [101-107], especially on the phase transformation between the fcc structure and the hexagonal structure. Previously, it was proposed that stacking faults in a hexagonal structure could act like embryos for the nucleation of small fcc crystallites governing the phase transformation in cobalt by ball milling [101]. Some others further studied the phase transformation from γ (fcc) to ε (hexagonal) structure and suggested that the ε-phase can be formed by means of stacking faults or be realized by the multiplication of stacking faults through the sweeping of the partial dislocations around a pole dislocation [102，103] or directly by the overlapping of stacking faults [104-106] or via formation and motion of Shockley partial dislocations, which enclosed deformation-type stacking-fault regions [102, 107].Smith's study was the first to evidence that an atomic-scale γ' to ordered hexagonal Co_3 (Cr, Mo, W) phase transformation occurred along stacking faults in Ni-base superalloys by density functional theory (DFT) based *ab inito* calculations using the VASP and high-angle annular dark-field (HAADF)-STEM image simulations [108]. In addition to the stacking faults, incoherent boundary segments can also act as nucleation sites for new phase formation [109, 110].

In addition, the stacking fault energy is one of the most important parameters to determine the occurrence of phase transformation. According to numerous investigations, the probability for the presence of appropriate arrays of partial dislocations is increased, and hence more α'-martensite nucleation sites are available in austenitic steels with lower stacking fault energy, [106, 111-114]. According to a thermodynamic model for the calculation of the stacking fault energy, it was proposed that the tendency for the formation of the ε- martensite and the α'-

martensite increased with decreasing stacking fault energy, which is in good correlation with the modeled stacking fault energy value [115].

1.3.3 The dislocation mechanism on the phase transformation

The above investigations showed that crystal defects (dislocations, stacking faults) of the metallic materials play an important role in the atomic movements to ensure phase transformations. Some authors have clearly demonstrated that a solid-state phase transformation which involves a homogeneous shear must take place by a dislocation mechanism [116-127], as below.

1.3.3.1 Face-center-cubic (fcc) to hexagonal phase transformation

Christian suggested qualitatively that the martensitic transformation from a fcc structure to a close-packed-hexagonal (hcp) structure is the simplest structural change which can be accomplished by the movement of an Shockley partial dislocation on every alternate {111} planes in the $<11\bar{2}>$ direction by a/6 $<11\bar{2}>$ in pure cobalt using an mathematical approach [118]. However, his formation mechanism on the required half dislocations is not regarded as reasonable [119]. Votava further studied the phase transformation of cobalt in experiments and found that the stacking faults are responsible for the cooling phase transformation from the fcc to the hexagonal structure [120]. Then a thermally induced martensitic transformation from the high temperature fcc to the low temperature hexagonal phase was studied in a Co-32% Ni single crystal by transmission electron microscopy (TEM). It was found that the phase transformation took place by consecutive glide of partial dislocations of the same Shockley partial Burgers vector on every other close packed plane [121]. The partials have a Shockley partial Burgers vector ($b = 1/6\ (112)_{fcc} == 1/3\ (1\bar{1}00)_{hcp}$) and in addition they have a small Burgers vector component perpendicular to the glide plane to accommodate for a slight change of the interplanar spacing of the close packed planes [122]. Contrary to this, the reverse transformation from hexagonal to fcc structure in CoNi also studied by the TEM investigation. The results demonstrated the formation of lamellae that were bounded by partials of all three different Shockley partial Burgers vectors [123]. J. Aufrecht *et al.* further observed the Synchro-Shockley dislocation dipoles which were composed of two partial dislocations on two adjacent

planes with different Burgers vectors in the Laves phases $NbCr_2$ and $HfCr_2$ by high-resolution TEM. They proposed that the ordered passage of a series of this type of line defects brings about the phase transformation [124].

Furthermore, various transformation models were proposed that are based on dislocation mechanisms [124-131]. Mahajan S. *et al.* envisaged that the dislocation reaction a/2 $<1\bar{1}0>$ + a/2 $<10\bar{1}>$ → 3* a/6 $<2\bar{1}\bar{1}>$ may govern the nucleation of six-layer hexagonal crystal for the fcc to hexagonal structure transformation [128]. The pole mechanism proposed by Basinski and Christian [129]. Fujita and Ueda visualize that stair - rod cross - slip plays an important role in the formation of hexagonal structure regions [130]. Consider a situation where slip has occurred on the primary slip plane and glide dislocations are dissociated into Shockley partials. If stress on the intersecting glide plane is sufficiently high, Shockley partial may dissociate into a stair-rod and a Shockley partial glide on the intersecting plane. If this process is repeated on parallel planes separated by two layers, a hexagonal structure region could form [130]. The Suzuki mechanism also be proposed to form the hexagonal structure nuclei, that is segregation of solute atoms to stacking faults, on aging the strain hardened materials [131].

Dislocation mechanisms for fcc to hexagonal phase transformation were further studied by DFT [132-135]. Hsiung and Lassila proposed a dislocation dissociation model to account for the stress-induced β to ω transformation: A perfect 1/2 $<111>_\beta$ dislocation on the $\{11\bar{2}\}_\beta$ slip plane dissociates into two 1/12 $<111>_\beta$ partials and one 1/3 $<111>_\beta$ partial on three consecutive $\{11\bar{2}\}_\beta$ planes, whose motions leave behind the ω phase [132, 133]. On the basis of this model, Lai *et al.* proposed that the dissociation and motion of the perfect $<111>_\beta$ dislocations on the $\{11\bar{2}\}_\beta$ slip planes can render the encountered ω phase transforming into the β phase. The passage of these dislocations leaves behind a channel almost completely consisted of β phase in Ti-Nb-based gum metal [134]. Recently, Niu *et al.* proposed that the fcc to hexagonal phase transformation could be achieved by glide of 1/6 $<112>$-type Shockley partial dislocations in the CrCoNi alloy [135]. They showed the energy pathways corresponding to the glide of Shockley partials with the same burgers vector on adjacent {111} planes using the DFT calculations, as shown in **Fig. 1.6**. To compare the energetics of twin formation with those of

the hcp phase transformation, they considered two additional paths once the intrinsic stacking faults (isf) is formed to create an extrinsic stacking faults and a 3-layer twinned region (path 1) and to form 4 layers of the atoms with hexagonal coordination (path 2). For path 3 from an already formed twin boundaries, the formation of the hexagonal phase commences with the motion of a Shockley partial on the plane adjacent to the twin boundary, and can proceed with subsequent partials passing on every other {111} plane. **Fig. 1.6 b** shows the fault energies over 36 configurations with various local chemistry at the fault plane. **Fig. 1.6 c** shows the distribution of energy values for all calculations. It is seen that the hexagonal phase formation from an isf or a twin boundary, lower the energy and requires a lower barrier to overcome compared to the competing process. Their results confirmed that hexagonal phase formation is in fact favored to twin formation in CrCoNi and are consistent with direct HAADF-STEM observations as shown in **Fig. 1.7** [135].

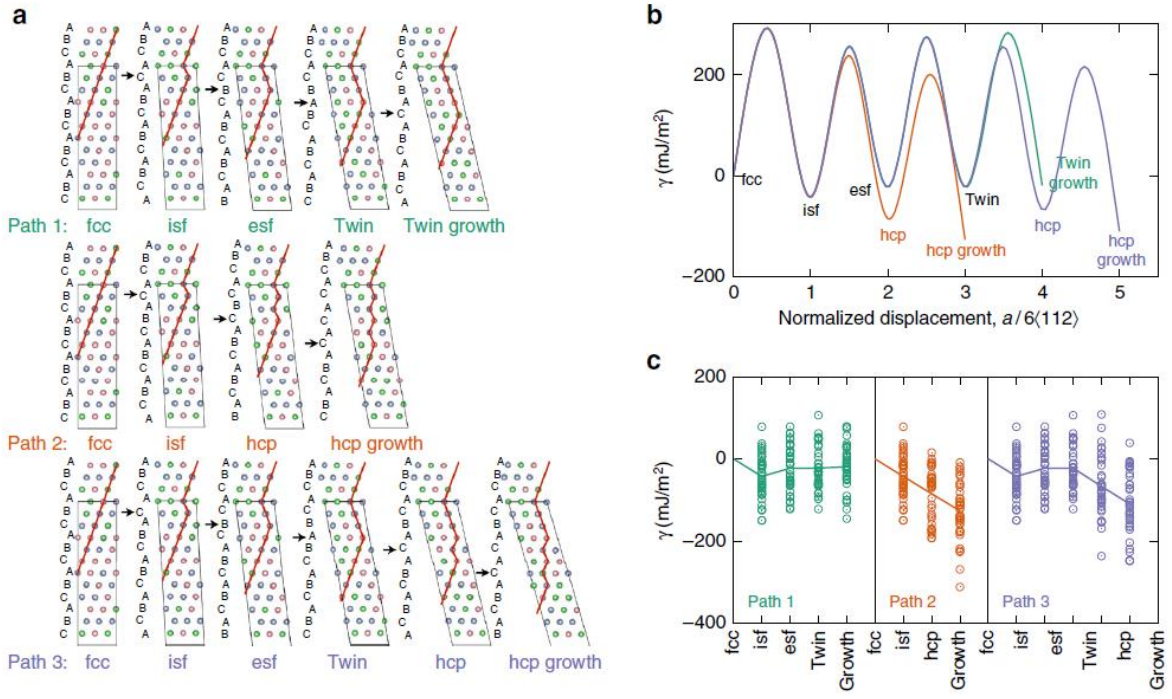


Fig. 1.6 *Ab initio* generalized planar fault energies versus normalized shear displacements on successive {111} planes in CrCoNi. a The supercells used to calculate the energetics of three paths. b The fault energies, averaged over 36 configurations with different local chemistry at the fault plane. c The corresponding energies of all 36 configurations with average values marked by solid lines [135].

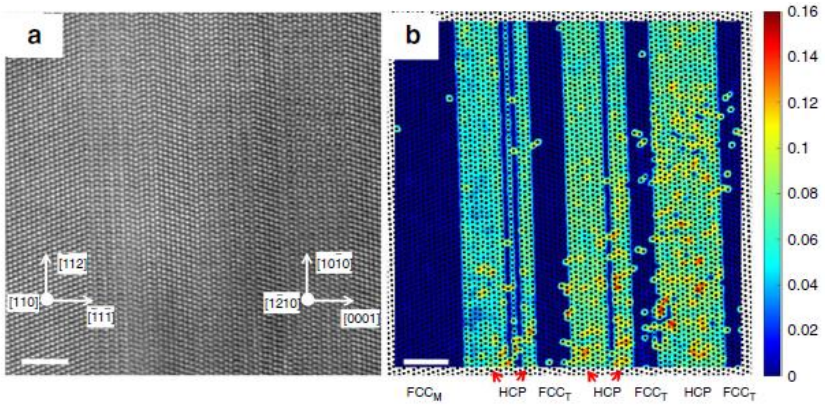


Fig. 1.7 HAADF-STEM images show (a) a well-developed nanotwin-HCP lamellar structure in CrCoNi. The corresponding center of symmetry maps are shown in b [135].

1.3.3.2 Face-center-cubic (fcc) to body-center-cubic (bcc) transformation

For the fcc to bcc phase transformation, Suzuki *et al.* proposed that the motion of perfect dislocations made an effect on the martensitic transformation, especially the interaction between solute atoms and perfect dislocations which seems to results in the different transformation mechanisms [136]. However, Lecroisey *et al.* showed the experimental results on the martensitic transformation (fcc γ to bcc α') in steels that the α' martensite laths are frequently located at the intersection of 2 deformation bands on the $\{111\}_\gamma$ plane in austenite [137]. They thought that the fcc to bcc phase transformation is initiated by the moving of the $\{111\}_\gamma$ $<211>_\gamma$ transformation dislocation and then completed by a second shear and by the accommodations necessary. The possible role of such transformation dislocations has been evidenced by many authors [138-142].

1.3.3.3 Bcc to hexagonal structure transition

In addition, the bcc to two kinds of hexagonal structure transition mechanism have been widely and deeply studied on many alloys systems, such as Ti-based alloys [143-162], Zr-based alloys [163, 164] and Cu-based alloys [166-172]. Of the two hexagonal structures, the one possesses a crystal structure resembling that of the equilibrium α phase with the Burges orientation relation (BOR) with the β matrix [163], and the other have a crystal structure resembling that of the metastable ω phase with the Blackburn OR with the β matrix [159]. Due to the two kinds of structure distortions in the β matrix, additional weak reflections are produced

at the approximate 1/2 β reflection positions in the TEM Selected Area Electron Diffraction (SAED) patterns for the former and at the approximate 1/3 and 2/3 β reflection positions for the latter [145-148]. Furthermore, it is reported that characteristic atomic shuffles or displacements on certain shear systems of the bcc phase commonly result in the formation of hexagonal structures in a form of nano-sized atomic clusters. Many experimental investigations have shown that the atomic shuffles or displacements are associated with the $\{110\}<\bar{1}10>$ and $\{\bar{1}12\}<\bar{1}1\bar{1}>$ shear systems [147, 165]. Further studies revealed that the softening of the two shear systems corresponds to the lower energy or soft phonon modes of the β phase [165]. It should be noted that the $\{110\}<\bar{1}10>$ and $\{\bar{1}12\}<\bar{1}1\bar{1}>$ shear systems are coincidence with the typical dislocations of the bcc structure.

To summarized above, the dislocations of the parent phase played an important role to ensure the typical phase transformation. However, the impact of the dislocations on the phase transformation from fcc to bcc and the cooresponding mechanism on the dislocation evolution with the new phase are still not clear. So, it needs further studying.

1.3.4 Crystal defect type associated transformation OR selection

As we known, to ensure that the structure change is energetically economical, a specific orientation relationship (OR) is respected by the two end phases to minimize the lattice distortion energy. Depending on the crystal system of the two end phases, different ORs are present, such as the Kurdjumov-Sachs OR (K-S), i.e., $\{111\}_\alpha$ //$\{110\}_\beta$, $<\bar{1}10>_\alpha$ //$<\bar{1}11>_\beta$, observed in steels [173-176], Fe–based alloys [177-179] and Cu-Zn alloys [180]; the Nishiyama-Wasserman OR (N-W), i.e., $\{111\}_\alpha$//$\{110\}_\beta$, $<11\bar{2}>_\alpha$//$<\bar{1}10>_\beta$ in steels [173, 175, 176], Fe-Ni-Co-Ti shape memory alloy [181] and in Gibeon meteorites [182], the Burgers OR (BOR), i.e., $\{110\}_\beta$//$\{0001\}_\alpha$, $<\bar{1}1\bar{1}>_\beta$//$<11\bar{2}0>_\alpha$, in Ti based alloys [183-186], the Pitsch OR, i.e., $\{101\}_\alpha$//$\{1\bar{2}\bar{1}\}_\beta$, $<10\bar{1}>_\alpha$//$<\bar{1}\bar{1}1>_\beta$, in Ni–Mn based intermetallic compounds [187] and other special OR, i.e., $\{001\}_{7M}$//$\{112\}_{NM}$, $<100>_{7M}$//$<11\bar{1}>_{NM}$, in Ni–Mn–Ga alloys [188]. According to the above results, the structure change is always realized by the existing dislocations of the parent crystal structure. Moreover, the nucleation of a new phase occurs heterogeneously at some preferential nucleation sites in the parent phase such as grain

boundaries, dislocations and second phase during most phase transformation processes. Thus, the phase transformation OR should be related to the different type defects. The relation between the observed transformation ORs and the possible perfect or partial dislocations to facilitate certain OR variants produced by phase transformation in some materials have been an interest of study since last century and continues to attract attention [182, 189-195] to date.

Bogers *et al.* observed different orientation relationships regarding to the transition of austenite into martensite and suggested that a certain orientation relation be realized depending on the action of the dislocations present or created by external stress [116]. Later, Luo and Weatherly further studied the crystallography of bcc precipitates nucleated on various kinds of defects in the fcc matrix of a Ni–Cr alloy [193]. They found that the bcc precipitates nucleated on dislocation hold the variant of the K–S relationship, for which the maximum misfit direction calculated by the surface dislocation theory [194] is nearly parallel to the Burgers vector of the dislocation. Ameyama and Maki further found that a fcc γ precipitate holds the K–S relationship with respect to both the bcc α matrix and the twin at the {112}<111> deformation twin boundary in a duplex stainless steel [195].

Furthermore, the correspondence relations between the OR plane and the glide plane and between the OR direction and the Burgers vectors of the dislocations (perfect or partial) have been phenomenologically studied for the K-S and N-W relations [190, 191]. With such an approach of correspondence relations, the association of each plane/ burgers vector combination with a particular variant is established and the presence of both “positive slip” and “negative slip” variants within individual grains, a puzzling phenomenon, have been successfully interpreted [190]. The approach explains well the differences in the proportions of the K-S and the N-W variants observed experimentally in relation with the stacking fault energy of the parent phase [190, 192].

However, the experimental investigation on the evidences of the corresponding perfect and partial dislocations is further needed, as stated by the authors of [190]. Moreover, the correlation between the strains of the perfect or the partial dislocations and the lattice deformation of the phase transformation to realize the crystal structure change from the parent

phase to the product phase needs to be studied to reveal the underlying physical mechanisms of the influence of different types of dislocations on the transformation strain path of different OR variants.

1.4 Phase transformations in Cu-Zn alloys

The Cu-Zn alloys are widely used in many applications such as lead frames, connectors, pipes, valves, and in fittings in potable water systems due to their superior electrical and thermal conductivities, excellent corrosion resistance, ease of fabrication, and good strength and fatigue resistance [196]. The development of high-performance brasses is necessary to satisfy new demands posed by the electronics industry, automotive, and aerospace applications and household appliance development. It is well known that their mechanical properties are strongly dependent on the microstructural characteristics, especially the size, the volume fraction, the morphology and distribution of the precipitates [197-200], therefore the phase transformation process has been extensively studied to obtain an appropriate microstructure.

From the last century on, many studies have focused on the phase transformation during cooling course in the Cu-Zn alloys. It was reported that the phase transformation usually follows specific orientation relationships [201-209], such as the K-S OR, i.e., $\{111\}_{\alpha}//\{110\}_{\beta}$, $<\bar{1}10>_{\alpha}//<\bar{1}11>_{\beta}$ [203-208] or N-W OR, i.e., $\{111\}_{\alpha}//\{110\}_{\beta}$, $<11\bar{2}>_{\alpha}//<\bar{1}10>_{\beta}$ [209] and displays different occurrences of the variant following the different ORs under different treatments [202-205]. At the same time, the precipitates also show different morphology such as the widmanstatten typed under heat treatment [206], the needle shape under dezincification [207, 210], the fine globular shape under extrusion [209] and the plate shape [211, 212] and so on.

In the recent years, the heating phase transformation from the fcc structure to the bcc structure was realized by the ECP treatment [52, 54-57, 213]. It is evidenced that the high temperature β phase could be retained to the ambient temperature and the ECP could enhance the nucleation resulting from the electric current itself. It is worth noting that, by the ECP treatments, the high temperature β phase nucleated from the α phase obeyed the orientation relation of 44.3°/<114> [56], which is close to the K-S relationship, during the heating phase transformation in the Cu-Zn alloys.

Furthermore, it has been reported earlier that two kinds hexagonal structure had been observed in the Cu-Zn alloys under heat treatment [166-168] and the dezincification treatment [169-172]. They also proposed that the β phase transforms to the hexagonal structure by a simple shuffle mechanism on the $(011)_\beta$ planes in the $\pm[01\bar{1}]_\beta$ directions or the atomic displacements on the $\{110\}<1\bar{1}0>$ system [168, 170-172]. The lattice instability resulting from the soft phonon modes of the B_2 β or β' phase is also the inherent features of the β or β' phase (having an ordered BCC structure) in the Cu-Zn alloys [166]. However, on the formation mechanism of the hexagonal structures in the Cu-Zn alloys, it remains not detailed.

1.5 Content of the present work

In the past, the effect of the crystal defects (dislocations and stacking faults) on phase transformation of metallic materials have been studied, including the dislocations (perfect and partial) assisted structure transition and the formation of the dislocations caused by phase transformation. However, in some aspects on the transformation mechanism induced by crystal defects, it still need profound understanding, such as the dislocation mechanism on phase transformation OR study and the interaction between the defects and new phase during the phase transformation process. Furthermore, numerous studies on the effect of the partial dislocations of the fcc to hexagonal structure have been conducted by experiments and simulations. Compared to this, the effect of the crystal defects on the structure transitions from the fcc structure to bcc structure and from the bcc structure to the hexagonal structure need further studied.

Cu-Zn alloys as traditional metallic materials are widely studied and used in many applications due to the outstanding performances. In the recent years, the heating phase transformation from the fcc structure to the bcc structure in the Cu-Zn alloys were realized by ECP treatments at room temperature. However, few researchers studied the effect of the crystal defects on heating phase transformation of the Cu-Zn alloys and the product phase with bcc structure.

On the basis of such a background, the Cu-40%Zn alloy was used to study the effect of the crystal defects on the solid phase transformation in the present work. A thorough

investigation on microstructural and crystallographic features of the parent and product phases, the crystal defect evolution of the parent phase and the structure transition mechanism in Cu-40%Zn alloys were conducted in the present PhD work. The main contents of this work can be outlined as below:

(1) Phase constituents and crystallographic feature characterization of Cu-40%Zn alloys by means of XRD diffraction and SEM EBSD techniques. Study of heating phase transformation (fcc to bcc) mechanism by characterizing the changes on the defects of the parent phase and the orientation relationship during the heating phase transformation. (Chapter 3)

(2) Study of the formation of dislocations induced by the product phase during the heating phase transformation process by TEM. (Chapter 4)

(3) Investigation on structure transition mechanism from bcc to hexagonal structures analyzed by TEM and high-resolution STEM. (Chapter 5)

This work aims at further studying the effect of the crystal defects on the structure transitions from the fcc structure to the bcc structure and from the bcc structure to the hexagonal structures, and the interaction between the crystal defects and product phase to provide new information on heating phase transformation in the Cu-Zn alloys.

Chapter 2 Experimental and calculation methods

2.1 Experimental details

2.1.1 Alloy preparation and heat treatment

The material used in the present work is the hot-rolled Cu-40%Zn alloy sheet (300×150×1.5mm). The composition analyzed by the X Ray Fluorescence is given in **Table 2.1** and is very close to the nominal one.

Table. 2.1 Chemical composition (in wt. / %) of the hot-rolled Cu-Zn alloy.

Cu%	Zn%	Si%
60.86	39.06	<0.01

Dog-bone-shaped samples with gauge dimensions of 10 mm in length, 2 mm in width, and 1.5 mm in thickness, as shown in **Fig. 2.1**, were cut out of the center part of the hot-rolled Cu-40%Zn sheet by the electro-spark discharge technique. Then, these samples were heat treated at 500°C in the α+β phase region for 30 min and cooled in air to increase the crystal perfection and homogenize the microstructure. Such samples are named annealed samples and the treated state was used as the initial state for the subsequent treatments.

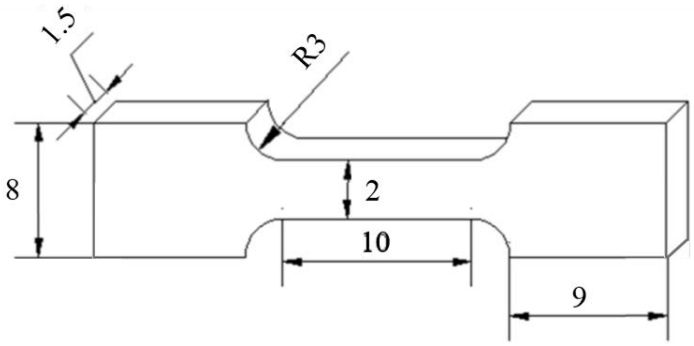


Fig. 2.1 A schematic illustration of the sample shape.

2.1.2 ECP treatments

The heat treated (annealed) samples were further treated under electric current pulse (ECP) treatments. A schematic illustration of the ECP treatment arrangement is given in **Fig. 2.2 (a)**. A single electric current pulse was produced by a discharge of the capacitor banks and goes through the annealed samples at room temperature. The two ends of each sample were put into the copper electrodes under atmospheric condition during the ECP treatment. Since the sizes of the two ends were much wider than the gauge part, the current flux in the gauge part is much higher than that in the two ends during the ECP process. Thus, the temperature rise of the two ends is very small and can be neglected. **Fig. 2.2 (b)** displays a typical wave profile of a measured electric current pulse. The pulse takes a form of a damped oscillation wave. During the treatment, the current density and the pulse duration were instantaneously recorded using a Rogowski coil and a TDS3012 digital storage oscilloscope (Tektronix, Beaverton, Oregon).

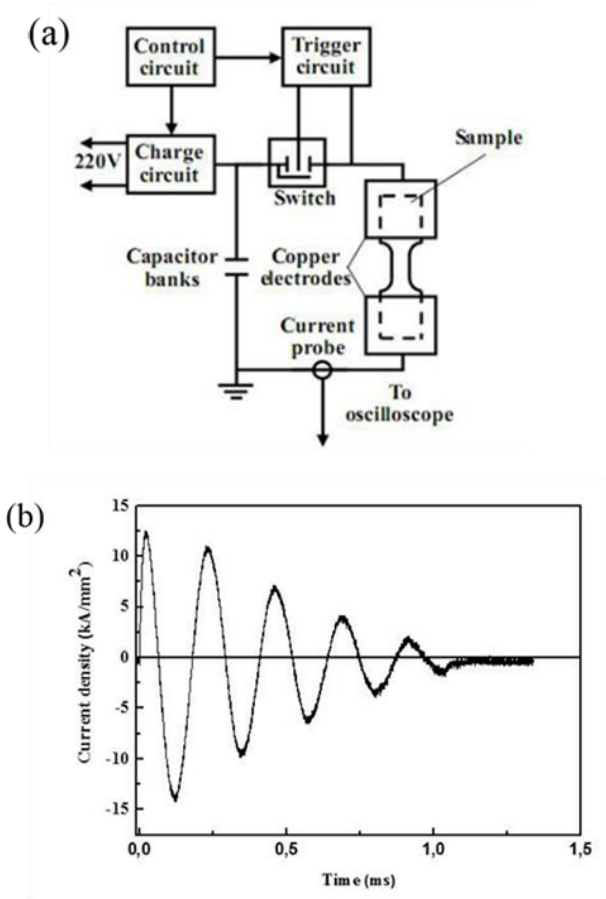


Fig. 2.2 (a) Illustration of ECP experimental arrangement; (b) The typical waveform of an ECP.

In this work, the ECP treatment was performed at various instant voltages that correspond to the current densities of about 15.12 kA/ mm^2, 15.66 kA/ mm^2, 15.93 kA/ mm^2, 17.01 kA/ mm^2 and 17.28 kA/ mm^2, respectively, with the pulse duration of 117 μs, 118 μs, 118 μs, 125 μs and 150 μs.

During the ECP treatment, the electric heating of the samples can be regarded as an adiabatic course due to the very short treatment time, and the temperature rise can be evaluated using the waveforms of the electric current pulse according to the following Equation (2-1):

$$\Delta T = \frac{\int_0^{t_d} j^2(t)\rho dt}{C_\rho d} \tag{2-1}$$

where *j(t)* is the electric current density at time *t*, ρ is the resistivity (0.062×10^{-6} Ω·m), t_d is the pulse duration (117 μs), C_p is the specific heat (378J/ kg/ K), and d is the volumetric mass density (8.40×10^3 kg/ m^3) of the specimen. Here, the electric current density is the peak value of an instantaneous current intensity in the pulse duration. According to the waveform (in **Fig. 2.2 (b)**) under different current density, the correspond temperature were calculated and shown in **Table 2.2**. It should be noted that the temperature value is derived on the basis of the electrical resistivity (ρ) and the current density (j) of the sample at equilibrium state. So the absolute value of the calculated temperature is indicative but the relative value between different current densities is accurate. As shown in **Table 2.2**, it is clear that the temperature of the samples rises with the increase of the electric current density.

Table. 2.2 Calculated temperature of the Cu-40%Zn alloy during the ECP treatment.

Electric Current Density (kA/mm^2)	Duration (μs)	T (°C)
0	0	25
15.12	117	550
15.66	118	588
15.93	118	642
17.01	125	876
17.28	150	899

2.1.3 X-ray diffraction measurement

The phase constituents and their lattice constants of the samples before and after the ECP treatment were analyzed by X-ray diffraction (XRD, Rigaku, Smartlab), using a Cu-Kα radiation at room temperature. The diffraction patterns were measured at a 2θ range from 40° to 90°. The "step" mode was used with a scanning step of 0.01° (2θ) and a duration of 4 seconds. The software *Jana 2006* was used to fit the lattice constants.

2.1.4 Microstructural characterization

The microstructural examinations and crystallographic orientation investigations were performed in a field emission gun scanning electron microscope (SEM, Jeol JSM 6500 F) with an EBSD acquisition camera and the Aztec online acquisition software package (Oxford Instruments). During the EBSD measurements, the "beam-control" mode was applied with a step size of 0.15 μm under an accelerating voltage of 15 kV. The EBSD data were analyzed with the Oxford Channel 5 software and the Atex software [221]. The EBSD samples were first mechanically ground using the emery/ SiC grinding paper up to 4000 # and then polished using diamond paste (1 μm), and then electrolytically polished with a solution of 20 % (volume fraction) nitride acid in methanol at 18 V for 3 seconds at room temperature.

The nano scaled microstructural and crystallographic features of the constituent phases were analyzed using a Philips CM 200 transmission electron microscope (TEM) operated at 200 kV. The TEM is equipped with a LaB6 cathode, a Gatan Orius 833 CCD camera, and homemade automatic orientation analysis software – Euclid's Phantasies (EP) [214, 215]. The atomic scaled microstructures were analyzed by high-resolution scanning transmission electron microscopy (STEM), using a JEOL JEM-ARM200F TEM operated at 200 kV. High-angular dark-field (HAADF) images were acquired with an inner and outer collecting angle of 68 and 280 mrad, respectively. TEM thin films were prepared first by mechanical thinning to 80 μm and then by electrolytic polishing to perforation at -30°C in a solution of 20 % (in volume) nitride acid in methanol at 20 V, using a Struers Tenupol-5 twin-jet electropolisher.

During the TEM examination, the crystallographic orientation of the microstructural

constituents was determined by indexing the TEM Kikuchi line patterns using the software EP and expressed in a triplet of Euler angles in Bunge's notation [216, 217]. Orientation relationships (OR) between the microstructural constituents were analyzed by misorientation calculation. The dislocation types and the dislocation Burgers vectors were analyzed using invisibility criterion and by matching the observed dislocation line orientation with the theoretical ones as described in [218]. The atomic correspondences and the electron diffraction patterns for the structure transformation from the parent phase to the product phase were analyzed using the Crystal Maker® [219] software.

2.1.5 Chemical composition analysis

The chemical composition distribution characteristics were examined by the electron probe microanalysis (EPMA). X-ray line profiles and energy scans were obtained using an FEG-EPMA instrument (JEOL JXA-8530 F). In each measurement, the working distance was approximately 11 mm, the take-off angle was 40° and the In-Lα X-rays (critical excitation voltage: 3.73 keV) were employed. The radius of the Rowland circle was 100 mm (an H-type spectrometer with a JEOL microprobe) and the analyzing crystal was made of pentaerythritol (PETH). The probe current (Iprob) was in the range of 10^{-12} – 5 * 10^{-7} A and the sampling time was 1 second per point. The electron beam was focused.

2.2 Basic crystallographic calculations

2.2.1 Coordinate system

During the crystallographic calculation processes, two kinds of coordinate systems were used in the present work. The one is the orthonormal coordinate system '*x- y- z*' or '*i-j-k*' which is either set to the sample frame or to the crystal bases as shown in **Fig. 2.3**. The other is the Bravais lattice basis of the cubic crystal (α and β structure) and the hexagonal crystals (ε and ω structure), *i.e.* '*a- b- c*' of the cubic crystal structure in **Fig. 2.3 (b)** and the hexagonal structure in **Fig. 2.3 (c)**. When the orthonormal coordinate system is set to the Bravais lattice basis, the geometrical relation between the orthonormal coordinate system and the Bravais lattice basis conforms to the convention defined by the *Channel 5* software package. All coordinate systems

are of right-handedness.

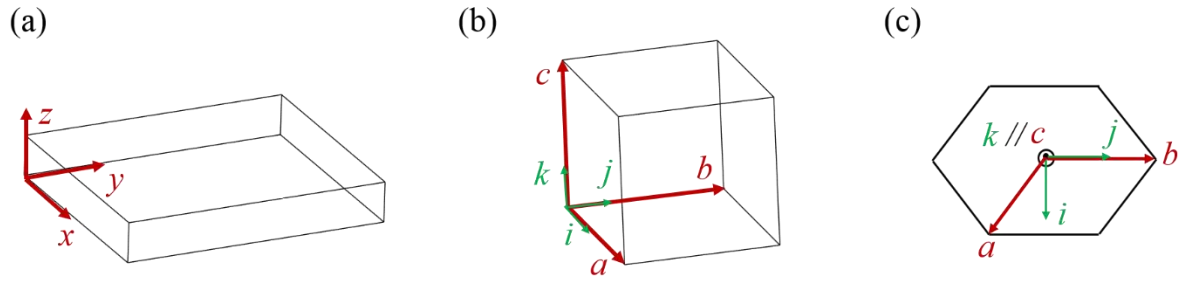


Fig. 2.3 Two kinds of coordinate systems used in the present work. Orthonormal coordinate system is set to the sample frame '*x*- *y*- *z*' (a) or to the crystal basis '*i*- *j*- *k*' (b) and (c); Bravais lattice basis '*a*- *b*- *c*' of the cubic structure in (b) and hexagonal structure in (c); the relationship between the orthonormal coordinate system and the corresponding Bravais lattice basis are demonstrated in (b) and (c). All coordinate systems are of right-handedness.

2.2.2 Coordinate transformation and orientation relation

2.2.2.1 Coordinate transformation matrix

The relative orientation between two coordinate systems, for example the sample coordinate system '*x*- *y*- *z*' and the crystal coordinate system '*i*- *j*- *k*' can be described with the coordinate transformation matrix. The relation between the two coordinate systems '*x*- *y*- *z*' and '*i*- *j*- *k*' are given in Equation (2-2).

$$\begin{aligned} i &= a_{11}x + a_{21}y + a_{31}z \\ j &= a_{12}x + a_{22}y + a_{32}z \\ k &= a_{13}x + a_{23}y + a_{33}z \end{aligned} \tag{2-2}$$

So, the coordinate transformation matrix M from the sample coordinate system to the crystal coordinate system can be written as:

$$\mathrm{M} = \begin{pmatrix} a_{11} & a_{12} & a_{13} \\ a_{21} & a_{22} & a_{23} \\ a_{31} & a_{32} & a_{33} \end{pmatrix} \tag{2-3}$$

2.2.2.2 Euler angles

In general, the Euler angles (φ_1, Φ, φ_2) are conveniently used to describe the relative relationship between two orthonormal coordinate systems, for example the crystal coordinate

system with respect to the sample coordinate system. The Euler angles (if in Bunge notation) involve three consecutive rotations φ_1, Φ and φ_2, as demonstrated in **Fig. 2.4**, where the '*x*- *y*- *z*' represents the sample coordinate system S and the '*i*- *j*- *k*' is set to the Cartesian crystal coordinate system C.

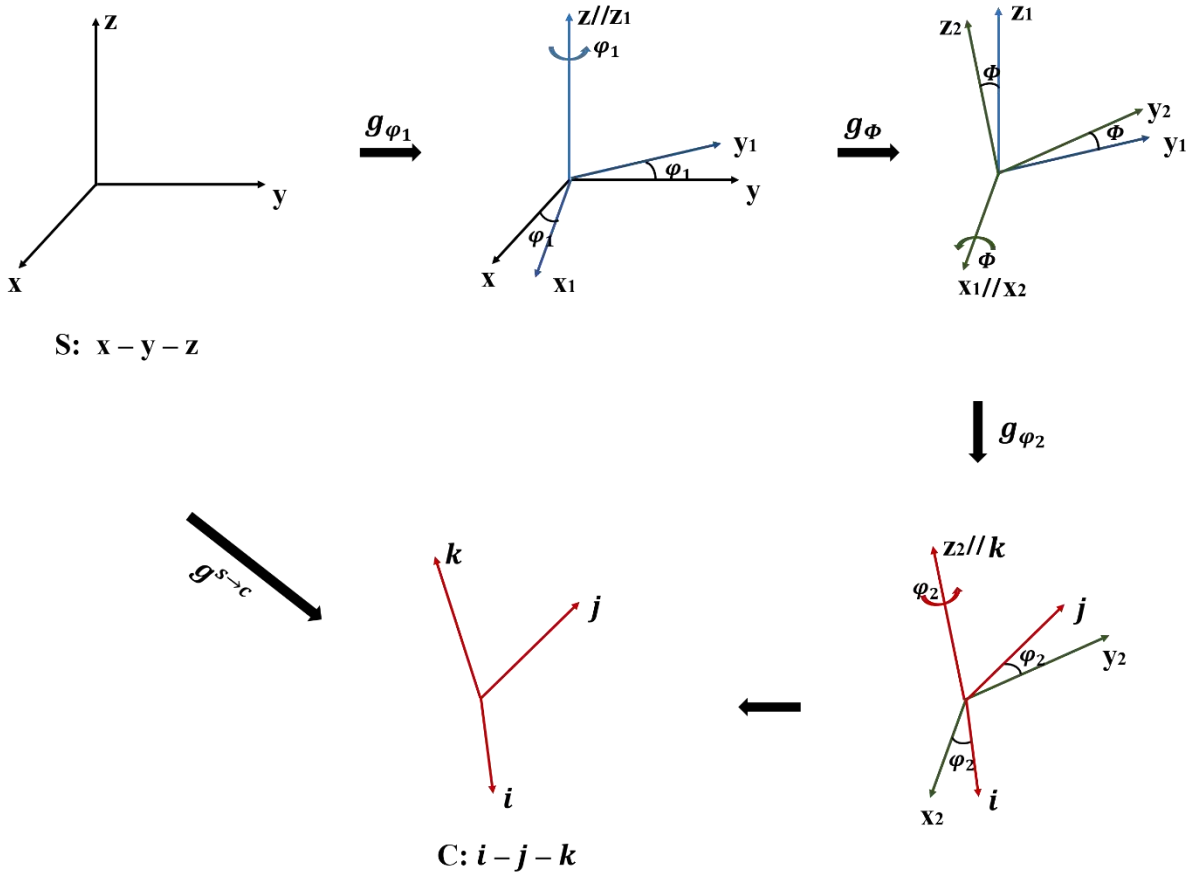


Fig. 2.4 Illustration of the three rotations in Bunge notation. The sample coordination system S: '*x*-*y*-*z*'; the Cartesian crystal coordinate system C: '*i*-*j*-*k*'.

The rotation matrix $g^{s\to c}$ from the sample coordinate system S to the Cartesian crystal coordinate system C can be described as:

$$g^{s\to c} = g_{\varphi_1} * g_{\phi} * g_{\varphi_2}$$

$$= \begin{pmatrix} \cos\varphi_1 \cos\varphi_2 - \sin\varphi_1 \sin\varphi_2 \cos\Phi & -\cos\varphi_1 \sin\varphi_2 - \sin\varphi_1 \cos\varphi_2 \cos\Phi & \sin\varphi_1 \sin\Phi \\ \sin\varphi_1 \cos\varphi_2 + \cos\varphi_1 \sin\varphi_2 \cos\Phi & -\sin\varphi_1 \sin\varphi_2 + \cos\varphi_1 \cos\varphi_2 \cos\Phi & -\cos\varphi_1 \sin\Phi \\ \sin\varphi_2 \sin\Phi & \cos\varphi_2 \sin\Phi & -\cos\Phi \end{pmatrix} \quad (2\text{-}4)$$

where

$$g_{\varphi_1} = \begin{bmatrix} \cos\varphi_1 & \sin\varphi_1 & 0 \\ -\sin\varphi_1 & \cos\varphi_1 & 0 \\ 0 & 0 & 1 \end{bmatrix}$$

$$g_{\phi} = \begin{bmatrix} 1 & 0 & 0 \\ 0 & \cos\phi & \sin\phi \\ 0 & -\sin\phi & \cos\phi \end{bmatrix}$$

$$g_{\varphi_2} = \begin{bmatrix} \cos\varphi_2 & \sin\varphi_2 & 0 \\ -\sin\varphi_2 & \cos\varphi_2 & 0 \\ 0 & 0 & 1 \end{bmatrix}$$

2.2.2.3 Coordinate transformation

The coordinate transformation is used to express the same vector or plane in different coordinate systems in the crystallographic calculation. As displayed in **Fig. 2.5**, two arbitrary coordinate systems S_1 and S_2 are defined with basis vectors '*x*, *y*, *z*' and '*i, j, k*' respectively, and a vector $\vec{V}$ is expressed as [*x, y, z*] and [*i, j, k*] in the two references S_1 and S_2, respectively. The relationship between the two sets of coordinates can be linked with the coordinate transformation matrix M which is described in detail in § 2.2.2 (p26) and can be expressed in Equation (2-5):

$$\begin{bmatrix} x \\ y \\ z \end{bmatrix}^{S_1} = M * \begin{bmatrix} i \\ j \\ k \end{bmatrix}^{S_2} \tag{2-5}$$

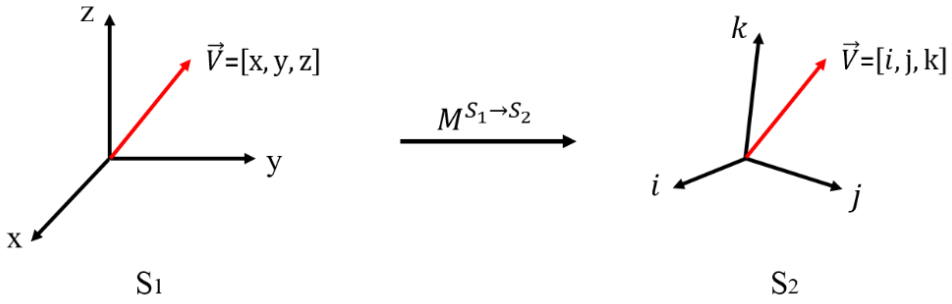


Fig. 2.5 Illustration of coordinate transformation of a vector between two coordinate systems S_1 ('*x- y- z*') and S_2 ('*i- j- k*').

2.2.2.4 Misorientation

The angle/ axis pair - (ω, d) is usually used to describe the relative relationship between two crystal coordinate systems C_1 and C_2. That is the misorientation expressed with a rotation ω from one symmetrically equivalent Cartesian crystal coordinate system of crystal C_1 along the axis d to another symmetrically equivalent Cartesian crystal coordinate system of crystal C_2. In order to determine the angle/ axis pair - (ω, d), the misorientation matrix $\Delta g^{C_1 \to C_2}$ between these two crystals C_1 and C_2 is required to be calculated, as demonstrated in **Fig. 2.6**.

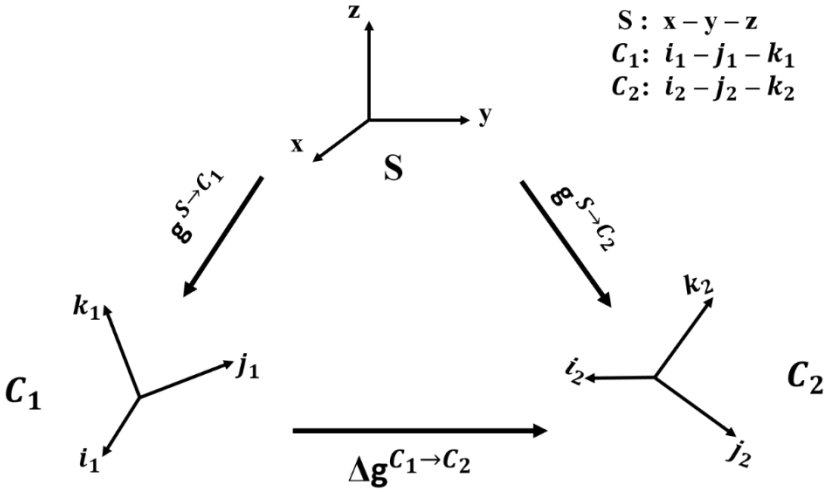


Fig. 2.6 Schematic of misorientation between two crystal coordinate systems C_1 and C_2. '*x- y- z*' is the sample coordinate system *S*. 'i_1- j_1- k_1' and 'i_2- j_2- k_2' are the Cartesian crystal coordinate systems C_1 and C_2, respectivily. $g^{S \to C_1}$ and $g^{S \to C_2}$ are rotation matrices from the sample coordinate system *S* to the Cartesian coordinate systems of the two crystals C_1 and C_2. $\Delta g^{C_1 \to C_2}$ is the misorientation matrix between the two crystals C_1 and C_2.

It should be noted that all the coordinate systems (S, C_1 and C_2) are orthonormal. The misorientation matrices $\Delta g^{C_1 \to C_2}$ can be expressed with Equation (2-6).

$$\Delta g^{C_1 \to C_2} = (S_i)^{-1} \times (g^{S \to C_1})^{-1} \times g^{S \to C_2} \times S_j \tag{2-6}$$

where S_i and S_j are the rotational symmetric matrices of crystal C_1 and C_2, respectively, $g^{S \to C_1}$ and $g^{S \to C_2}$ represent the rotation matrices from the sample coordinate system *S* to the corresponding Cartesian crystal coordinate systems of crystal C_1 and C_2 that are obtained by the corresponding experiment data. Denote the misorientation matrix $\Delta g^{C_1 \to C_2}$ as below:

$$\Delta g^{C_1 \to C_2} = \begin{pmatrix} g_{11} & g_{12} & g_{13} \\ g_{21} & g_{22} & g_{23} \\ g_{31} & g_{32} & g_{33} \end{pmatrix} \tag{2-7}$$

The misorientation expressed with the rotation angle ω and the rotation axis d [d_1 d_2 d_3] in the Cartesian crystal coordinate system can be further calculated using the following Equations:

$$\omega = \arccos\left(\frac{g_{11}+g_{22}+g_{33}-1}{2}\right) \tag{2-8}$$

(1) $\omega = 0°$

$$d = [1 \quad 0 \quad 0] \tag{2-9}$$

(2) $0° < \omega < 180°$

$$d = \left[\frac{g_{23}-g_{32}}{2\sin\omega} \quad \frac{g_{31}-g_{13}}{2\sin\omega} \quad \frac{g_{12}-g_{21}}{2\sin\omega}\right] \tag{2-10}$$

(3) $\omega = 180°$

$$d = \left[\pm\sqrt{\frac{g_{11}+1}{2}} \quad \pm\sqrt{\frac{g_{22}+1}{2}} \quad \pm\sqrt{\frac{g_{33}+1}{2}}\right]$$

$$\text{with} \begin{pmatrix} |d_m| = \max(|d_i|, i=1, 2, 3) \\ d_m > 0 \\ \forall\, i \neq m,\ d_i = \text{sign}(g_{im}) \cdot |d_i| \end{pmatrix} \tag{2-11}$$

Due to the crystallographic rotational symmetry of the crystals, more than one crystallographically equivalent rotation axis/ angle pairs can be figured in the calculation, but all the calculated (ω, d) are crystallographically equivalent.

2.2.2.5 Phase transformation orientation relationship

In general, the crystallographic transformation orientation relationship (OR) between the parent crystal (P) and the product crystal (D) could be defined by a pair of parallel crystalline planes and a pair of in-plane parallel directions, as described in Equation (2-12):

$$(hkl)_P // (hkl)_D \qquad [uvw]_P // [uvw]_D \tag{2-12}$$

During the crystallographic calculations, the coordinate transformation matrix is often used to describe the orientation relation between the two crystal systems (parent and product

phases). The geometrical relation between the two crystal systems (a_P-b_P-c_P and a_D-b_D-c_D) under the OR is illustrated in **Fig. 2.7**. The orthonormal or Cartesian coordinate system '*i*- *j*- *k*' is set on the OR system of the two phases. *k* is parallel to the normal of the OR plane, *j* is parallel to the OR direction and *i* is parallel to the vector cross product of the OR direction and the OR plane normal direction. M_P and M_D are the coordinate transformation matrix from the Bravais lattice basis '*a*-*b*-*c*' of the parent crystal or the product crystal to the Cartesian coordinate system '*i*-*j*-*k*'. Thus the coordinate transformation matrix between the two Bravais lattice bases of the two phase M^{OR} can be deduced as follows.

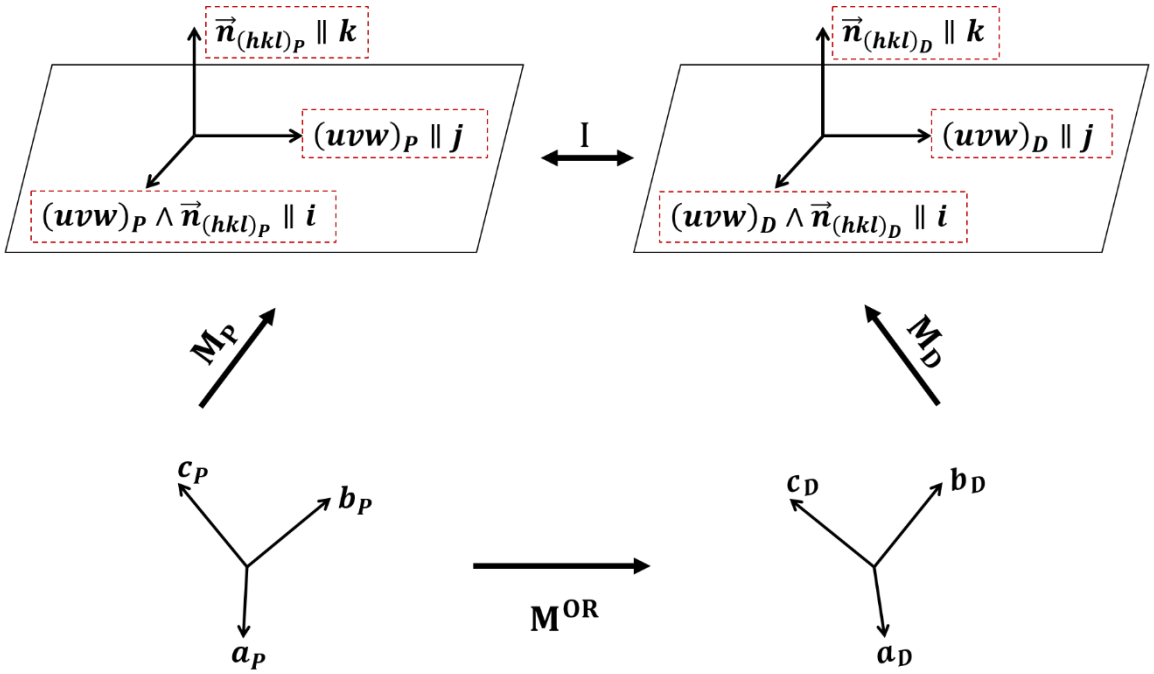


Fig. 2.7 Schematic of coordinate transformation between the parent and the product crystals under a given orientation relationship. All coordinate systems are of right-handedness.

First, the three basis vectors '*i, j, k*' of the corresponding Cartesian coordinate system can be expressed in the corresponding Bravais bases of the parent and the product crystals:

$$\vec{k}_i = \vec{n}_{(hkl)i} = \mathrm{g}_\mathrm{i}^* \times \begin{pmatrix} h \\ k \\ l \end{pmatrix}_i \tag{2-13}$$

$$\vec{j}_i = \begin{pmatrix} u \\ v \\ w \end{pmatrix}_i \tag{2-14}$$

$$\vec{\imath}_i = \mathrm{g}_\mathrm{i}^* \times (\vec{j}_i \times \vec{k}_i) \tag{2-15}$$

where g_i^* is the reciprocal metric tensor the corresponding crystal ($i = P, D$).

$$g^* = \begin{pmatrix} \boldsymbol{a}^* \cdot \boldsymbol{a}^* & \boldsymbol{a}^* \cdot \boldsymbol{b}^* & \boldsymbol{a}^* \cdot \boldsymbol{c}^* \\ \boldsymbol{b}^* \cdot \boldsymbol{a}^* & \boldsymbol{b}^* \cdot \boldsymbol{b}^* & \boldsymbol{b}^* \cdot \boldsymbol{c}^* \\ \boldsymbol{c}^* \cdot \boldsymbol{a}^* & \boldsymbol{c}^* \cdot \boldsymbol{b}^* & \boldsymbol{c}^* \cdot \boldsymbol{c}^* \end{pmatrix} \quad (2\text{-}16)$$

Here, $\boldsymbol{a}^*$, $\boldsymbol{b}^*$, $\boldsymbol{c}^*$ are the three basis vectors of the reciprocal space of the crystal.

Then, the three basis vectors '*i, j, k*' should be normalized to unit length and the coordinate transformation matrices M_P and M_D can be written as:

$$M_P = (\vec{\imath}_P \quad \vec{\jmath}_P \quad \vec{k}_P) \quad (2\text{-}17)$$

$$M_D = (\vec{\imath}_D \quad \vec{\jmath}_D \quad \vec{k}_D) \quad (2\text{-}18)$$

with the basis vectors as columns in the matrice.

Thus, the coordinate transformation matrix M^{OR} can be obtained with Equation (2-19).

$$M^{OR} = M_P * (M_D)^{-1} \quad (2\text{-}19)$$

2.2.3 Stereographic projection

In the present work, the stereographic projection was used to demonstrate the projection of a vector (or a plane normal) in the three-dimensional (3D) space to the equatorial plane of a sphere in a two-dimensional (2D) map, as illustrated in **Fig. 2.8**. As an example, the *'XOY'* is

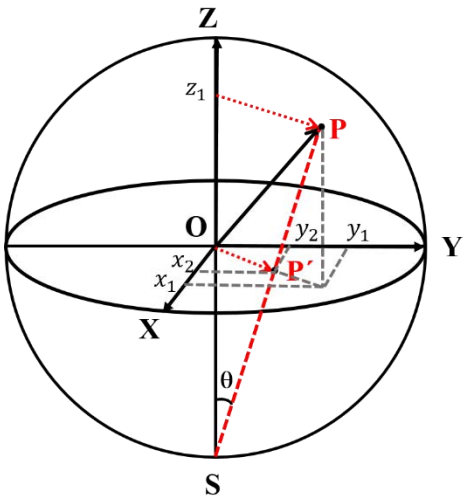


Fig. 2.8 Illustration of the stereographic projection on the equatorial plane *'XOY'* of vector OP in a unit sphere. Point *P'* is the projection of the pole P of vector OP on the equatorial plane and point *S* is the south pole of the projection sphere.

the projection plane of the stereographic projection and the OP represents an arbitrary vector in the 3D orthonormal reference *'X- Y- Z'*. Its corresponding projection P' is the intersection of the projection plane *'XOY'* with the vector of PS, where P is the pole of the vector on the sphere and S is the south pole of the projection sphere, as seen the **Fig. 2.8**.

$$x_1^2 + y_1^2 + z_1^2 = 1$$
$$\frac{x_1}{x_2} = \frac{y_1}{y_2}$$
$$\tan\theta = \frac{\sqrt{x_1^2 + y_1^2}}{1} = \frac{\sqrt{x_2^2 + y_2^2}}{1}$$

Thus, the coordinates of P' (x_2, y_2), with respect to the 2D coordinate system of the projection plane *'XOY'*, can be determined with the coordinates of OP (x_1, y_1, z_1) in the 3D reference S by the follow Equation (2-20).

$$x_0 = \frac{x}{1 + |z|}$$
$$y_0 = \frac{y}{1 + |z|} \tag{2-20}$$

For a crystalline plane (*h k l*), the normal vector ***n*** should be calculated firstly to plot its projection with the following equation:

$$\boldsymbol{n} = g^* \times \begin{pmatrix} h \\ k \\ l \end{pmatrix} \tag{2-21}$$

Then the stereographic projection of a given plane (*h k l*) could be determined according to the Equations (2-21).

2.2.4 Deformation gradient tensor

The deformation gradient tensor is used to describe a deformation process. For a clear illustration, the deformation gradient tensor is denoted by $F_{P\to D}^{R}$, where the superscript R indicates the reference system '*i-j-k*', P represent the undeformed domain and D is the corresponding deformed domain. The determination of the deformation gradient tensor is shown in **Fig. 2.9**, where $\boldsymbol{V_P}$ represents an arbitrary undeformed vector, and the corresponding vector after deformation is indicated by $\boldsymbol{V_D}$. The reference *R*, defined by basis vectors '*i, j, k*',

is an arbitrary coordinate system. If we suppose the coordinates of vector $\boldsymbol{V_P}$ with respect to reference *R* are $[X_1\ X_2\ X_3]_R$, the vector $\boldsymbol{V_D}$ could be expressed by $[x_1\ x_2\ x_3]_R$ after deformation. By definition, the deformation gradient tensor $F^R_{P\to D}$ could be expressed as Equation (2-22).

$$F^R_{P\to D} = \frac{\partial V_D}{\partial V_P} = \begin{bmatrix} \frac{\partial x_1}{\partial X_1} & \frac{\partial x_1}{\partial X_2} & \frac{\partial x_1}{\partial X_3} \\ \frac{\partial x_2}{\partial X_1} & \frac{\partial x_2}{\partial X_2} & \frac{\partial x_2}{\partial X_3} \\ \frac{\partial x_3}{\partial X_1} & \frac{\partial x_3}{\partial X_2} & \frac{\partial x_3}{\partial X_3} \end{bmatrix} \tag{2-22}$$

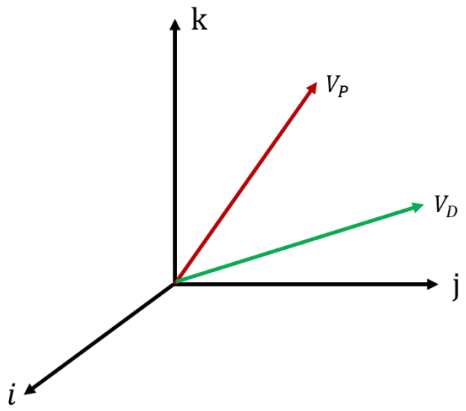


Fig. 2.9 Definition of the deformation gradient tensor $F^R_{P\to D}$. $\boldsymbol{V_P}$ represents an arbitrary undeformed vector, and the corresponding vector after deformation is $\boldsymbol{V_D}$. The reference system '*i*-*j*-*k*' is an arbitrary coordinate system. The coordinate system is of right-handedness.

With the deformation gradient tensor $F^R_{P\to D}$, the deformed vector $\boldsymbol{V_D}$ can be calculated from its undeformed initial vector $\boldsymbol{V_P}$ with Equation (2-23).

$$V_D = F^R_{P\to D} * V_P \tag{2-23}$$

The structure transformation process from the parent phase to the product phase under a specific orientation relationship (OR) is seen as a homogeneous deformation. The lattice correspondences for the two phases can be established, and then the corresponding deformation gradient could be determined. Thus the deformation gradient can be mathematically derived as follows.

Firstly, according to the specific OR between the two phases, the orthonormal reference frame *R* '*i*-*j*-*k*' could be built based on the OR plane and the OR direction of the parent crystal,

as illustrated in **Fig. 2.10**. Then the three basis vectors '*i, j, k*' of the corresponding coordinate system can be expressed as i^p, j^p and k^p in reference system of the parent phase and i^d, j^d and k^d of product phase based on Equations (2-13) to (2-15). Then, based on the OR frame

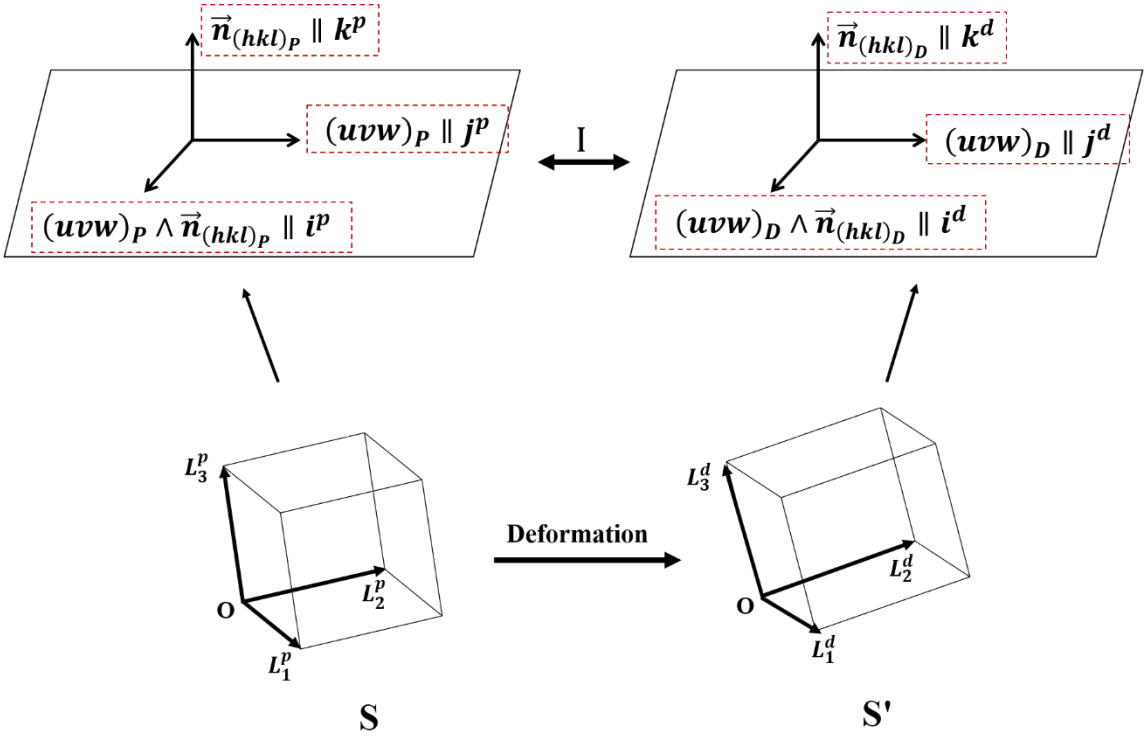


Fig. 2.10 Schematic of the crystal lattice deformation during phase transformation process. The parent crystal coordinate reference *S* defined by basis vector L_1^p, L_2^p and L_3^p; The product crystal coordinate reference *S′* defined by L_1^d, L_2^d and L_3^d; Reference *R* is defined with basis vector *i*, *j* and *k*.

R '*i-j-k*', lattice correspondences between the two phases can be worked out by finding out the three basis lattice vectors. For the parent phase, it is defined with the basis vectors L_1^p, L_2^p and L_3^p. After the structure transition, it is deformed to L_1^d, L_2^d and L_3^d of the product phase in the coordinate system *S′*, as illustrated in the figure. Finally, the orthonormal reference frame *R* '*i-j- k*' is set to the two coordinate systems *S* and *S′* and the basis vectors of the coordinate system before and after the deformation can be expressed as follows.

$$M_p = \begin{bmatrix} L_1^p * i^p & L_2^p * i^p & L_3^p * i^p \\ L_1^p * j^p & L_2^p * j^p & L_3^p * j^p \\ L_1^p * k^p & L_2^p * k^p & L_3^p * k^p \end{bmatrix}_R \tag{2-24}$$

$$M_d = \begin{bmatrix} L_1^d * i^p & L_2^d * i^p & L_3^d * i^p \\ L_1^d * j^p & L_2^d * j^p & L_3^d * j^p \\ L_1^d * k^p & L_2^d * k^p & L_3^d * k^p \end{bmatrix}_R \quad (2\text{-}25)$$

It should be noted that the three basis vectors '*i, j, k*' should be normalized to unit length. Thus, the deformation gradient tensor can be expressed as:

$$\boldsymbol{F} = \frac{M_d}{M_p} \quad (2\text{-}26)$$

Moreover, the deformation gradient tensor could be expressed in different references obtained by coordinate transformation, as expressed in Equation (2-27):

$$F^R = M^{R \to R_0} * F^{R_0} * M^{R_0 \to R} \quad (2\text{-}27)$$

where F^R and F^{R_0} are the deformation gradient tensor in references R and R_0, respectively, $M^{R \to R_0}$ and $M^{R_0 \to R}$ are the coordinate transformation matrices between the two references.

2.2.5 Trace analysis method

2.2.5.1 Interface analysis

The trace analysis method is used to determine the interfaces for the materials based on the EBSD technique, such as twin boundaries, the phase boundaries or habit planes, the slip planes. The interface plane determination is illustrated by the trace analysis method in **Fig. 2.11**. The orthonormal coordinate *'X- Y- Z'* is the sample coordinate. The TP represents the interface trace in the observation plane *'XOY'*. Stereographic projection with the projection plane of

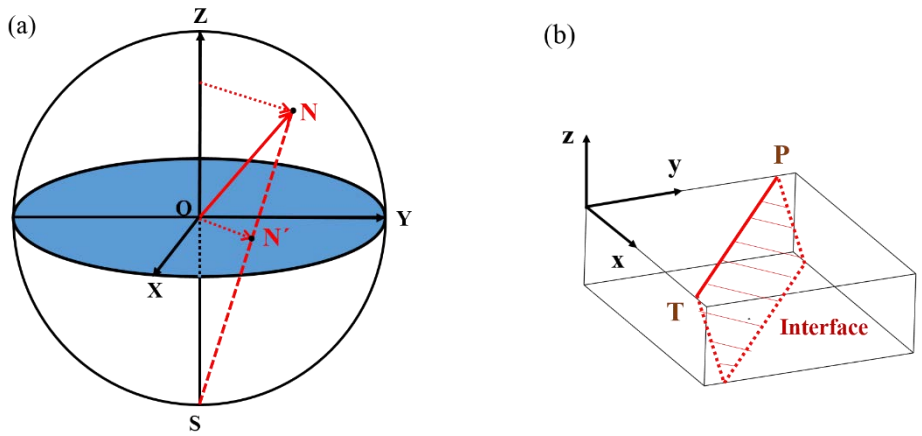


Fig. 2.11 Illustration of the interface in the pole figure (a) and the sample frame (b).

'XOY', as an example, where ON represents the normal vector of the interface plane in the orthonormal reference *'X- Y- Z'*. N' is the corresponding stereographic projection pole of the plane normal. Then the interface trace PT in **Fig. 2.11 (b)** is perpendicular to line ON' in **Fig. 2.11 (a)**. Therefore, the interface plane between the crystals can be estimated by comparing the orientation of the observed interface trace with a stereographic projection of a supposed plane.

2.2.5.2 Dislocation analysis

In the present work, the dislocation type of the material was identified with the trace analysis method using the known orientation data of the crystal based on the TEM technique. As we know, only dislocation lines can be seen using the TEM. Thus, the dislocation lines were always used to determine the type of the dislocation. In the present work, the dislocation types of the FCC crystal are analyzed using the trace analysis method. **Fig. 2.12** illustrates the coordinate transformation of the same dislocation lines based on the TEM image coordinate system *'X_t-Y_t-Z_t'*, the sample coordinate system *'X- Y- Z'* and the crystal coordinate system *'a-b-c'*. The typical types of dislocations of the FCC crystal are list in the **Table 2.3**. According to the table, the typical dislocation lines could be obtained as L_c (a, b, c) in the crystal coordinate system. If the Euler angles (φ_1, Φ, φ_2) of the crystal coordinate system with respect to the sample holder coordinate system and the rotation angle (θ, 0, 0) from the sample holder coordinate system to the TEM image coordinate system are known, as illustrated in **Fig. 2.12**, the theoretical dislocation line projection L_t on the TEM image coordinate system could be calculated the following equations.

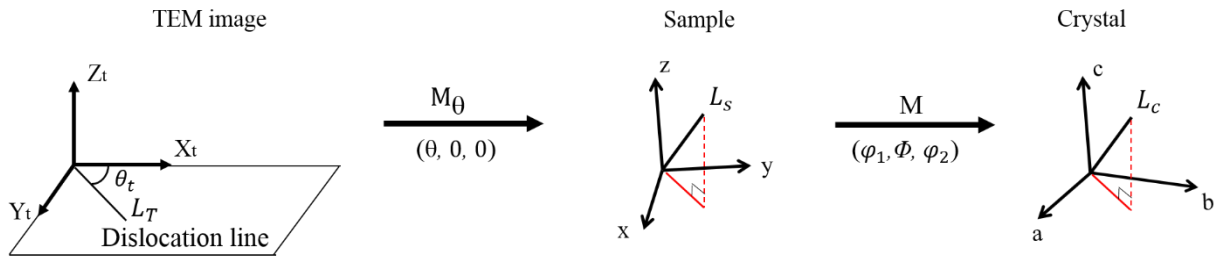


Fig. 2.12 Schematic of coordinate transformation for the same dislocation lines *L* based on the TEM image coordinate system, the sample coordinate system and the crystal coordinate system.

$$L_t = M_\theta * \mathrm{M} * S_i * L_c \qquad (2\text{-}28)$$

According to Equation (2-5), the coordinate transformation matrices M_θ and M can be obtained. Thus, the typical dislocation line expressed on the TEM image coordinate system L_t (x, y, z) can be calculated. Thus the angle θ_t between the dislocation line and the X_t axis of the TEM image coordinate system can be expressed determined.

$$\theta_t = \cot(y/x) \tag{2-29}$$

Through comparing the calculated θ_t of the theoretical dislocation with the measured angle of the observed dislocation line in the TEM image, the dislocation types can be determined.

Table 2.3 The typical type dislocations of the FCC crystal

Slip system	Burgers Vector *b*	Dislocation Line	
{111}<1$\bar{1}$0>	<1$\bar{1}$0>	<11$\bar{2}$>	Edge
		<1$\bar{1}$0>	Screw
{111}<11$\bar{2}$>	<11$\bar{2}$>	<1$\bar{1}$0>	Edge
		<11$\bar{2}$>	Screw

2.2.6 Twinning elements

For twins, their twinning mode can be fully defined by the twinning elements. These are K_1 - the twinning plane, η_1 - the twinning direction, K_2 - the conjugate twinning plane, η_2 - the conjugate twinning direction, P - the plane of shear and γ - the magnitude of shear, as shown in **Fig. 2.13**. According to the definition of twin, two twin related crystals should possess at least one 180° misorientation angle ω.

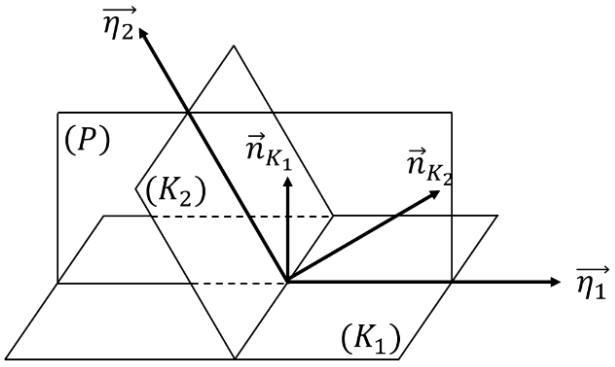


Fig. 2. 13 Illustration of twinning elements.

2.2.7 Hexagonal coordinates

The Bravais lattice basis of hexagonal crystals are always expressed in two ways. The one uses a three-axis coordinate system, where the (H K L) represents an arbitrary plane and the <U V W> represents an arbitrary direction in the hexagonal basis. The other way uses a four-axis basis, where the (h k i l) represents an arbitrary plane and the <u v t w> represents an arbitrary direction in the hexagonal structure. The relation between the three Miller indices of the three-axis coordinate system and the four Miller indices of the four-axis coordinate system can be obtained by the following Equations.

For the direction indices:

$$u = \frac{2*U-V}{3}$$

$$v = \frac{2*V-U}{3}$$

$$t = -(u+v)$$

$$w = W \tag{2-30}$$

$$U = u - t \qquad V = v - t \qquad W = w \tag{2-31}$$

For the plane indices:

$$h = H \qquad k = K \qquad i = -(H + K) \qquad l = L \tag{2-32}$$

$$H = h \qquad K = k \qquad L = l \tag{2-33}$$

Chapter 3 Microstructure and crystallographic characteristics of Cu-40％Zn alloy after the ECP treatments

3.1 Introduction

During the phase transformations (displacive or diffusive) process, specific orientation relationships (ORs) will be respected by the two end phases to minimize the lattice distortion energy for the structure change. In many cases, different ORs are respected by the same phase transformation. Thus, the selection role for the ORs during phase transformation process needs further investigation. In this chapter, a thorough study on the microstructure, phase transformation ORs and the crystallographic features of the α to β heating phase transformation was conducted in an annealed Cu-40%Zn alloy treated by high density Electric Current Pulse (ECP) treatments. The phase constituents and the microstructure of the alloy were explored firstly. Then the crystal orientation of the phases was characterized and the corresponding phase transformation ORs of the Cu-40%Zn alloy were further investigated through crystallographic analyses. Finally, the characteristics of the β phase morphology was investigated with the trace analysis method.

3.2 Experimental

In this chapter, an annealed Cu-40%Zn sheet was used. It was further treated by ECP under the current densities of about 15.12 kA/ mm^2, 15.66 kA/ mm^2, 15.93 kA/ mm^2, 17.01 kA/ mm^2 and 17.28 kA/ mm^2, respectively, with the pulse duration of 117 μs, 118 μs, 118 μs, 125 μs and 150 μs, correspond to the temperature of about 550°C, 588°C, 642°C, 876°C and 899°C. The detailed information on sample preparation can be found in §2.1.2 (p23). The phase constituents and their lattice constants of the samples were analyzed by XRD at room temperature. The software Jana 2006 was used to determine the lattice constants. The chemical composition of the constituent phases was analyzed by the electron probe microanalysis using an FEG-EPMA instrument. The microstructural examinations and crystallographic orientation characterization were performed by SEM and EBSD. The nano scaled microstructural and crystallographic

features of the constituent phases were analyzed using TEM. The atomic correspondences for the structure transformation from the parent α phase to the product β phase were analyzed using the Crystal Maker® software.

3.3 Results

3.3.1 Phase constituents and lattice constants

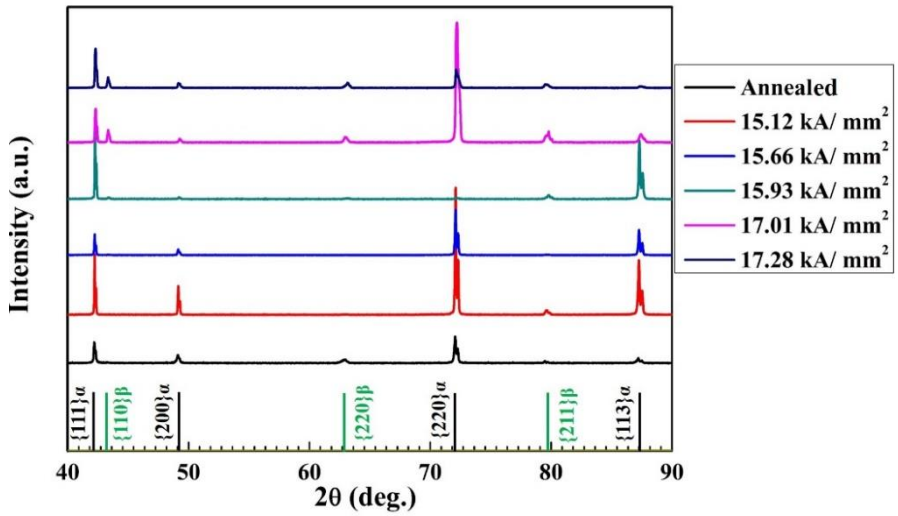


Fig. 3.1 X-ray diffraction patterns of the annealed and the ECP treated samples. The ideal peak positions of the α and the β phase were indicated with the color lines (black: α phase; green: β phase) at the bottom of the figure.

Fig. 3.1 displays the X-ray diffraction patterns of the samples before and after the ECP treatments at room temperature. It should be mentioned that as the patterns were measured from the bulk samples, the intensities of the peaks are strongly affected by the local texture of the measured regions, thus the corresponding peak intensities from sample to sample change. It is seen from the patterns that all the samples contain two phases (FCC α and BCC β). After the ECP treatment, the $\{110\}_\beta$ diffraction peaks appeared. With the peak positions, the lattice constants of the two phases in the samples without and with the ECP treatments were calculated and listed in **Table 3.1**. It is seen that the lattice constants of the two phases change very slightly with the ECP treatment. Those of the α phase decrease with the increase of the current density, whereas those of the β phase decrease first from the initial state and then increase with the increase of the current density. These measured lattice constants of the parent and the product phases allow accurate analyses of the lattice strains for the phase transformation induced by the

ECP, as demonstrated later.

Table. 3.1 Lattice constants of α and β phase in the annealed and in the ECP treated samples.

Electric Current Density (kA/mm^2)	α	β
0	3.702612	2.951775
15.12	3.703542	2.921082
15.66	3.701506	2.928865
15.93	3.701626	2.944449
17.01	3.698314	2.948694
17.28	3.699182	2.950145

3.3.2 Microstructure characteristics

3.3.2.1 Annealed microstructure

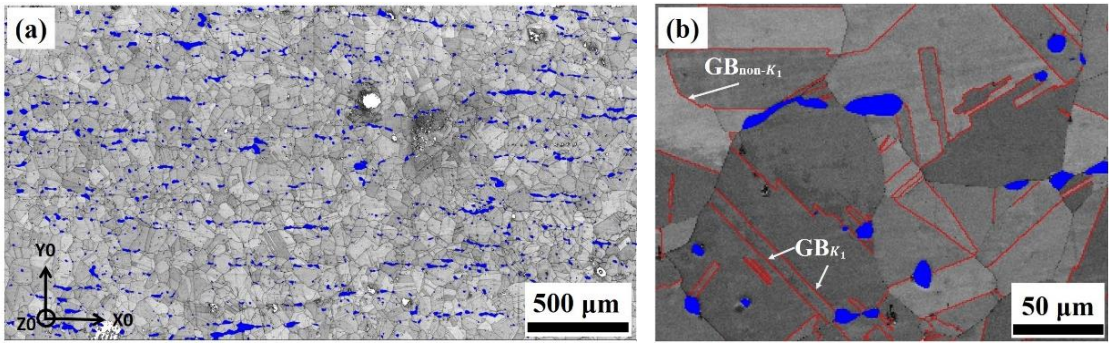


Fig. 3.2 (a) and (b) SEM-EBSD micrographs of annealed Cu-40%Zn alloy, where the β phase is in blue whereas the α phase is in gray represented with its EBSD band quality index contrast, and Σ3 boundaries are in red (b).

Fig. 3.2 (a) and **(b)** show the EBSD micrographs of the annealed Cu-40%Zn alloy, where the β phase is in blue and the α phase in gray (EBSD band quality index contrast). It can be seen that the annealed microstructure is mainly composed of α phase (about 96.21%) with equiaxed grains. The β phase is much less in quantity (about 3.79%) and located at the α grain boundaries and triple-junctions, forming bands along the previous hot rolling direction, as shown in **Fig. 3.2 (a)**. Within the α grains there are always long and straight Σ3 (<111> 60°) boundaries, as outlined in red in **Fig. 3.2 (b)**. This indicates that the α grains contain {111} <11$\bar{2}$> twins as two FCC crystals possessing a disorientation of 60° around the <111> axis is {111}<11$\bar{2}$> twin related. Occasionally, curved Σ3 boundaries appear as grain boundaries. According to the coincidence with the {111} twinning plane K_1, these Σ3 boundaries can be

further classified into two types. Hereafter those coincident with the K_1 plane boundaries are denoted GB_{K1} and those not coincident with the K_1 plane non-K_1-Σ3 grain boundaries are denoted $GB_{non\text{-}K1}$, as indicated in **Fig. 3.2 (b)**.

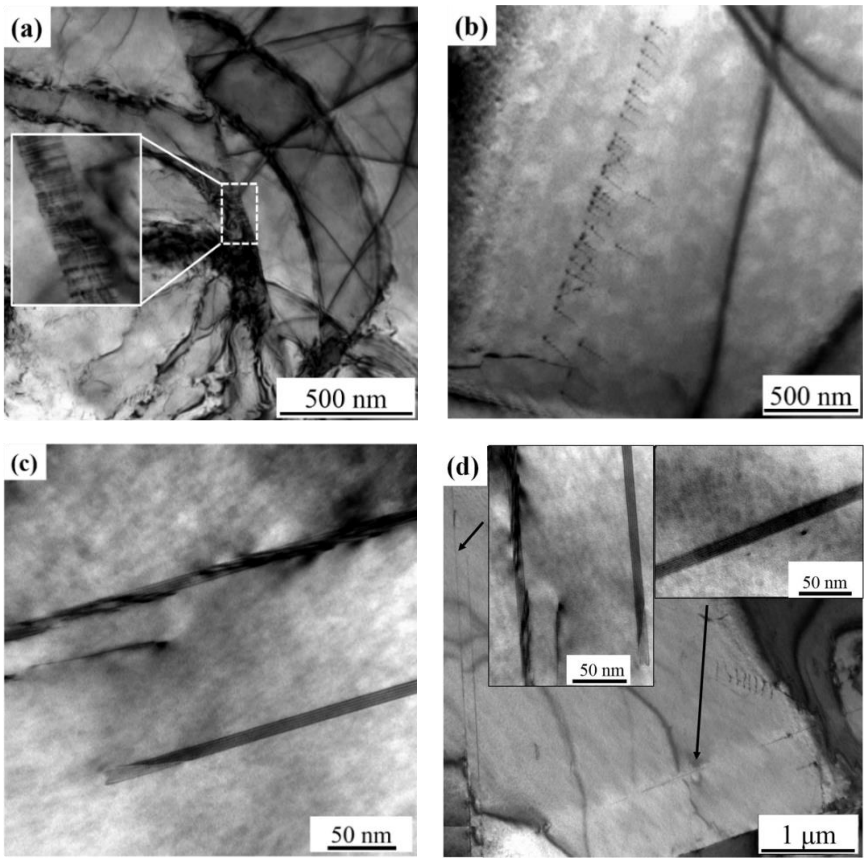


Fig. 3.3 TEM bright field micrographs of two kinds of crystal defects on α grain boundaries and in α grain interiors. (a) and (b) dislocation arrays, (c) and (d) stacking faults.

To investigate the sub-structure details of the α phase in the annealed Cu-40%Zn alloy, the TEM examinations were carried out. The examination results revealed that the annealed α matrix possesses two kinds of crystal defects located on α grain boundaries and in α grain interiors. Although the two kinds of defects are not numerous, their occurrence is certain. The one is parallel dislocation arrays that are mainly located on α grain boundaries, as shown with a typical example in **Fig. 3.3 (a)** and very occasionally located in the vicinities of α grain boundaries, as shown in **Fig. 3.3 (b)**. Further analysis demonstrated that such dislocations are mainly of $\{111\}<1\bar{1}0>_{\alpha}$ edge type. The other type of defects is stacking faults, as shown with a typical example in **Fig. 3.3 (c)** and **(d)**. Those stacking faults were observed within the α matrix and displayed different orientation. Trace analysis of the stacking faults confirmed that

they are of $\{111\}<11\bar{2}>_{\alpha}$ type that is typical for FCC low stacking fault metals, such as the α phase of the present alloy. This kind of stacking faults evidences the existence of the $\{111\}<11\bar{2}>_{\alpha}$ partial dislocations that are located along the boundaries between the faulted and non-faulted regions.

3.3.2.2 Microstructures after ECP treatment

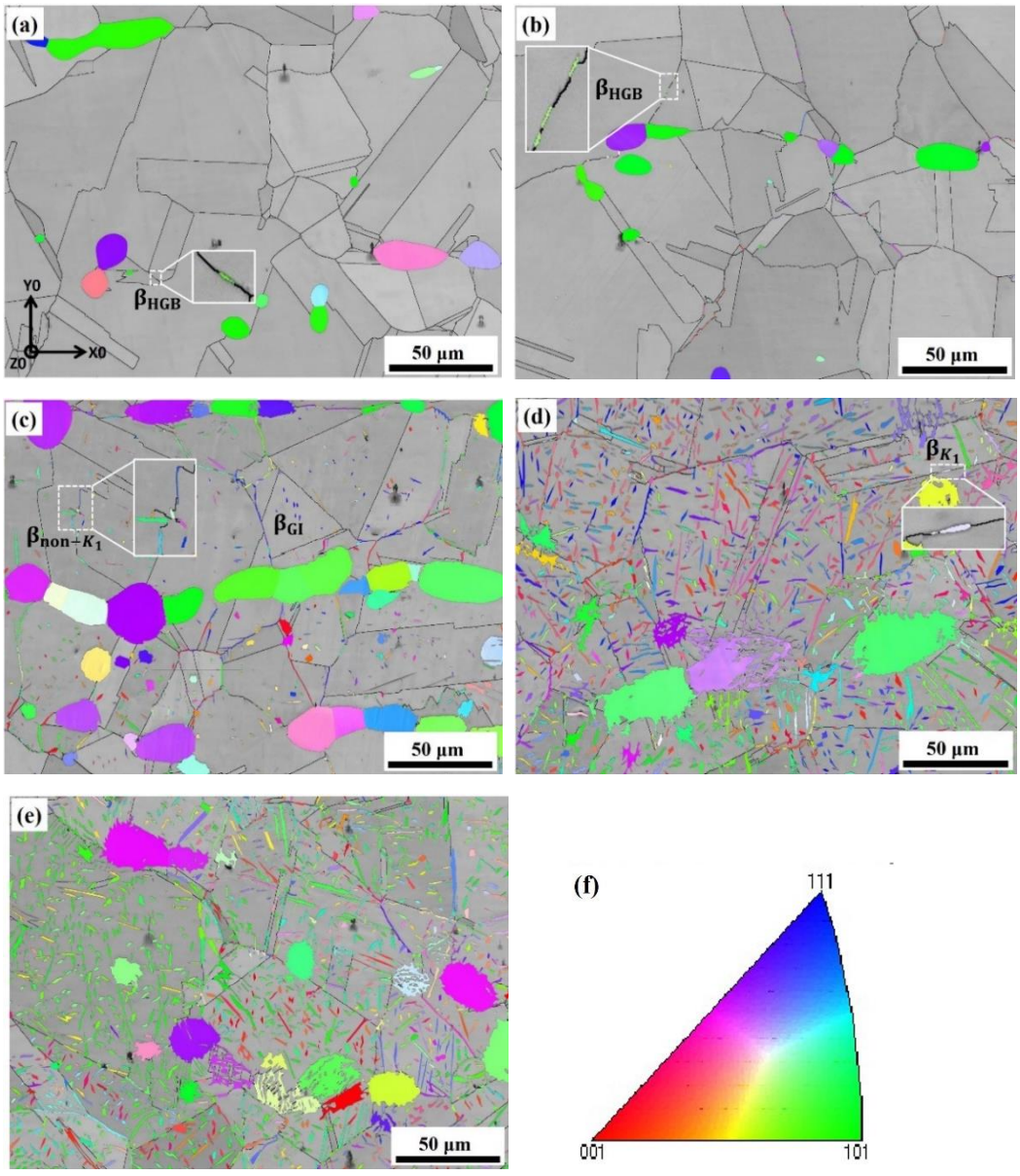


Fig. 3.4 SEM-EBSD micrographs of Cu-40%Zn alloy after ECP treatments where the α grains are in gray according to the EBSD band quality indices and the β phase in color according to its crystallographic orientation with respect to the X0 axis (X0 inverse pole figure (IPF) micrograph). (a) The ECP density j_{max}= 15.12 kA/ mm^2 (b) j_{max}= 15.66 kA/ mm^2 (c) j_{max}= 15.93 kA/ mm^2 (d) j_{max}= 17.01 kA/ mm^2 (e) j_{max}= 17.28 kA/ mm^2 and (f) the X0 IPF color code. The electric current direction is in the X0 direction.

Fig. 3.4 shows the EBSD micrographs of the Cu-40%Zn alloy after ECP treatments, where the α grains are in gray represented with the EBSD band quality index contrast and the β ones are in color according to their crystallographic orientations. Comparing with the annealed sample (**Fig. 3.2 (b)**), it can be found that some fine β precipitates appear in the α phase. It is noted that for those fine β precipitates, the amount of the precipitates increases with the increase of the electric current density, from 0.64% at 15.12 kA/ mm^2 to 11.5% at 17.28 kA/ mm^2, as shown in **Fig. 3.5**, the average area fractions of the β precipitates calculated from the EBSD results. With the increase of the amount of the β precipitates, the formation sites of the β precipitates also increases, from the random high angle (>10°) α grain boundaries (as indicated in the insert of **Fig. 3.4 (a)** and **(b)**) at low current density, to the non-K_1-Σ3 boundaries (as indicated in the insert of **Fig. 3.4 (c)**) and the α grain interiors (**Fig. 3.4 (c)** to **(e)**), and then to the K_1-Σ3 boundaries (as indicated in the insert of **Fig. 3.4 (d)**) at the high current density. Here the β precipitates at the α random high angle boundaries are denoted β_{HGB}, those at $GB_{non\text{-}K1}$ boundaries $\beta_{non\text{-}K1}$, those at GB_{K1} boundaries β_{K1} and those at α grain interiors β_{GI}. Such a nucleation sequence from low current to high current density demonstrates that the α grain boundaries are the preferred formation sites for the β precipitates, especially the high angle and non-coherent boundaries.

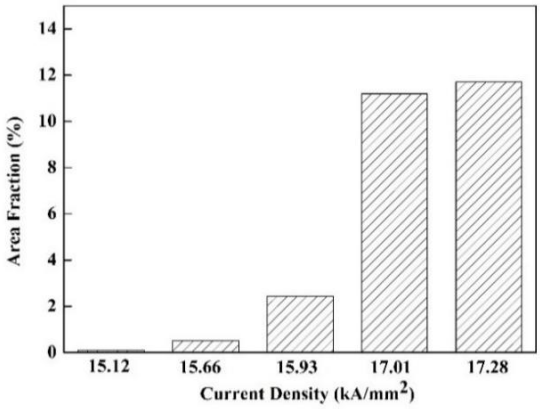


Fig. 3.5 Area fractions of the β precipitates obtained during ECP treatments.

In addition to the precipitation of the β phase during the ECP treatments, the morphology and size of the initial β grains also change. Some initial β grains become bigger or smaller at low current density and some tend to transform to α phase when the current density reached

17.01 kA/ mm^2 (**Fig. 3.4 (d)** and **(e)**). In the present work, only the α to β transformation was focused, the β to α transformation and the microstructure evolution of the initial β grains will not be included in the later sections.

3.3.3 Chemical composition distribution characteristics

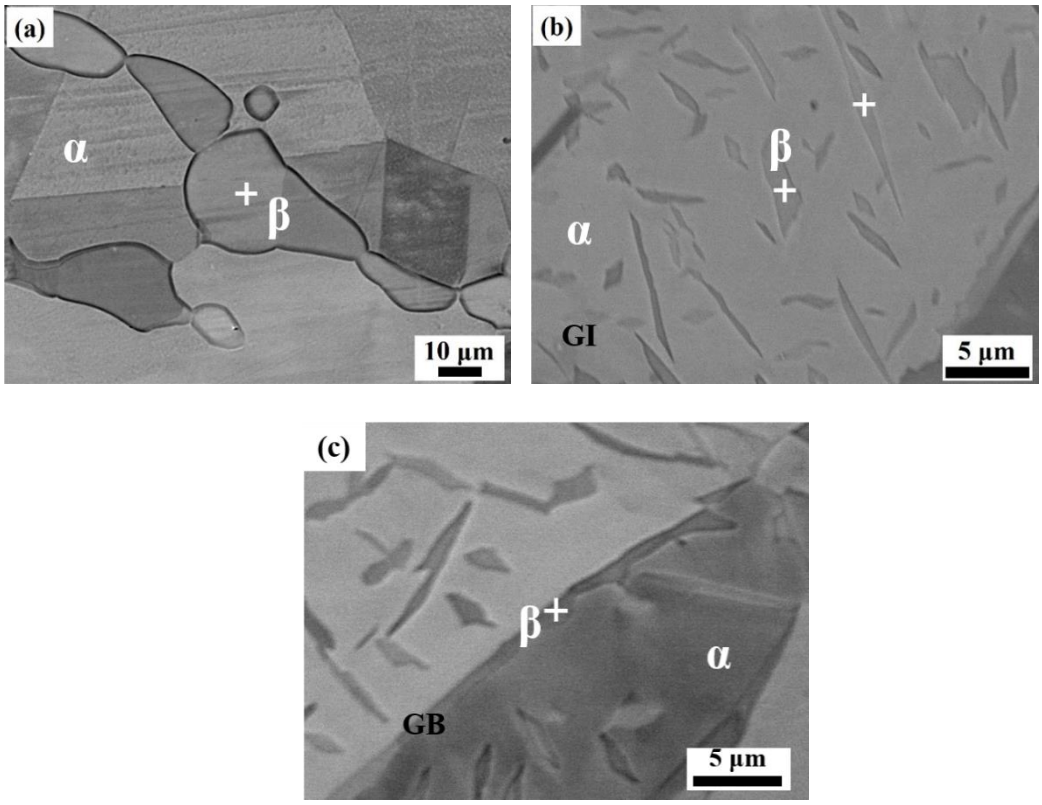


Fig. 3.6 Backscatter electron image of the annealed and ECPed Cu-40%Zn samples (a) annealed; (b) j_{max}= 17.01 kA/ mm^2 (β_{GI}); (c) j_{max}= 17.01 kA/ mm^2 (β_{GB}). The white crosses represent the measurement positions.

As the transformation from α to β phase is normally diffusional and the ECP induced transformation happened in a very short time from 118 μs to 150 μs depending on the electric current density, the composition of the ECP induced β phase was analyzed with respect to its parent phase α. **Table 3.2** shows the contents (the Cu and Zn) of the ECP induced β phase on the α grain boundaries and in the α grain interiors and the surrounding α matrix in the annealed and ECPed Cu-40%Zn samples. For reference, those of the residual β phase in the initial as-annealed sample were also measured and given in **Table 3.2**. Some example measurement positions indicated with the cross are displayed in **Fig. 3.6**. It can be found that the compositions of the ECP induced β phase on the α grain boundaries (β_{GB}) and in the α grain interiors (β_{GI}) are

quite close to those of the initial β phase of the annealed sample but different from those of the parent α phase, demonstrating that atom repartition happened during the ECP induced phase transformation although the transformation time was very short.

Table. 3.2 Chemical concentrations of Zn and Cu of the ECP induced β precipitates and the surrounding α matrix in the annealed and ECPed Cu-40%Zn samples.

Current Density (kA/mm^2)	α		β_{GI}		β_{GB}	
	Zn%	Cu%	Zn%	Cu%	Zn%	Cu%
0	38.72±0.31	62.58±0.43	46.83±0.75	57.40±0.22	46.83±0.75	57.40±0.22
15.93	39.40±0.56	62.33±0.68	43.71±1.72	59.51±1.63	44.83±0.51	58.06±0.68
17.01	37.74±0.47	63.69±0.66	45.12±0.66	57.34±0.59	45.17±0.53	57.64±1.00
17.28	37.01±0.87	64.43±0.58	45.41±0.65	57.82±0.43	43.25±4.57	60.58±5.11

3.3.4 Orientation relationship (OR) between α/ β

In consideration of the crystal structure features of the α phase (FCC) and the β phase (BCC), the Bain, the Nishiyama-Wassermann (N-W), the Kurdjumov-Sachs (K-S) and the Pitsch relations (as listed in **Table 3.3**) might be possible for the phase transformation in the investigated material. To evaluate the possibility of these orientation relationships (ORs), a large number of α and β grains were selected for the crystallographic analysis, using the measured orientations of the parent α phase and the β precipitates. It is found that one part of β precipitates respects the N-W with the surrounding α phase, whereas the other part respects the K-S ORs with the neighboring α phase, both with certain angular deviations (up to 5°), as shown in **Fig. 3.7 (a)** and **(b)**. **Fig. 3.7 (a)** and **(b)** displayed the β_{GB} along α grain boundaries and the β_{GI} in the α grain interiors where the α grains are in gray contrasted with the EBSD band quality indices and the β ones are in white. The colored contour lines around the β precipitates indicate the angular deviations from the exact ORs (K-S and N-W) where the red lines represented the K-S OR and the green line the N-W OR. The plane and direction parallelisms of the respective K-S and the N-W ORs are illustrated in the corresponding plane and direction pole figures in **Fig. 3.7 (c)** and **(d)**, using the example orientation data of the two phase measured by EBSD *i.e.* the $\{111\}_\alpha$ of the α phase and the $<011>_\beta$ of the β phase. From those maps it can be observed that the $\{111\}_\alpha$ poles of the α phase roughly coincide with the $\{011\}_\beta$ poles of the β_{GI}. For the

pole figures of ORs directions, there are two kinds of situations. One is the $[1\bar{1}0]_\alpha$ poles of the α phase almost coincide with the $[1\bar{1}1]_\beta$ poles of the β_{GB}, and the other is the $[11\bar{2}]_\alpha$ poles of the α phase coincide with the $[1\bar{1}0]_\beta$ poles of the β_{GI}. Thus, there are two kinds of ORs between the α phase and the β_{GI}: the K-S and the N-W OR for the ECP induced phase transformation. Due to the existence of the angular deviations, the actual transformation ORs deviate from the theoretical ORs, indicating that lattice strains are produced during the structure transition from the α phase to β phase.

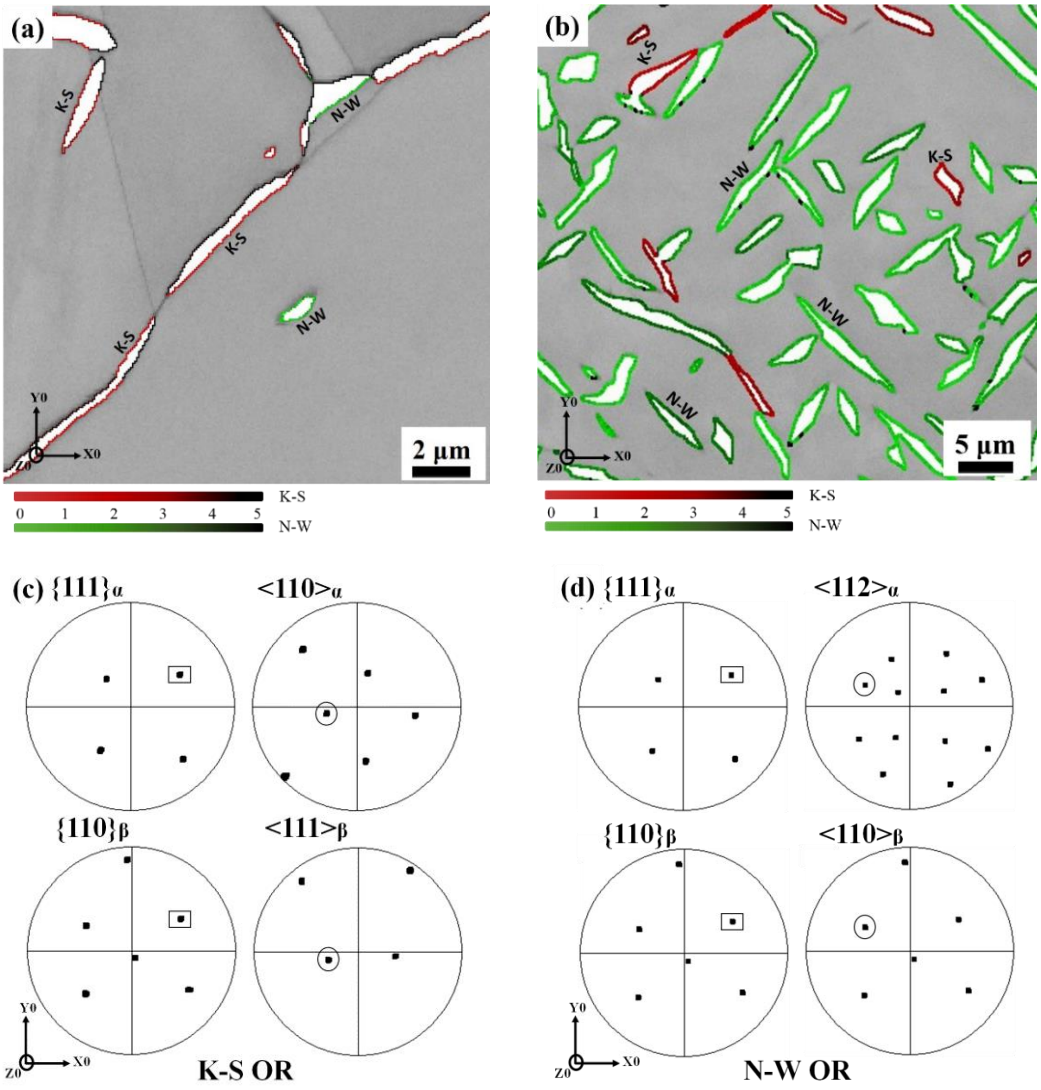


Fig. 3.7 SEM-EBSD micrograph of α and β precipitates in Cu-40%Zn alloy after ECP treatment. The α grains are in gray contrasted with the EBSD band quality indices and the β ones are in white. The colored contour lines around the β precipitates indicate the angular deviations from the exact OR. (a) β_{GB} along α grain boundaries, (b) β_{GI} in α grain interiors and (c) and (d) corresponding OR direction and plane pole figures of the parent α and the β precipitates obeying the K-S OR and the N-W OR, respectively. The overlapped poles are indicated with the rectangles (plane) and the circles (direction).

Table. 3.3 Possible ORs and their corresponding plane and in-plane direction parallelisms.

Possible ORs	**Parallel planes and in-plane directions**	
Bain relation	$(001)_\alpha$ //$(010)_\beta$	$<010>_\alpha$ //$<101>_\beta$
N-W relation	$(111)_\alpha$ //$(011)_\beta$	$<11\bar{2}>_\alpha$ //$<0\bar{1}1>_\beta$
K-S relation	$(111)_\alpha$ //$(011)_\beta$	$<1\bar{1}0>_\alpha$ //$<1\bar{1}1>_\beta$
Pitsch relation	$(101)_\alpha$ //$(1\bar{2}\bar{1})_\beta$	$<10\bar{1}>_\alpha$ //$<\bar{1}\bar{1}1>_\beta$

Table. 3.4 β /α phase boundary length fractions of β_{GB} and β_{GI} that obey different transformation ORs (the K-S: 42.85°/< 0.968 0.178 0.178 > and the N-W: 45.98°/< 0.976 0.083 0.201 >) at different deviation ranges (from both the rotation angle and the rotation axis) from the exact OR, obtained under different ECP treatments. For the β_{GI}, the statistics were counted from about 500 precipitates at 15.93 kA/ mm^2 to 2000 precipitates at 17.28 kA/ mm^2 and for the β_{GB}, the statistics were collected from around 600 precipitates.

	Electric Current Density (kA/mm^2)	**OR**	**0-3°**	**3-7°**
α/β_{GB}	15.66	K-S	76.2%	1.3%
		N-W	22.5%	
	15.93	K-S	78.6%	0.9%
		N-W	20.5%	
	17.01	K-S	73.3%	0.6%
		N-W	26.1%	
	17.28	K-S	60.1%	1.1%
		N-W	38.8%	

	Electric Current Density (kA/mm^2)	**OR**	**0-3°**	**3-7°**
α/β_{GI}	15.93	K-S	38.2%	1.1%
		N-W	60.7%	
	17.01	K-S	28.4%	0.5%
		N-W	71.1%	
	17.28	K-S	31.8%	0.4%
		N-W	67.8%	

Table 3.4 shows the detailed results the OR and the corresponding angular deviations from the exact OR of the β precipitates obtained from the examination of a large number of randomly

selected β precipitates along the α grain boundaries (β_{GB}) and in the α grain interiors (β_{GI}) under the ECP treatments. To visualize the different populations of the β precipitates with respect to the two ORs, the deviations of all the selected β precipitates from the ideal N-W OR (equivalent to a 45.98° rotation around the <0.976 0.083 0.201> axis) and also from the ideal K-S OR (equivalent to a 42.85° rotation around the <0.968 0.178 0.178> axis) are presented in the histograms and displayed in **Fig. 3.8**. It should be noted that both the deviations from the rotation angle and the rotation axis are considered. It is seen from **Table 3.4** and **Fig. 3.8** that

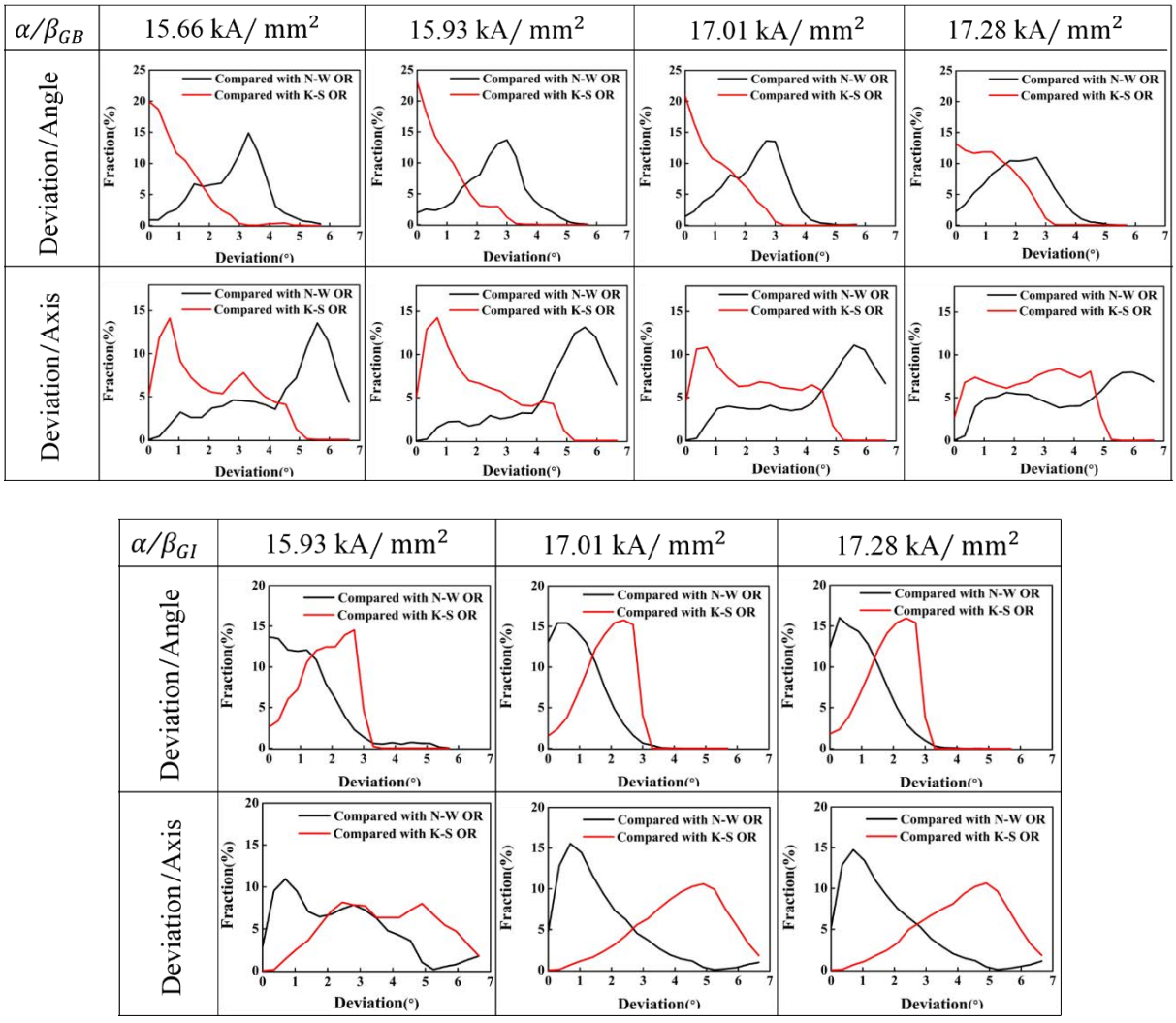


Fig. 3.8 Variations of β/α phase boundary length fractions of all the selected β_{GB} and β_{GI} with the deviations from the ideal N-W OR (equivalent to a 45.98° rotation around the <0.976 0.083 0.201> axis) (in black) and also from the ideal K-S OR (equivalent to a 42.85° rotation around the <0.968 0.178 0.178> axis) (in red) under different ECP treatments. The deviations are both from the rotation angle and the rotation axis. For the β_{GI}, the statistics were counted from about 500 precipitates at 15.93 kA/ mm^2 to 2000 precipitates at 17.28 kA/ mm^2 and for the β_{GB}, the statistics were collected from around 600 precipitates.

most β_{GB} respects the K-S OR whereas the most β_{GI} obeys the N-W OR. In addition, the β_{GI} obeying the K-S OR are located in the vicinities of the α grain boundaries. These results demonstrate that the transformation OR of the β precipitates induced by the ECP is rather selective, depending on the formation location. As at these sites we found different types of dislocations, the selection of the OR should be related to the specific dislocations.

3.3.5 Morphology of intragranular β (β_{GI})

Here, the morphologies of the intragranular β (β_{GI}) precipitates were mainly investigated. From large scaled microstructure examinations (not shown here), it can be found that the β_{GI} precipitates are monolithic in bar shape as shown in **Fig. 3.4**. By statistical trace analysis, it is further found that the precipitates are encased in two pairs of parallel planes, $\{211\}_\alpha$ and $\{311\}_\alpha$ of α phase as the prismatic planes. These planes correspond to the respective $\{112\}_\beta$ and $\{2\bar{1}1\}_\beta$ (or $\{12\bar{1}\}_\beta$) planes of the β phase, as shown with the corresponding pole figures of the example β_{GI} precipitates in **Fig. 3.9**. In the figures, the microstructures of the β_{GI} precipitates are displayed in colors according to their crystallographic orientations. The surfaces of the precipitates are illustrated with the dashed lines and the traces the solid lines in the consistent colors. The corresponding poles of the surface planes are indicated with the circles. According to the orientation of the parallel directions from the two phases ($<112>_\alpha$ // $<111>_\beta$) under the N-W transformation OR, *i.e.*, the OR direction, enclosed in the black boxes in **Fig. 3.9**, with respect to the surface planes $\{311\}_\alpha$ and $\{211\}_\alpha$, the β_{GI} precipitates are further classified into three types referred to as precipitate A, B and C, as illustrated in **Fig. 3.9**. The geometrical relations between the surface planes and the OR direction of the three types of β_{GI} are summarized in **Table 3.5**.

Table. 3.5 The geometrical relations between the OR direction $<112>_\alpha$ and the surface planes of the three types of precipitates (A, B and C) described with the angles between this direction and the corresponding surface plane normal directions $\vec{n}$.

	$<112>_\alpha$ Λ Shear Direction	**$<112>_\alpha$ Λ $\vec{n}_{\{113\}_\alpha}$**	**Shape**
A	10°	80°	Long Bar
B	5°	80°	Short Bar
C	10° - 90°	10° - 90°	Irregular

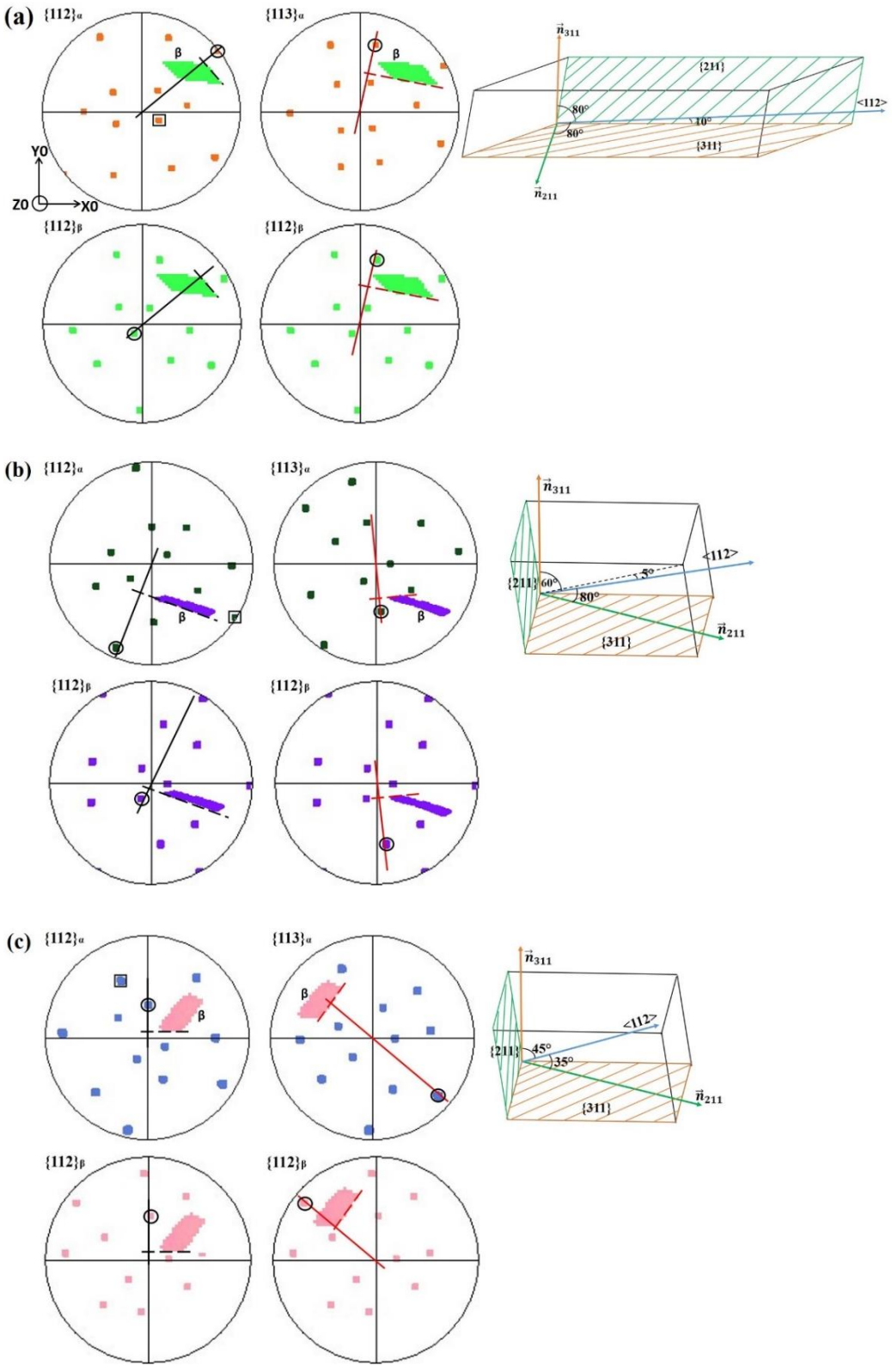


Fig. 3.9 $\{112\}_\alpha$ and $\{113\}_\alpha$ pole figures of α phase possessing the three types of β precipitates (A, B and C) and their three-dimensional illustrations. (a) precipitate Type A, (b) Type B and (c) Type C. The dash lines outline the surface plane traces of the precipitates and the solid lines connect the center of the pole figures with the poles corresponding to the surface planes and perpendicular to the surface plane traces with the same color.

For Type A, the precipitates are in long bar shape and the N-W OR direction ($<112>_{\alpha}$) is nearly parallel to the two pairs of surface planes. For Type B, the length of the bars is much shorter. The OR direction is nearly parallel to one pair of the surface plane ($\{211\}_{\alpha}$) but largely deviated from the other pair ($\{311\}_{\alpha}$). For Type C, the shape is not regular and the OR direction is not fixed with respect to the two pairs of surface planes. It changes from one case to another. The occurrences of the three types of precipitates are also different under different current densities, as displayed in **Table. 3.6**. Type A is in absolute majority and the other two are in minority. However, with the increase of the current density the occurrence of Type A decreases. It should be mentioned that with the increase of the current density, the number and sizes of β_{GI} drastically increased and the precipitates formed all over the parent α grains. Thus the lattice of the parent grains should be largely distorted due to the lattice mismatch between the two phases (the lattice deformation will be detailed later). The lattice distortions should impose constraints on the elongation of the precipitates. This suggests that the preferred elongation direction of the β precipitates is close to the OR direction.

Table. 3.6 The number percentage of the three types of β_{GI} obtained in different current density treatments.

Electric Current Density (kA/mm^2)	**A**	**B**	**C**
15.93	79.59%	8.16%	12.24%
17.01	72.46%	19.32%	8.21%
17.28	57.91%	20.89%	21.20%

3.4 Discussion

These experimental observations clearly demonstrate that there is a phase transformation occurred in the annealed Cu-40%Zn alloy during the ECP treatment. Since the application of ECP would input high-energy into the materials, the system of the sample will be in an unstable state during the passage of the current. Thus, the lattice strain, the thermal effect and the electrical effect of the ECP play an important role in the formation of the β precipitates during the heating phase transformation process.

3.4.1 The thermal effect of the ECP

Table 3.7 shows the average temperature value caused by the ECP. It is clear that the temperature of the samples rises with the increase of the electric current density. Meanwhile, from the percentage increase of the β phase with the current density (in **Fig. 3.5**), it is reasonable to deduce that the joule heating provides temperature and energy conditions for phase transformation during the ECP process. The detailed calculation process on sample temperature induced by the ECP can be found in § 2.1.2 (p23).

Table. 3.7 The temperature value of the sample induced by the ECP.

Electric Current Density (kA/mm^2)	T (°C)
0	25
15.12	550.19
15.66	588.37
15.93	642.83
17.01	876.95
17.28	899.57

3.4.2 The electrical effect of the ECP

As known, the electric effect of the ECP also play an important role on the occurrence of phase transformation. Here, we used the model developed by Dolinsky [34-38] and by Qin [39-41] to explain the formation of the β precipitates in α phase. **Fig. 3.10 (a)** and **(b)** show schematically the electric current distribution when the electric current passes through a pure α phase and a α phase with a spherical nucleus of a β precipitate, respectively. The sphere radius of the α phase is R and that of the β precipitate is r (r << R).

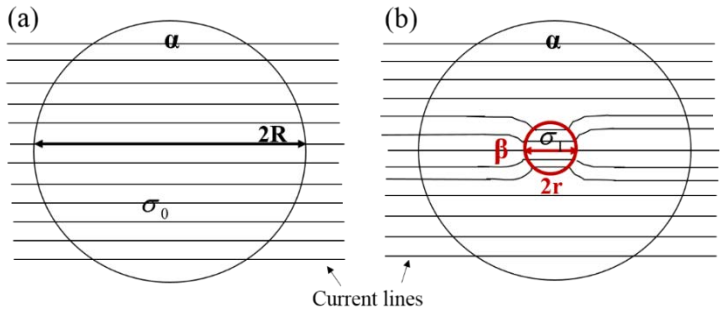


Fig. 3.10 Current distributions during the passage of electric current through (a) a α phase with sphere radius R, (b) a new β phase with sphere radius r at the center (r << R).

When an electric current passes through a conductor, the energy change of the system can be expressed by the following equations [34-41]:

$$\Delta G = \Delta G_0 + \Delta G_e \quad (3\text{-}1)$$

$$\Delta G_e = \mu_0 g\xi(\sigma_0, \sigma_1) j^2 \Delta V \quad (3\text{-}2)$$

$$\xi(\sigma_0, \sigma_1) = (\sigma_0 - \sigma_1)/(\sigma_1 + 2\sigma_0) \quad (3\text{-}3)$$

where ΔG_0 is the Gibbs free energy change in current-free system, ΔG_e is the Gibbs free energy change due to the change of the current distribution caused by the nucleus formation and expressed in Equation (3-2), μ_0 is the magnetic susceptibility in vacuum, $\Delta V = (4/3)\pi r^3$ is the volume of the new phase nucleus, *j* is the current density, and g (a, b) is a geometric factor. In this model, $\xi(\sigma_0, \sigma_1)$ is a factor which depends on the electric properties of the nucleus and the medium, where the σ_0 and σ_1 are the electrical conductivity of the α phase and the β precipitate as shown in **Fig. 3.10**. The sign of ΔG_e is dominated by $\xi(\sigma_0, \sigma_1)$ and it can be written as Equation (3-3). During the α to β phase transformation process, $(\sigma_\beta=\sigma_1) > (\sigma_\alpha=\sigma_0)$; that made $\xi(\sigma_0, \sigma_1) < 0$, so $\Delta G_e < 0$ according to Equation (3-2). Therefore, the value of ΔG is negative. That means the electric current can induce α to β phase transformation by providing additional Gibbs free energy decrease (also the transformation driving force). It further indicates that the application of ECP is favorable to the nucleation of the precipitates with higher conductivity during the phase transformation process.

It is worth noting that the electric current distribution will be changed in the deformed area with defects during the passage of the current. That will cause the local temperature of the deformed area to rise. As a result, an atom flow resulting from a temperature gradient (thermotransport) could occur. Thus, inhomogeneous temperature field in the sample is generated due to the existence of the crystal defects (such as dislocations, grain boundaries, etc.) during the passage of the high density electric current. That means the joule-heating of the α grain boundaries will be larger than the α grain interiors when a high density electric pulse passes in the annealed Cu-40%Zn alloy. Therefore, the fine β phase prefers to precipitate along the grain boundary of α phase as indicated in **Fig. 3.4 (a)** and **(b)**. Thus, α grain boundaries are the preferred nucleation sites for the β precipitates for the phase transformation.

3.4.3 The lattice strain effect

Under the condition of the present initial microstructure of the Cu-40%Zn alloy, the transformation OR of the β precipitates formed under the present ECP treatments are characteristic depending on the formation location. On α grain boundaries, the OR is mostly the K-S, whereas in α grain interiors, the OR is mostly the N-W, suggesting that the lattice distortion to realize the structure transformation from α phase to the β phase proceeds in different ways and makes use of different crystal defects. The different transformation ORs may represent different lattice strain paths for the structure transformation.

To further explore the transformation deformation, the lattice strains to form the β precipitates having a BCC structure from the α phase with an FCC structure under the two ORs (K-S and N-W) were analyzed using the lattice constants determined from the XRD diffraction measurements (**Table 3.1**) and represented with the deformation gradient tensor **A** expressed in the corresponding OR reference systems. **Fig. 3.11** shows the lattice correspondences of the two phases under the two ORs and the OR reference systems (*i*-*j*-*k*). For each OR reference system, *j* is set parallel to OR direction, *k* to the direction normal to the OR plane and *i* to the vector product of *j* and *k*. A general form of the deformation gradient tensor is given in Equation (3-4), where the diagonal element in the tensor a_{ii} (*i*=1, 2 and 3) represents an elongation (a_{ii}>1) or a contraction (a_{ii}<1) in the direction of *i* when the lattice change from α to β, whereas the off diagonal element a_{ij} (*i* and *j*=1, 2 and 3), represents a shear in the direction of *i* and on the plane normal to *j*.

$$A=\begin{bmatrix} a_{11} & a_{12} & a_{13} \\ a_{21} & a_{22} & a_{23} \\ a_{31} & a_{32} & a_{33} \end{bmatrix} \tag{3-4}$$

According to the measured lattice constants of the two phases in the samples (**Table. 3.1**), the deformation gradient tensors could be obtained by examining the lattice correspondences of the two phases under the corresponding OR (N-W and K-S) reference frames under different current density. Here, the deformation gradient tensor in the sample treated at 17.28 kA/mm^2 is used as example and listed in **Table 3.8**.

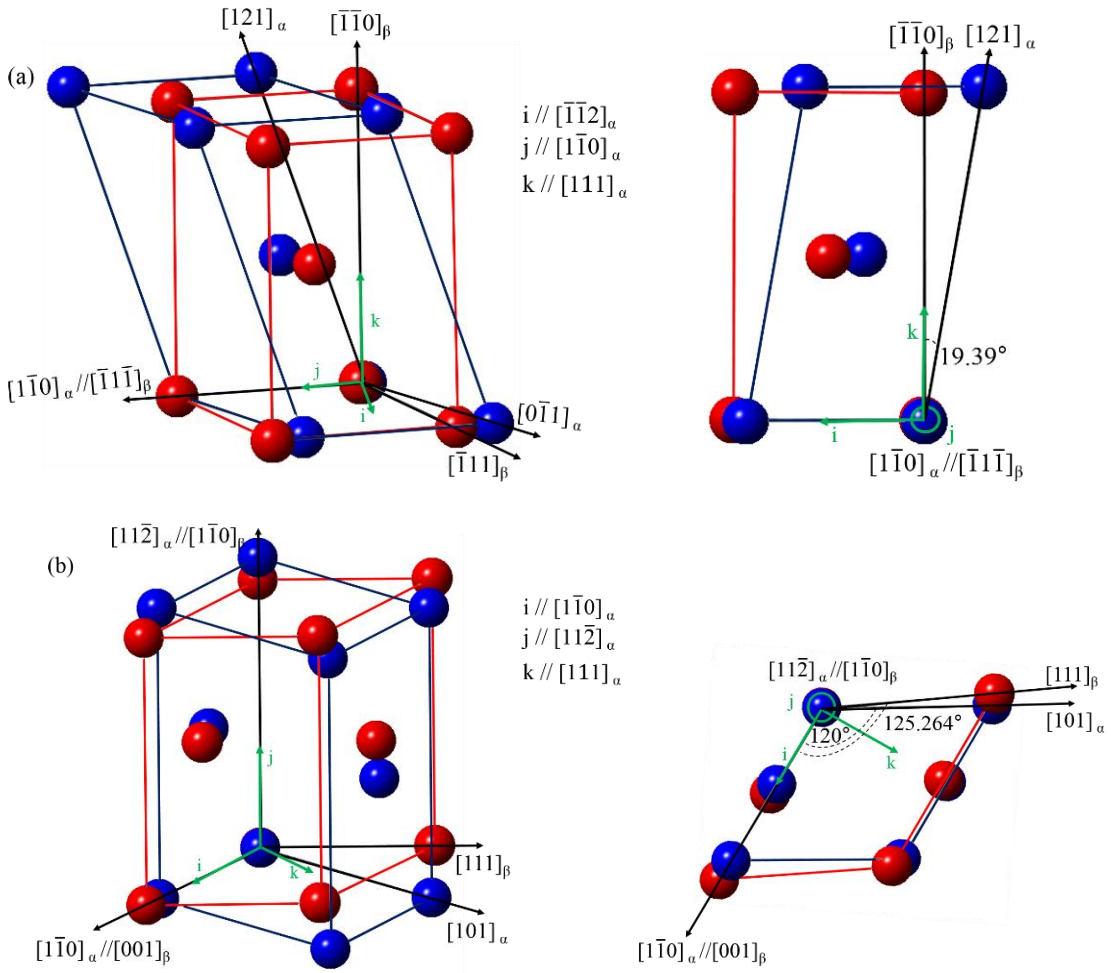


Fig. 3.11 (a) Lattice correspondences between α and β under the K-S (a) and under the N-W OR (b). The OR reference systems (*i*-*j*-*k*) are set with direction *i* parallel to the OR direction, *j* to the direction normal to the OR plane and *k* to the vector cross product of *i* and *j*. The lattice points of the α phase are in blue and those of the β phase in red.

Table. 3.8 Deformation gradient tensor of the structure deformation to form the β precipitates in the sample treated under j = 17.28 kA/ mm^2 under the K-S and under the N-W OR expressed in the K-S and the N-W OR reference frame, respectively.

OR	**Deformation Gradient Tensor**
K-S	$i // [\bar{1}\bar{1}2]$ $j // [1\bar{1}0]$ $k // [111]$
	$\begin{bmatrix} 1.0634 & 0 & 0.1880 \\ -0.1880 & 0.9767 & 0.2658 \\ 0 & 0 & 0.9767 \end{bmatrix}$
N-W	$i // [1\bar{1}0]$ $j // [11\bar{2}]$ $k // [111]$
	$\begin{bmatrix} 1.1279 & 0 & 0 \\ 0 & 0.9209 & 0.3256 \\ 0 & 0 & 0.9767 \end{bmatrix}$

Table. 3.9 Strain components of the deformation gradient tensor.

N-W path		K-S path	
Dilation $[1\bar{1}0]_\alpha$	0.1279	Dilation $[\bar{1}\bar{1}2]_\alpha$	0.0634
Dilation $[11\bar{2}]_\alpha$	-0.0791	Dilation $[1\bar{1}0]_\alpha$	-0.0233
Dilation $[111]_\alpha$	-0.0233	Dilation $[111]_\alpha$	-0.0233
Shear (111) $[\bar{2}11]_\alpha$	0.3256	Shear (111) $[1\bar{1}0]_\alpha$	0.2658
		Shear $(\bar{1}\bar{1}2)$ $[1\bar{1}0]_\alpha$	-0.1880
		Shear (111) $[\bar{1}\bar{1}2]_\alpha$	0.1880

It is seen that for the formation of the K-S β phase it requires an elongation of 0.0634 in the $[\bar{1}\bar{1}2]_\alpha$ direction (a_{11}) of the α lattice, a contraction of 0.0233 in the $[1\bar{1}0]_\alpha$ direction (a_{22}) and in the $[111]_\alpha$ direction (a_{33}). The transformation also requires three shear deformations, a shear of 0.1880 on the $(111)_\alpha$ plane and in the $[\bar{1}\bar{1}2]_\alpha$ direction (a_{13}), a shear of -0.1880 on the $(\bar{1}\bar{1}2)_\alpha$ plane and in the $[1\bar{1}0]_\alpha$ direction (a_{21}) and a shear of 0.2658 on the $(111)_\alpha$ plane and in the $[1\bar{1}0]_\alpha$ direction (a_{23}), as shown in **Table 3.9**. Clearly, the shear strains are much larger than those of the normal strains. Among the three shear strains, a_{23} is the largest. It should be noted that the shear system of a_{23} corresponds to the $\{111\}_\alpha/<1\bar{1}0>_\alpha$ slip system of FCC crystals, thus the existing $\{111\}_\alpha/<1\bar{1}0>_\alpha$ dislocation arrays found along the α grain boundaries should facilitate the structure transformation from the α phase to the β phase via the K-S path.

For the N-W β precipitates, the transformation requires the α lattice to elongate by 0.1279 in the $[1\bar{1}0]_\alpha$ direction (a_{11}), to contract by 0.0791 in the $[11\bar{2}]_\alpha$ direction (a_{22}), to contract by 0.0233 in the $[111]_\alpha$ direction (a_{33}) and to shear by 0.3256 on the $(111)_\alpha$ plane and in the $[11\bar{2}]_\alpha$ direction (a_{23}), as shown in **Table 3.9**. In addition, the shear deformation is much larger than the normal strains under the N-W path. Interestingly, the required shear system is $\{111\}_\alpha/<11\bar{2}>_\alpha$ that corresponds to the partial slip system of FCC crystals. It is known that Cu-40%Zn has relatively low stack fault energy. Stacking faults are one of the important crystal defects in this alloy, as observed in the α grain interiors in the present work. Thus, the existing $\{111\}_\alpha/<11\bar{2}>_\alpha$ stacking faults should be favorable for the formation of the β precipitates via the N-W path. In consequence, the existence of different dislocations in different locations in the as annealed Cu-40%Zn provide different pre-strain to facilitate the transformation via different strain paths and are at the origin of the selection of the transformation OR.

The morphology of the β precipitates obeying the N-W OR in the α grain interiors is also related to the characteristic lattice strain. As the shear deformation $\{111\}_\alpha/<11\bar{2}>_\alpha$ is the major lattice strain, the elongation of the N-W β precipitates in the shear direction generates less accumulated lattice distortion in the transformation front than the thickening of the precipitates in the directions perpendicular to the shear direction. Thus, the shear deformation restricts the thickening of the β precipitates and facilitates the elongation of the β precipitates along the shear direction during the growth process. However, such ideal morphology should be obtained at the beginning of the transformation when the matrix is distortion free. With the increase of the current densities or the prolongation of the transformation, the remaining α matrix becomes distorted due to the formation of the early β precipitates thus the growth of the newly formed β precipitates deviates from the low distortion growth direction in the stress free medium and the morphology changes.

3.5 Summary

In this part of the work, the crystallographic features of the phase transformation from the low temperature α phase to the high temperature β phase induced by electric current pulse (ECP) in an annealed Cu–40%Zn alloy was thoroughly investigated. With the increase the electric current density, substantial fine high-temperature β precipitates were remained to the room temperature due to the accelerated nucleation of the β phase during the transformation induced by ECP and the rapid cooling of the ECP treatment.

The ECP induced β precipitates formed in the α matrix follow different ORs depending on the formation site. At the α grain boundaries or their vicinities, the K-S OR is respected, whereas in the α grain interiors, the N-W OR is obeyed. In the former locations, $\{111\}_\alpha/<1\bar{1}0>_\alpha$ dislocation arrays are frequently observed, whereas in the latter stacking faults boarded with $\{111\}_\alpha/<11\bar{2}>_\alpha$ partial dislocations are often spotted. Analysis of the transformation lattice deformation revealed that under the different ORs, the lattice strain to realize the structure change for the α to β transformation is different. For the K-S strain path, the principal resistance is the shear strain on the $\{111\}_\alpha$ plane and in the $<1\bar{1}0>_\alpha$ direction, whereas for the N-W path, the principal obstacle is the shear on the $\{111\}_\alpha$ plane and in the $<11\bar{2}>_\alpha$ direction. Thus the

existing $\{111\}_\alpha$ /$<1\bar{1}0>_\alpha$ dislocation arrays provide the favorable pre-strains to facilitate the formation of the β precipitates via the K-S path. The existing $\{111\}_\alpha$ /$<11\bar{2}>_\alpha$ stacking faults offer the favorable pre-strains for the formation of the β precipitates via the N-W path, resulting in the selection of ORs for the α to β transformation.

With the present work, the correlation between the types of existing crystal defects (dislocations and stacking faults) and the transformation orientation relationships is confirmed. The roles of different dislocations in providing favorable pre-strain to contribute to the transformation strain process of the α to β transformation under different ORs were fully revealed. The methodology of the present work is applicable to phase transformations in many other metallic materials.

Chapter 4 Crystal defects produced by α to β phase transformation during ECP in Cu-40％Zn alloy

4.1 Introduction

The mesoscopic features of the α to β phase transformation of the Cu-40%Zn alloy treated by high density Electric Current Pulse (ECP) has been largely reveled, such as the microstructure characteristics, the chemical composition characteristics, the orientation relationships between α and β phases and the morphology of the intragranular β precipitates. So, in this chapter, the crystal defects in the α phase related to the α to β heating phase transformation induced by the ECP treatments was investigated. The crystal defects in the α phase under different electric current densities were explored by TEM firstly. Then, combining the experimental observation and the simulated results by *ab-initio* calculations, the impact of the phase transformation on the formation of the crystal defects were further investigated. Finally, the formation mechanism of the crystal defects and the relationship between the crystal defects and the α/β phase transformation were revealed through crystallographic analyses. The results provide new information on the crystal defects related to the α to β phase transformation in an ECPed Cu-40%Zn alloy.

4.2 Experimental

In this chapter, an annealed Cu-40%Zn sheet was used. It was further treated by ECP under the current densities of about 15.66 kA/ mm^2 and 17.01 kA/ mm^2, respectively, with the pulse durations of 118 μs and 125 μs, corresponding to the temperatures of about 588°C and 876°C. The detailed information on sample preparation can be found in §2.1.1 (p23). The microstructural examinations and crystallographic orientation characterization were performed by SEM-EBSD. Nano scaled microstructural and crystallographic features of the constituent phases were analyzed using TEM. The atomic scaled microstructures were analyzed by high-resolution STEM (HAADF). The atomic correspondences for the structural transformation from the parent α phase to the product β phase were analyzed using the Crystal Maker® software.

4.3 Results

4.3.1 Microstructural characteristics

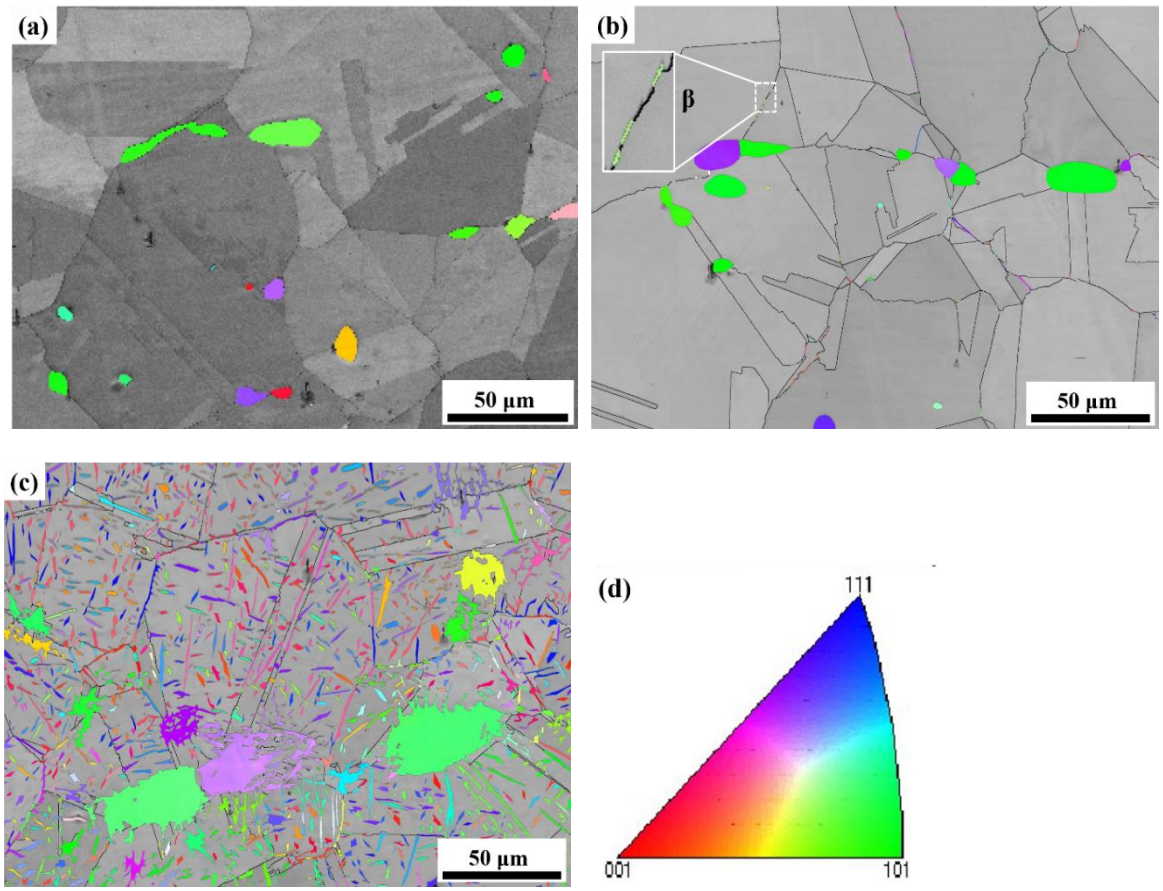


Fig. 4.1 SEM-EBSD micrographs of Cu-40%Zn alloy before and after ECP treatments where the α grains are in gray according to the EBSD band quality indices and the β phase in color according to its crystallographic orientation with respect to the X0 axis (X0 inverse pole figure (IPF) micrograph). (a) Annealed, (b) ECP treated with the current density j_{max}= 15.66 kA/ mm^2 and (c) ECP treated with j_{max}= 17.01 kA/ mm^2 (d) the X0 IPF color code. The electric current direction is in the X0 direction.

Fig. 4.1 shows the EBSD micrographs of the annealed Cu-40%Zn alloy before and after the ECP treatments, where the α grains are in gray represented with the EBSD band quality index contrast and the β ones are in color according to their crystallographic orientations. It is seen from **Fig. 4.1 (a)** that the annealed microstructure is mainly composed of α phase with a slight amount of irregularly shaped β phase that is formed during the solidification process. After the ECP treatment at low current density (15.66 kA/ mm^2) (**Fig. 4.1 (b)**), fine β precipitates started to precipitate along the α grain boundaries, as indicated in the insert of **Fig.**

4.1 (b). This means that the β to α transformation just started. When the sample was treated at high current density (17.01 kA/ mm^2), the transformation amount increased drastically not only along the α grain boundaries but also in the α grain interiors as shown in **Fig. 4.1 (c)**. The detailed information on the α and β microstructure evolution during the phase transformation process induced by ECP can be found in §3.3.2.2 (p45).

4.3.2 Crystal defect characteristics

4.3.2.1 Annealed

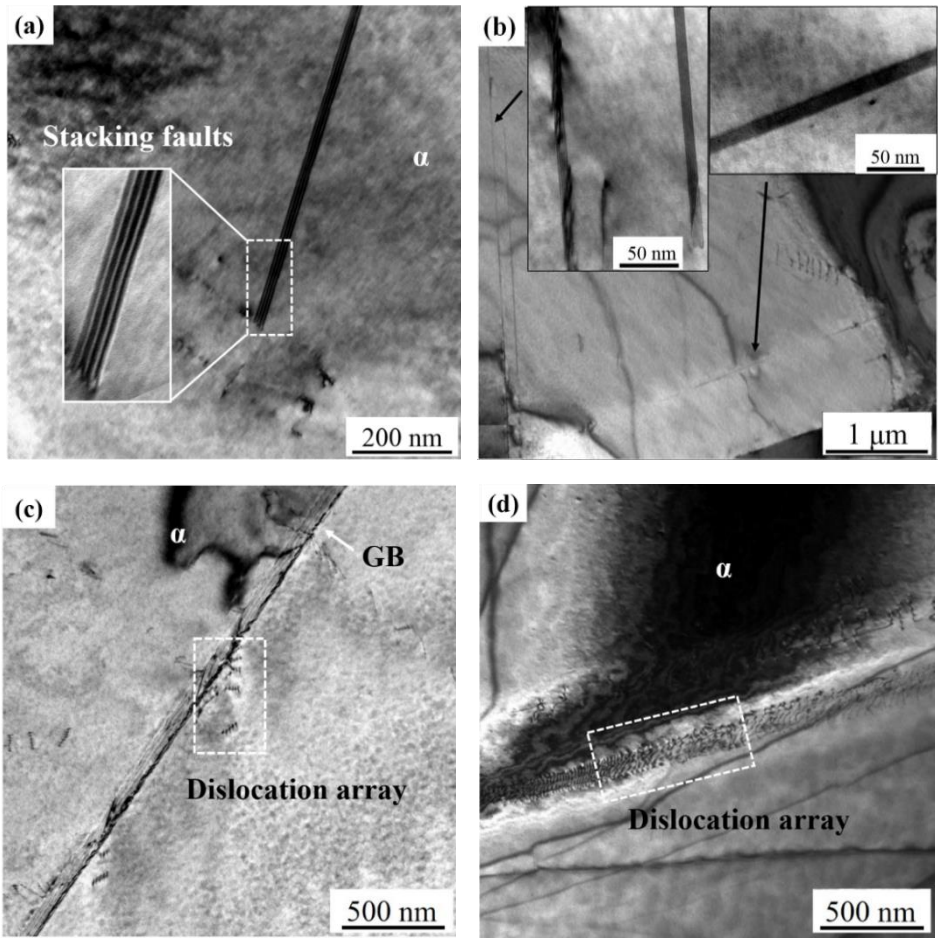


Fig. 4.2 TEM bright-field micrographs of the crystal defects of α grains in the annealed Cu-40%Zn samples. (a) and (b) Stacking faults, (c) and (d) dislocation arrays near the α grain boundaries.

In the annealed Cu-40%Zn alloy, there are small amount of stacking faults and dislocation arrays presented within the α matrix. The stacking faults with different default plane orientations located in the α grain interiors, as shown with typical examples in **Fig. 4.2 (a)** and **(b)**. The dislocation arrays located near the α grain boundaries are shown in **Fig. 4.2 (c)** and **(d)**.

Further analysis demonstrated that the stacking faults are of $\{111\}<11\bar{2}>_\alpha$ type and the dislocations are of $\{111\}<1\bar{1}0>_\alpha$ edge type . For this part of the work, the similar results can be found in §3.3.2.1 (p44).

4.3.2.2 ECP treatment at j_{max} = 15.66 kA/ mm^2

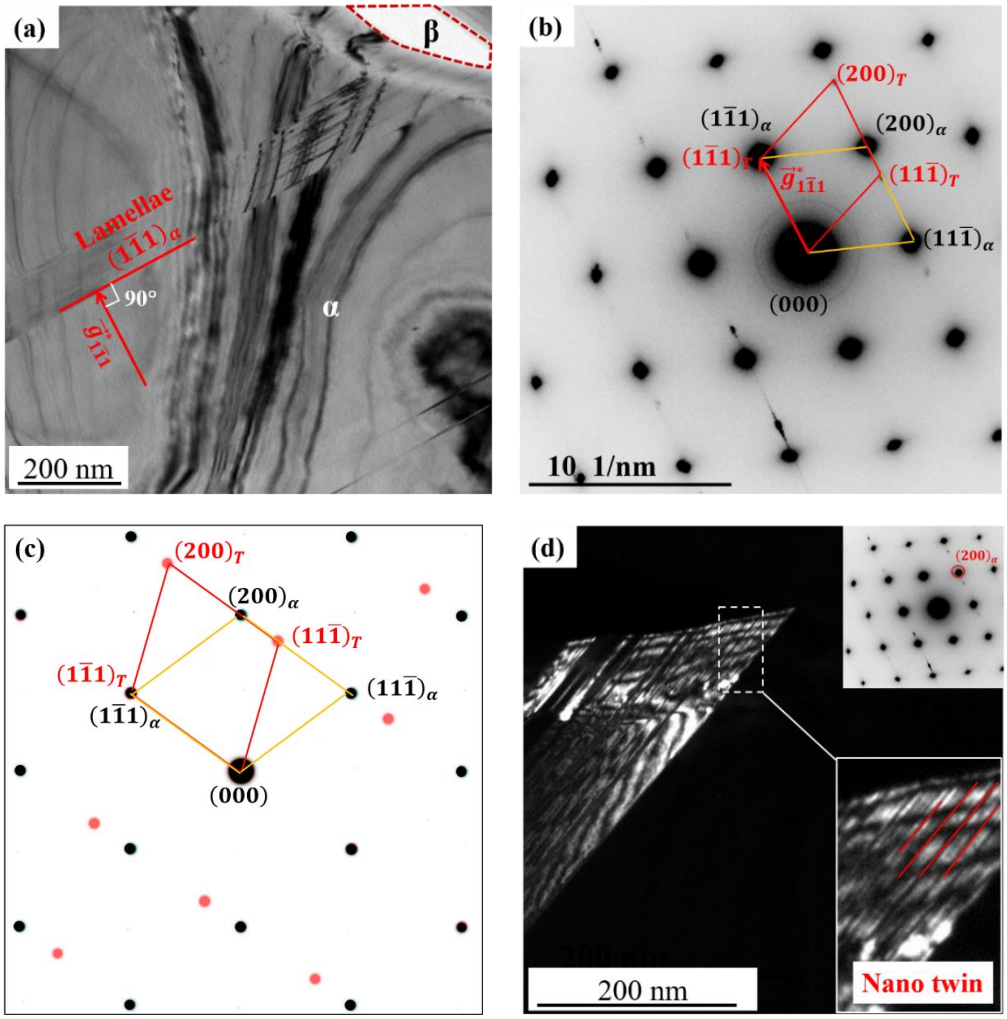


Fig. 4.3 (a) TEM bright-field micrographs of α grain in the ECPed Cu-40%Zn samples at j_{max}= 15.66 kA/ mm^2. (b) The corresponding $[011]_\alpha$ zone axis Selected Area Electron Diffraction (SAED) pattern of the α grain. (c) Simulated SAED patterns of the α grain with nano twins. (d) TEM dark-field micrographs obtained using the α $[200]_\alpha$ reflection as indicated in the insert of the figure. The red line represents the nano twins.

After the ECP treatment at j_{max}= 15.66 kA/ mm^2, large amount of parallel fine straight lamellae with thickness of about ten nanometers appeared within the α matrix, as revealed by the TEM diffraction contrast in **Fig. 4.3 (a)** (indicated with the red line). It should be mentioned that the curved fringes going from the lower part to the upper part in the figure are the so-called

equal inclination fringes induced by the curving of the thin foil. **Fig. 4.3 (b)** shows the corresponding $[011]_\alpha$ zone axis Selected Area Electron Diffraction (SAED) pattern of the α grain containing the fine lamellae. In the pattern, two sets of diffraction spots are visible. The one is from the high-intensity spots that are from the FCC α phase, as outlined with the yellow frame in **Fig. 4.3 (b)**. The other one is composed of low intensity spots with fine streaks, as outlined with the red frame in **Fig. 4.3 (b)**. These low-intensity diffraction spots correspond to the reflections also from the same FCC structure, but having specific orientation relationship with the α phase. The two patterns share the $(1\bar{1}1)_\alpha$ spot and the two patterns are symmetrical with respect to this spot. This indicates that the crystals giving the two set of diffraction patterns are twin related with the $(1\bar{1}1)_\alpha$ plane as the twinning plane. Further crystallographic analysis confirmed that the twins are of the $\{111\}\langle 11\bar{2}\rangle_\alpha$ type, as those find in the annealed sample (§3.3.2.1). Such twins are typical for the FCC crystals. The simulated SAED patterns of the twin and the α matrix are shown in **Fig. 4.3 (c)**. The good accordance confirm that the fine lamellae are the $\{111\}\langle 11\bar{2}\rangle$ twins to the α matrix. **Fig. 4.3 (d)** shows the dark-field image using the $[200]_\alpha$ reflection from the α matrix as outlined with the red circle in the insert of the figure. In the dark field image, the α matrix is illuminated, whereas the twinned lamellae remained dark, as indicated with the red lines in the magnified image inserted in **Fig. 4.3 (d)**. It can also be seen that the interfaces of the fine lamellae (**Fig. 4.3 (a)**) are perpendicular to the reciprocal vector $\vec{g}^*_{1\bar{1}1}$, as indicated in the bright field image and the SAED diffraction pattern, i.e., parallel to the $(1\bar{1}1)_\alpha$ planes of the α matrix. This suggests that the lamellar twins are interfaced with the α matrix with their twinning plane (the $(1\bar{1}1)_\alpha$ planes).

In addition, the fine lamellae structures were also observed with different lamellar orientations in the α grain in the ECPed Cu-40%Zn sample at j_{max}= 15.66 kA/ mm^2, as shown with one example in **Fig. 4.4 (a)**. Here the two differently oriented lamellae are denoted L1 (represented with the red line in **Fig. 4.4 (a)**) and L2 (represented with the yellow line in **Fig. 4.4 (a)**). **Fig. 4.4 (b)** shows the $[011]_\alpha$ zone axis SAED pattern of the α grain containing the two differently oriented lamellae (L1 and L2). The high-intensity spots that are from the FCC α matrix, as outlined with the yellow frame, are well visible. The interfaces of the two types of lamellae (L1 and L2) in **Fig. 4.4 (a)** are just perpendicular to the respective reciprocal vectors

$\vec{g}^*_{1\bar{1}1}$ and $\vec{g}^*_{11\bar{1}}$, as shown with the red and the yellow arrow in **Fig. 4.4 (b)**, inferring that the two kinds of lamellae might be two variants of the {111}<11$\bar{2}$>$_\alpha$ twins. However, in the SEAD pattern in **Fig. 4.4 (b)** only one set of low intensity spots, as outlined with the red frames, can be seen. According to the similar analysis described above, these weak spots can be identified to be the reflections from L1. For L2, as outlined with the yellow line in **Fig. 4.4 (a)**, there are no visible diffraction spots can be found in the SEAD pattern. This suggests that these lamellae are not yet twins to the α matrix. Although no visible spots can be found in the SAED pattern, streaks in the $(11\bar{1})_\alpha$ reciprocal direction can be clearly seen as indicated with the yellow arrow in **Fig. 4.4 (b)**. This suggests that the $(11\bar{1})_\alpha$ planes contain planar defects (detailed analysis on diffraction streaking will be given in the next chapter). These planar defects should be the

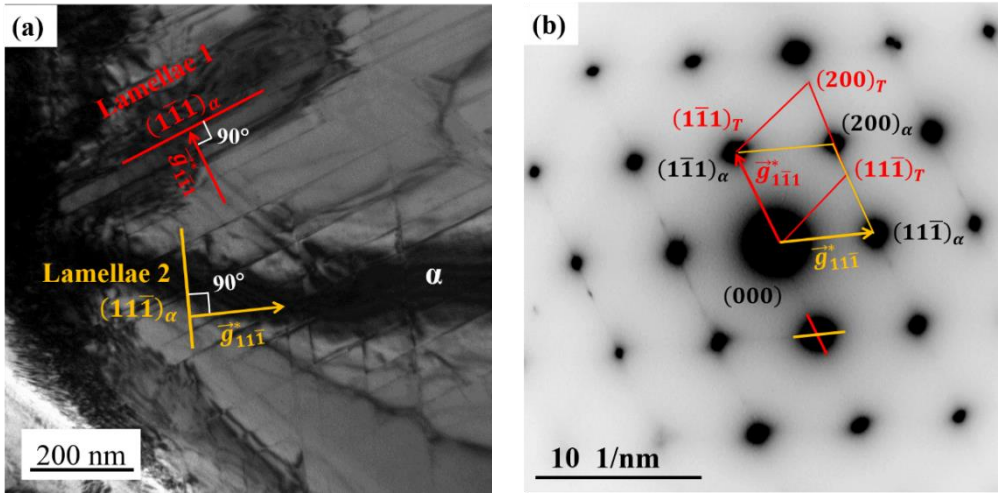


Fig. 4.4 (a) TEM bright-field micrographs of α grain in the ECPed Cu-40%Zn samples at j_{max}= 15.66 kA/ mm^2. (b) The corresponding [011]$_\alpha$ zone axis SAED pattern of the α grain.

stacking faults on the $(11\bar{1})_\alpha$ planes. As the interfaces of L2 are just perpendicular to the reciprocal vector $\vec{g}^*_{11\bar{1}}$, *i.e.*, parallel to the $(11\bar{1})_\alpha$ planes, these lamellae should be the stacking faults on the $(11\bar{1})_\alpha$ planes. As we know that for FCC crystals the planar defects are created by the Shockley partial dislocations when they glide on the {111} planes. If the Shockley partial dislocations glide only on individual {111} planes, they will not create detectable new orientations for the faulted planes. However, if they glide on many consecutive {111} planes (at least more than 3 planes), the part experienced the glide will demonstrate a new orientation. The reoriented part will be the {111}<11$\bar{2}$> twins with respect to the un-affected part of the crystal. Thus these results demonstrate that under the relative low current density (j_{max}= 15.66

kA/ mm^2) with only very minor formation of grain boundary β precipitates (as shown in **Fig. 4.1 (b)**), stacking faults and then nano twins were formed intensively in the α grain interiors.

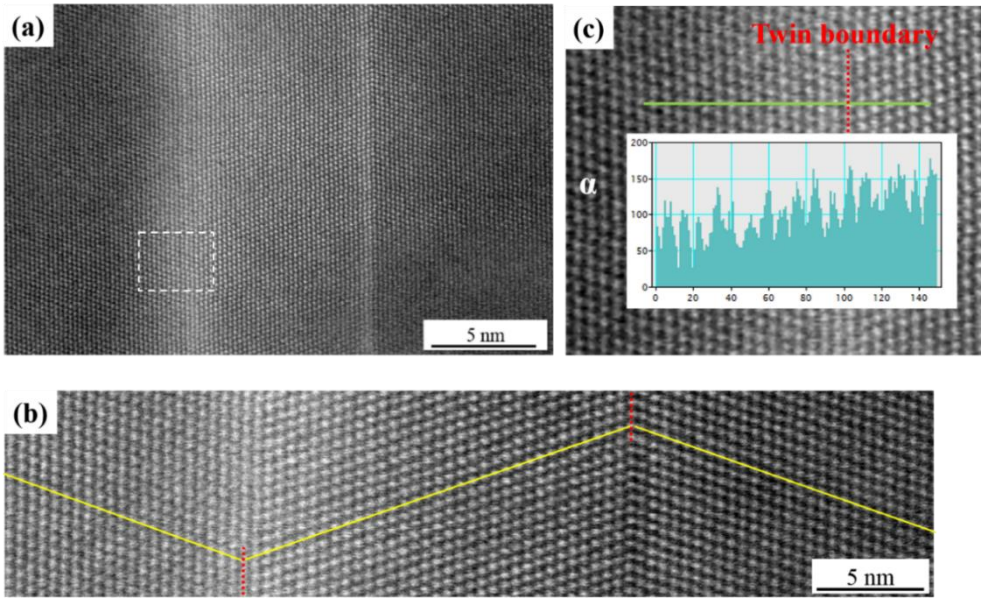


Fig. 4.5 (a) STEM-HAADF micrograph of the nano twin in the α matrix viewed in the $[011]_\alpha$ direction in the Cu-40%Zn alloy induced by the ECP at j_{max}= 15.66 kA/ mm^2. (b) Enlarged STEM-HAADF image. The twin boundaries are outlined with red dotted lines. Equivalent layers are marked with yellow lines. (c) Intensity profiles of the outlined (in green) atom columns of the figure (a) marked with white rectangle.

To further analyze the solute (Zn) repartition in the nano twin regions, the atomic number related contrast of these regions were examined by STEM-HAADF. **Fig. 4.5 (a)** shows an example of the atomic-resolution STEM-HAADF micrographs of the nano twins viewed in the $[011]_\alpha$ direction of the ECPed (j_{max} = 15.66 kA/ mm^2) Cu-40%Zn sample. It is seen that the twinned part having a thickness of about 10 nm is well separated by straight interfaces. As further magnified in **Fig. 4.5 (b)**, where the twin boundaries are outlined with the red dotted lines and the same Miller indexed planes in the twinned parts are marked with the yellow lines. Further examination showed that the twin interfaces coincide with the twinning plane $\{111\}_\alpha$. Moreover, it can be seen that the contrasts of the atoms at the twin boundaries are not constant. As is known, in the STEM-HAADF micrographs, the contrast is related to the atomic number Z. The atom column intensity is basically proportional to the square of the corresponding atomic number, as shown by Equation (4-1):

$$I_s = \left(\frac{m}{m_0}\right) * \frac{\boldsymbol{Z^2} * \lambda^4}{4\pi * \sqrt[3]{{\alpha_0}^2}} * \left(\frac{1}{{\theta_1}^2 + {\theta_0}^2} - \frac{1}{{\theta_2}^2 + {\theta_0}^2}\right) * N * t * I \qquad (4\text{-}1)$$

where I_s is the scattering intensity, m is the mass of the electron at accelerated state, m_0 is the mass of the electron at static state, Z is the atomic number, λ is electron wavelength, α_0 is the Bohr radius, θ is Persian characteristic scattering angle ($290° > \theta_0 > 50°$, $10° > \theta_1 > 10°$, $\theta_2 < 10°$), *N* is atomic number per unit volume, *t* is sample thickness and *I* is scattering intensity of a single atomic column. Accordingly, in the *Z* contrast image, the contrast of the heavier Zn atom should be higher than that of the lighter Cu atom. Thus the contrast of the lighter (Cu) atom columns should be differentiated from that of the heavier (Zn) atom columns. For the same observation at the same sample region, the above experimental parameters (m, m_0, λ, α_0, θ, *N, t, I)* are the same except for the atomic number (Z) of the atoms in the observed sample. So, the intensity ratio (or the relative contrast) can be used to analyze the solute repartition in the nano twin regions. According to Equation (4-1), the theoretical intensity ratio between the Zn atom and the Cu atom can be expressed as $(Z_{zn})^2/(Z_{cu})^2$ and the calculated result is shown in **Table 4.1**.

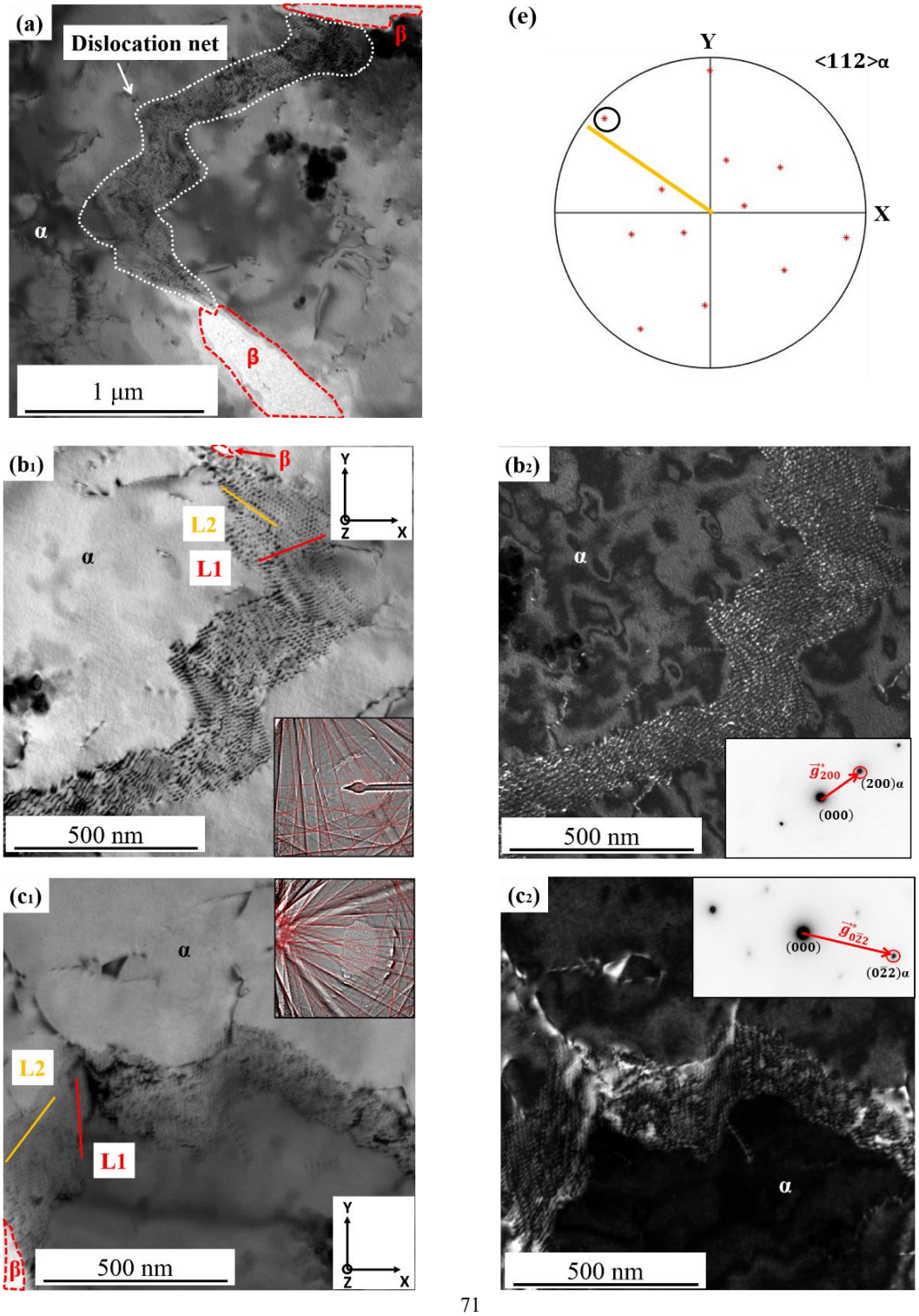
Table 4.1 The intensity ratio value between Zn atom and Cu atom.

	Theoretical value	Empirical value	Actual value
Intensity Ratio	1.07	1.06	1.19

However, in practice, the Persian characteristic scattering angles cannot reach the theoretical values. Thus, the intensity ratio is empirically expressed as $(Z_{zn})^{1.7}/(Z_{cu})^{1.7}$ and the obtained result is shown in the table. It is seen that the two ratios are very close. Then using the measured data from the intensity profiles of the outlined (in green) atom columns in **Fig. 4.5 (c)** (magnified area outlined with the white frame in **Fig. 4.5 (a)**), the actual intensity ratio between those of the atom columns near the twin boundary (indicated with the red line) and those of the matrix α phase (on the left part of the **Fig. 4.5 (c)**) were obtained. To obtained the statistical intensity value, 10 positions were used to calculate the average intensity value from about 160 atom columns. The obtained value is also shown in **Table 4.1**. In addition, one example intensity profile in **Fig. 4.5 (c)** indicated that the intensity gradually decreased from the right part (the twin grain boundary) to the left part of the α matrix. This suggests that the Zn

atoms are segregated near the $\{111\}_\alpha$ twin boundaries with a gradient distribution toward the matrix interior. This result evidences the segregation of the Zn atoms at the boundary regions of the twins induced by the ECP treatment with low current density. The reason of the Zn segregation will be further analyzed using the *ab-initio* calculations later.

4.3.2.3 ECP treatment at j_{max} = 17.01 kA/ mm^2



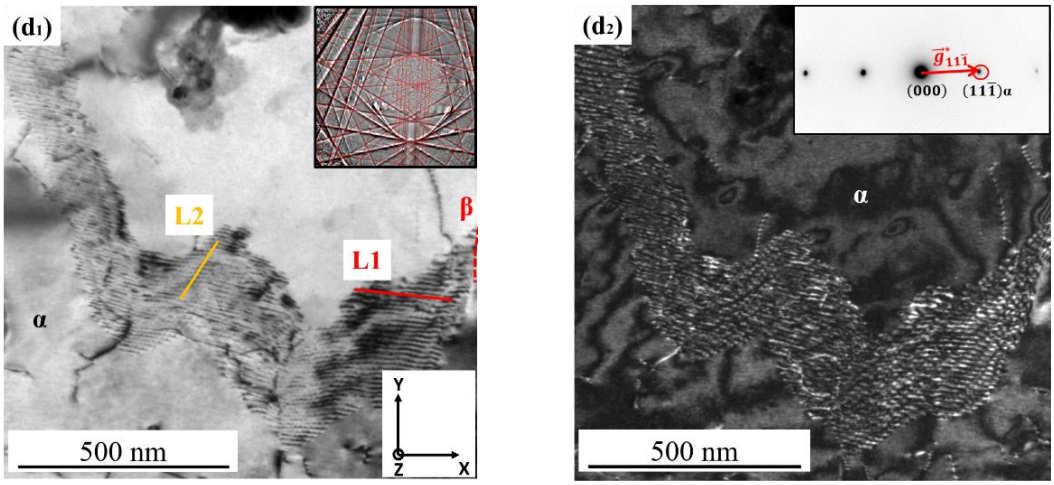


Fig. 4.6 (a) TEM bright field micrograph of the dislocation net in the α phase in the ECPed Cu-40%Zn alloys at j_{max}= 17.01 kA/ mm^2. (b) - (d) The magnified bright-field and dark field micrographs of the dislocation net with the measured and indexed (in red) Kikuchi line pattern of α phase using the *FCC* crystal structure parameters and the SAED pattern indicating the reflected beam for the dark field imaging inserted. (e) The corresponding <112>$_\alpha$ direction pole figure. The solid color lines indicate the dislocation lines constituting the dislocation net. The bright field and dark field images shown in (a) – (c) were acquired for the same dislocation net but at different sample positions. The sample position change was realized through double tilting the sample holder by rotating the holder around the X-axis (denoted λ) and by rotating the holder around the Z-axis (denoted γ).

When the current density reached j_{max}= 17.01 kA/ mm^2, large amount of β precipitates were formed in the α grains, as shown in **Fig. 4.1 (c)**. The intragranular β precipitates are related with the α matrix with the N-W OR, as detailed in § 3.3.4 (P48). Interestingly, the large amount of intragranular nano twins formed at j_{max}= 15.66 kA/ mm^2 disappeared in the ECPed sample at j_{max}= 17.01 kA/ mm^2.

Further TEM examination revealed that near the β precipitates, a large amount of dislocation nets were formed, as shown in **Fig. 4.6 (a)**, where the β phase were marked with the red dotted lines and the dislocation net with the white dotted line. It should be mentioned that as the resistance of the β phase to the electropolishing was much lower than that of the α phase, the β precipitates seldom sustained the electropolishing process. So the holes shown in **Fig. 4.6 (a)** were from the β precipitates. **Fig. 4.6 (b_1), (c_1)** and **(d_1)** show the bright-field micrographs of the dislocation network at three two beam sample positions allowing only the $(200)_\alpha$, the $(0\bar{2}2)_\alpha$ or the $(11\bar{1})_\alpha$ at Bragg condition. The sample position change was realized using the double tilts of the sample holder by rotating the holder around the X-axis (denoted λ) and by

rotating the holder around the Z-axis (denoted γ). The detailed tilt angles are shown in **Table 4.2**. It is seen that the dislocation net in **Fig. 4.6** is composed of two differently oriented dislocation lines that are denoted L1 (represented with the red line in **Fig. 4.6**) and L2 (represented with the yellow line) in the figures. The two-beam conditions were further achieved to examine the invisibility of the two dislocation lines to identify the dislocation type, the Burgers vector and the line vector.

Table 4.2 The detailed sample tilts of Fig. 4. 6 (b), (c) and (d).

	λ (°)	γ (°)
Fig. 4.6 (b)	2.49	130
Fig. 4.6 (c)	11.62	0
Fig. 4.6 (d)	13.95	220

Table 4.3 Verification of $\boldsymbol{g}\cdot\mathbf{b}$ for the invisibility of dislocation lines under different reflections.

$\boldsymbol{b}$ \ $\boldsymbol{g}$	$\vec{g}^{*}_{200}$	$\vec{g}^{*}_{0\bar{2}2}$	$\vec{g}^{*}_{11\bar{1}}$
[111]	$\neq$ **0**	$=$ **0**	$\neq$ **0**
[$\bar{1}$11]	$\neq$ **0**	$=$ **0**	$\neq$ **0**
[1$\bar{1}$1]	$\neq$ 0	$\neq$ 0	$\neq$ 0
[11$\bar{1}$]	$\neq$ 0	$\neq$ 0	$\neq$ 0
[110]	$\neq$ 0	$\neq$ 0	$\neq$ 0
[101]	$\neq$ 0	$\neq$ 0	$=$ 0
[011]	$=$ 0	$=$ 0	$=$ 0
[$\bar{1}$10]	$\neq$ 0	$\neq$ 0	$=$ 0
[10$\bar{1}$]	$\neq$ 0	$\neq$ 0	$\neq$ 0
[01$\bar{1}$]	$=$ **0**	$\neq$ **0**	$\neq$ **0**
[112]	$\neq$ 0	$\neq$ 0	$=$ 0
[121]	$\neq$ 0	$\neq$ 0	$\neq$ 0
[211]	$\neq$ 0	$=$ 0	$\neq$ 0
[$\bar{1}$12]	$\neq$ 0	$\neq$ 0	$\neq$ 0
[$\bar{1}$21]	$\neq$ 0	$\neq$ 0	$=$ 0
[$\bar{2}$11]	$\neq$ 0	$=$ 0	$\neq$ 0
[1$\bar{1}$2]	$\neq$ 0	$\neq$ 0	$\neq$ 0
[12$\bar{1}$]	$\neq$ 0	$\neq$ 0	$\neq$ 0
[2$\bar{1}$1]	$\neq$ 0	$\neq$ 0	$=$ 0
[11$\bar{2}$]	$\neq$ 0	$\neq$ 0	$\neq$ 0
[12$\bar{1}$]	$\neq$ 0	$\neq$ 0	$\neq$ 0
[21$\bar{1}$]	$\neq$ 0	$\neq$ 0	$\neq$ 0

The corresponding dark-field micrographs of the dislocation network were obtained, as

shown in **Fig. 4.6 (b_2)**, **(c_2)** and **(d_2)**, using the respectivethe $(200)_\alpha$, $(0\bar{2}2)_\alpha$ and $(11\bar{1})_\alpha$ reflections of the α matrix as circled in the inserts in the figures. It is known that if the dislocation Burgers vector $\boldsymbol{b}$ is lying on the operated reflecting plane $\boldsymbol{g}$ for the dark field imaging, the corresponding dislocation lines disappear. This can be explained by $\boldsymbol{g}\cdot\boldsymbol{b} = 0$, the so-called invisibility criterion. So the characteristic extinction of the dislocation lines allows finding the dislocation type and dislocation Burgers vector $\boldsymbol{b}$. For the dislocation L1, it is present in **Fig. 4.6 (b_2)** and **(d_2)** but not in **Fig. 4.6 (c_2)**, whereas for the dislocation L2, it is present in **Fig. 4.6 (c_2)** and **(d_2)** but not in **Fig. 4.6 (b_2)**. This evidences that the dislocation lines exhibit characteristic extinction. To find out the possible Burgers vectors of these dislocations, the dislocation Burgers vectors published in the literature (<111>, <110>, <112>) in FCC crystals are verified with the product of the $\boldsymbol{g}\cdot\boldsymbol{b}$. The results are given in **Table 4.3**. It is seen that the Burgers vector $\boldsymbol{b}_{L_1}$ of dislocation L1 is parallel to $[011]_\alpha$, and the Burgers vector $\boldsymbol{b}_{L_2}$ of dislocation L2 to $[01\bar{1}]_\alpha$, as highlighted in bold in **Table 4.3**.

To determine the types of the dislocations, the trace analysis method is used to determine the dislocation line vector. The inserts of **Fig. 4.6 (b_1)**, **(c_1)** and **(d_1)** show the Kikuchi line patterns acquired in the corresponding α matrix. By indexing the pattern using the *FCC* crystal structure parameters with the home-made software, EP, the orientation of the α matrix was determined. The calculated Kikuchi line patterns, as shown with the red line pattern in the insert of **Fig. 4.6 (b_1)**, **(c_1)** and **(d_1)** agree well with the experimentally acquired Kikuchi patterns. With the determined orientation of the α matrix, the orientation of the possible dislocation line projections for the two kinds of dislocations were calculated and compared with the orientations of the dislocation lines in the network, as an example shown in **Fig. 4.6 (e)**. Results showed that for dislocation L 2 the dislocation line is parallel to $<211>_\alpha$, as illustrated with the $<112>_\alpha$ direction pole figures in **Fig. 4.6 (e)**. That suggests that the perfect dislocation is edge type with the Burgers vector $\boldsymbol{b}$ // $[01\bar{1}]_\alpha$ and the dislocation line // $<211>_\alpha$.

This result evidence that the dislocation net is composed of two kinds of dislocations, the one being the normal $\boldsymbol{b}$ // $<110>_\alpha$ perfect dislocation and the other being the Frank dislocation $\boldsymbol{b}$ // $<111>_\alpha$. The former is movable and the latter is immobile, as the $\boldsymbol{b}$ // $<111>_\alpha$ is perpendicular

to the slip plane $\{111\}_{\alpha}$. Thus the dislocation net appeared at the tips of the intragranular β precipitates are also immobile due to the existence of the Frank dislocation. This explains why the dislocation nets still stay even though the β precipitates were already polished out, *i.e*. the local strain and stress were largely released.

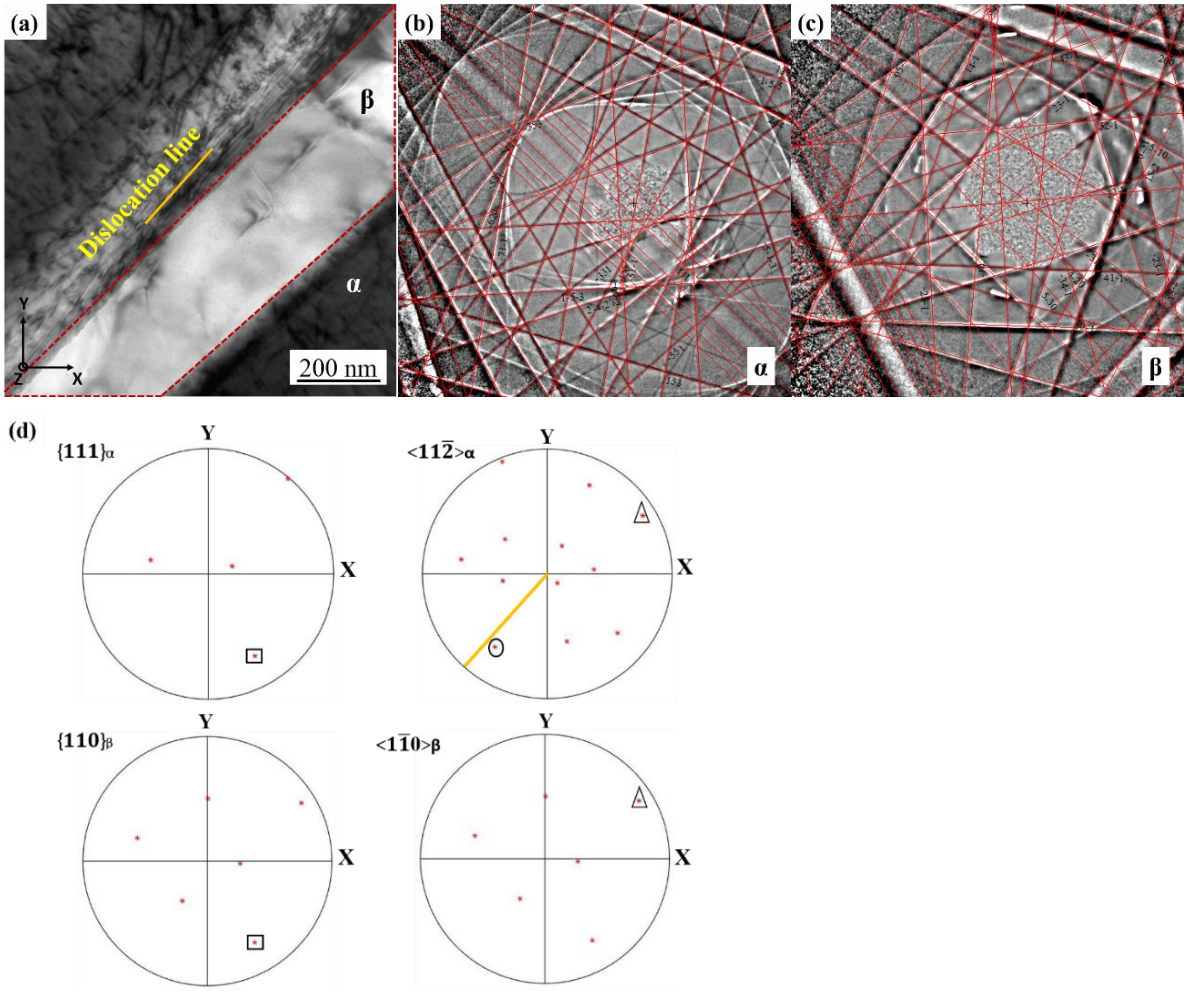


Fig. 4.7 (a) TEM bright field micrographs of dislocation arrays parallel to the α/β interface in Cu-40%Zn samples ECPed at j_{max}= 17.01 kA/ mm^2. (b) Measured Kikuchi line pattern of α phase with the calculated pattern (in red) using the *FCC* crystal structure parameters. (c) Measured Kikuchi line pattern of β phase with the calculated pattern (in red) using the *BCC* crystal structure parameters. (d) The corresponding N-W OR direction and plane pole figures of the parent α and the β precipitate. The poles of the corresponding OR planes and OR directions are enclosed in the respective rectangles and triangles. The orange line in the $<11\bar{2}>_{\alpha}$ pole figure in (d) indicated the orientation of the dislocation lines in (a) and the pole corresponding to the dislocation line vector is enclosed in the circle.

Further examination near the broad face regions of the intragranular β precipitates revealed the existence of a large amount of straight and parallel dislocation arrays piling up in front of

the α/ β interface, as shown in **Fig. 4.7 (a)**. The image was acquired with the incident beam close to the $[111]_\alpha$ direction. The β precipitate is marked with the red dotted lines, and the dislocation line is outlined with the orange line. **Fig. 4.7 (b)** and **(c)** show the measured Kikuchi line pattern of the α phase with the calculated pattern (in red) using the *FCC* crystal structure parameters and the measured Kikuchi line pattern of the β precipitate with the calculated pattern (in red) using the *BCC* crystal structure parameters, respectively. Using the EP sofeware, the orientations (expressed in the Euler angles) of the α matrix and of the β precipitate were determined. Further crystallographic analysis showed that the α matrix and the β precipitate obey the N-W OR, as illustrated with the OR plane and direction pole figures in **Fig. 4.7 (d)**, with some angular deviations (0.7764° deviated from the ideal N-W OR). According to the detail description on the β precipitate morphology in §3.3.5 (p52), the β precipitate in **Fig. 4.7 (a)** should correspond to the Type A β_{GI} precipitates which are in long bar shape and the N-W OR direction ($<112>_\alpha$) is nearly parallel to the two broad faces of the precipitates. Analysis using the trace match method revealed that the dislocation lines are of $\{111\}_\alpha <1\bar{1}0>_\alpha$ edge type dislocation (the Burgers vector $\boldsymbol{b}$ // $[1\bar{1}0]_\alpha$ and the dislocation lines // $<11\bar{2}>_\alpha$), as shown in the $<11\bar{2}>_\alpha$ direction pole figure of the α phase in the **Fig. 4.7 (d)**. The above results indicated that the formation of these dislocations should be related to the formation of the β_{GI} precipitates.

4.4 Discussion

From the above observations on the evolution of the crystal defects during the α to β phase transformation process induced by the ECP, one can find that the nano twins formed in the α grain interiors should be considered as an important microstructural constituent. Detailed strain character analysis revealed that the formation of the nano twins possesses some common strain feature with the formation of the β precipitates. By examining the atomic correspondence of the twinned crystal with that of the matrix crystal, the lattice strain to form the nano twins were constructed and represented with the deformation gradient tensor expressed in the corresponding slip reference systems (*i-j-k*). The same analysis was also conducted on the formation of the β precipitates under the N-W OR and the lattice strains also represented with the deformation gradient tensor expressed in the same reference system. For the transformation

lattice deformation tensor, the detail information can be found in § 3.4.3 (p57). For the *i-j-k* reference system, *j* is set parallel to twinning shear direction (also the OR direction), *k* to the direction normal to the twinning plane (also the OR plane) and *i* to the vector cross product of *j* and *k*. The tensors obtained using the measured lattice constants of the two phases in the sample treated at 15.66 kA/ mm^2 (**Table 3.1**) are given in **Table 4.4**. The detail description on the measured lattice constants of the two phases in the sample treated at different current densities could be found in §3.3.2 (p43).

Table. 4.4 Deformation gradient tensor of the structure deformation to from the nano twins and β phase in the sample after ECP treatment expressed in the slip system reference system (also the N-W OR reference system).

OR	Relation	Deformation Gradient Tensor
Nano twin	$\{111\}_\alpha<11\bar{2}>_\alpha$	$i // [1\bar{1}0]$ $j // [11\bar{2}]$ $k // [111]$ $M_{twin} = \begin{bmatrix} 1 & 0 & 0 \\ 0 & 1 & 0.7070 \\ 0 & 0 & 1 \end{bmatrix}$
β precipitates	$\{111\}_\alpha // \{110\}_\beta$ $<11\bar{2}>_\alpha // <1\bar{1}0>_\beta$	$i // [1\bar{1}0]$ $j // [11\bar{2}]$ $k // [111]$ $M_\beta = \begin{bmatrix} 1.1109 & 0 & 0 \\ 0 & 0.9137 & 0.3230 \\ 0 & 0 & 0.9691 \end{bmatrix}$

Compared with the deformation gradient tensors for the nano twins M_{twin} and the β precipitates M_β in **Table 4.4**, it is seen that the same shear component but with different shear magnitudes, a_{23}, on the $\{111\}_\alpha<11\bar{2}>_\alpha$ slip system is required during the two processes. As the formation of the nano twins need a quite large $\{111\}_\alpha<11\bar{2}>_\alpha$shear (0.707), the formation of the twin lamellas would result in a large lattice distortion and thus distortion energy. In a pure Cu lattice, this process should be difficult. This explains why the twin lamellas are very thin with thicknesses of only about ten nanometers as shown in **Fig. 4.3** and **Fig. 4.4**. Thus The existence of the Zn atoms in the Cu lattice could be useful to reduce the distortion energy or the stacking fault energy for the formation of the nano twins, as the formation of the twins can be regarded as the glide of $<11\bar{2}>_\alpha$ partial dislocations on the consecutive $\{111\}_\alpha$ planes. The stacking fault energy of the $\{111\}_\alpha$ without and with Zn atoms was simulated by the *Ab initio* calculations in cooperation with a professional staff of NEU and the results are shown in **Fig. 4.8 (a)** and the

corresponding atom maps of the stacking fault with different Zn concentrations on the $\{111\}_\alpha$ twinning plane are displayed in **Fig. 4.8 (b)**, where the Cu atoms are in red and the Zn atoms in yellow. It is seen from **Fig. 4.8 (a)** that the existence of the Zn atoms can effectively decrease the peak energy of the stacking fault that is represented as the energy barrier of the atom displacement during the glide of the partial dislocations on the $\{111\}_\alpha$ plane. This indicates that the Zn atoms enriched on the $\{111\}_\alpha$ shear plane will reduced the stacking fault energy and thus facilitate the formation of the twins. Thus, the stacking faults or the twins could preferentially form in the Zn rich regions to reduce the energy barrier. This is why in the STEM-HAADF images in **Fig. 4.5** the atoms on the twin boundaries display higher Z contrast, meaning that more Zn atoms are segregated on the twin boundaries.

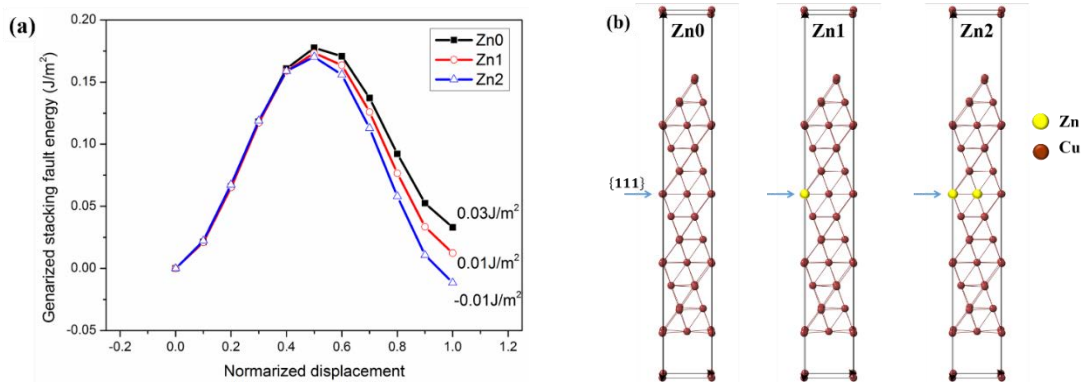


Fig. 4.8 (a) Atom normalized displacement dependence of stacking fault energy of the stacking fault with different Zn concentrations and (b) corresponding atom maps of the stacking fault with different concentration of Zn in. Cu is in red and Zn in yellow. The $\{111\}_\alpha$ shear plane of the stacking fault is indicated with arrows.

Table 4.5 The temperature of the Cu-40%Zn alloy under different ECP treatment.

Electric Current Density (kA/mm^2)	**Duration (μs)**	**T (°C)**
0	/	25
15.66	118	588
17.01	150	876

However, the appearance of the nano twins and the stacking faults in the α grain interiors instead of that of β_{GI} precipitates when the sample was treated at j_{max}=15.66 kA/mm^2 may be due to the temperature effect. As shown in **Table 4.5**, the estimated temperature of the sample when treated at j_{max}=15.66 kA/mm^2 is about 588.37°C that may not be sufficiently high to

induce the β to α transformation everywhere in the treated sample. The joule heating should be more localized in the places where the resistivity is higher, such as the grain boundary regions and the segregation regions of Zn (the resistivity of Zn is higher than that of Cu) at relatively low current density. Clearly, grain boundary regions should possess higher resistivity than Zn concentrated regions and thus have higher temperature. As a result, phase transformation started to happen at certain boundary regions. For the grain interiors, as the sample was annealed and possessed higher crystalline perfection, the temperature rise was not sufficient for phase transformation, but local temperature rise at high resistivity regions exists and cannot be homogenized by heat transfer, as the treatment time was very short. Therefore, local mechanical constraints due to temperature variation existed and induced local deformation of the treated sample. Thus, nano twins or stacking faults were formed at regions with local segregation of Zn. When the current density was increased to j_{max}=17.01 kA/mm^2, the equivalent temperature of the treated sample was drastically increased to 876.95°C, as shown in **Table 4.5** (about 200°C higher than the phase transformation temperature 660°C). Thus, phase transformation happened, taking the place of deformation (twinning or partial dislocation glide). As a result, a large amount of β precipitates were formed both along α grain boundaries and in α grain interiors.

After the rapid α to β phase transformation in the sample treated with j_{max}=17.01 kA/mm^2, dislocation nets composed of the perfect mobile dislocations and the Frank type dislocations formed at the tip of the β precipitates and the {111}<1$\bar{1}$0> typed edge dislocations formed at the broad faces of the β precipitates should be related to two factors. The one is the volume misfit between the α and the β phase and the other is the ultra-rapid formation and growth of the β precipitates in the α phase.

To further reveal the formation mechanisms of the dislocations and the dislocation network, the lattice deformation to realize the α to β transformation was analyzed and expressed with the deformation gradient tensor, as displayed in **Table 4.4**. It should be noted that any none zero value of the normal strains and the shear strains represent the change of the dimensions of the α phase to form the β precipitates during the transformation process. For the β_{GI} precipitates of Type A that appeared in majority (§3.3.5), they are encased in two pairs of parallel planes, $\{211\}_\alpha$ and $\{311\}_\alpha$ of the α phase as the prismatic planes. **Fig. 4.9** illustrated

the lattice deformation and volume misfit between the α and the Type A β_{GI} precipitates under different view directions ($[111]_\alpha$ direction, $[11\bar{2}]_\alpha$ direction and $[1\bar{1}0]_\alpha$ direction) where the red frames outline the α phase that will transformation to the β phase; while the green frames the β precipitate in 2D forms. As seen from the deformation gradient tensor M_β, the transformation requires an elongation of the α phase along the $[1\bar{1}0]_\alpha$ direction to form the β precipitate as illustrated in **Fig. 4.9 (a_1)** (projected along the $[111]_\alpha$ direction). That means the α phase should be expanded along the $[1\bar{1}0]_\alpha$. Thus, the $\{111\}<1\bar{1}0>_\alpha$ edge type dislocation should be most likely formed at the broad faces of the β precipitate as seen in **Fig. 4.9 (a_2)**, where the precipitate is approximately represented with an ellipsoid. Such dislocations correspond to the observed dislocation arrays in **Fig. 4.7 (a)**. In addition, the α phase was required be contracted along the $[111]_\alpha$ direction to form the β precipitate as seen in **Table 4.4** and illustrated in **Fig. 4.9 (b_1)**. As the $[11\bar{2}]_\alpha$ direction is the growth direction of the Type A β_{GI} precipitates (~80° to the $\{121\}_\alpha$ and ~90° to the $\{3\bar{1}1\}_\alpha$), the precipitate projected along the $[11\bar{2}]_\alpha$ is roughed into a round form, as displayed in **Fig. 4.9 (b_2)**. It is clear that the Frank dislocation could be formed due to the shrinkage of the α phase along $[111]_\alpha$ direction for the structure transformation. However, along the $[11\bar{2}]_\alpha$ direction, the transformation of the α phase requires two strain components, the one being a contraction along the $[11\bar{2}]_\alpha$ direction while a $\{111\}<11\bar{2}>_\alpha$ shear also can be required as shown in **Table 4.4**. As the accumulation and the other one being a shear on $\{111\}<11\bar{2}>_\alpha$ shear system. The two strains evoke opposite dimension change in the $[11\bar{2}]_\alpha$ direction. The normal strain or the contraction reduces the dimension of the precipitate and the shear increases the dimension in this direction, as illustrated in **Fig. 4.9 (c_1)**. Thus, the dimension change in this direction is roughly canceled out. Thus, no systematic dislocation arrays form in the tip front of the precipitate. This also explains why the precipitate can grow along this direction.

According to the above decomposed analyses, it is obvious that the dislocation nets can be formed on along the edges of the broad faces of the β precipitate, as illustrated in **Fig. 4.10**. Such dislocation nets are composed of $\{111\}<1\bar{1}0>_\alpha$ edge type dislocations with dislocation lines parallel to $<11\bar{2}>_\alpha$ and the Frank dislocations and correspond to the observed dislocation nets in the **Fig. 4.6**. Thus, the dislocations were induced to accommodate the volume misfit between the β precipitates and the original α volume.

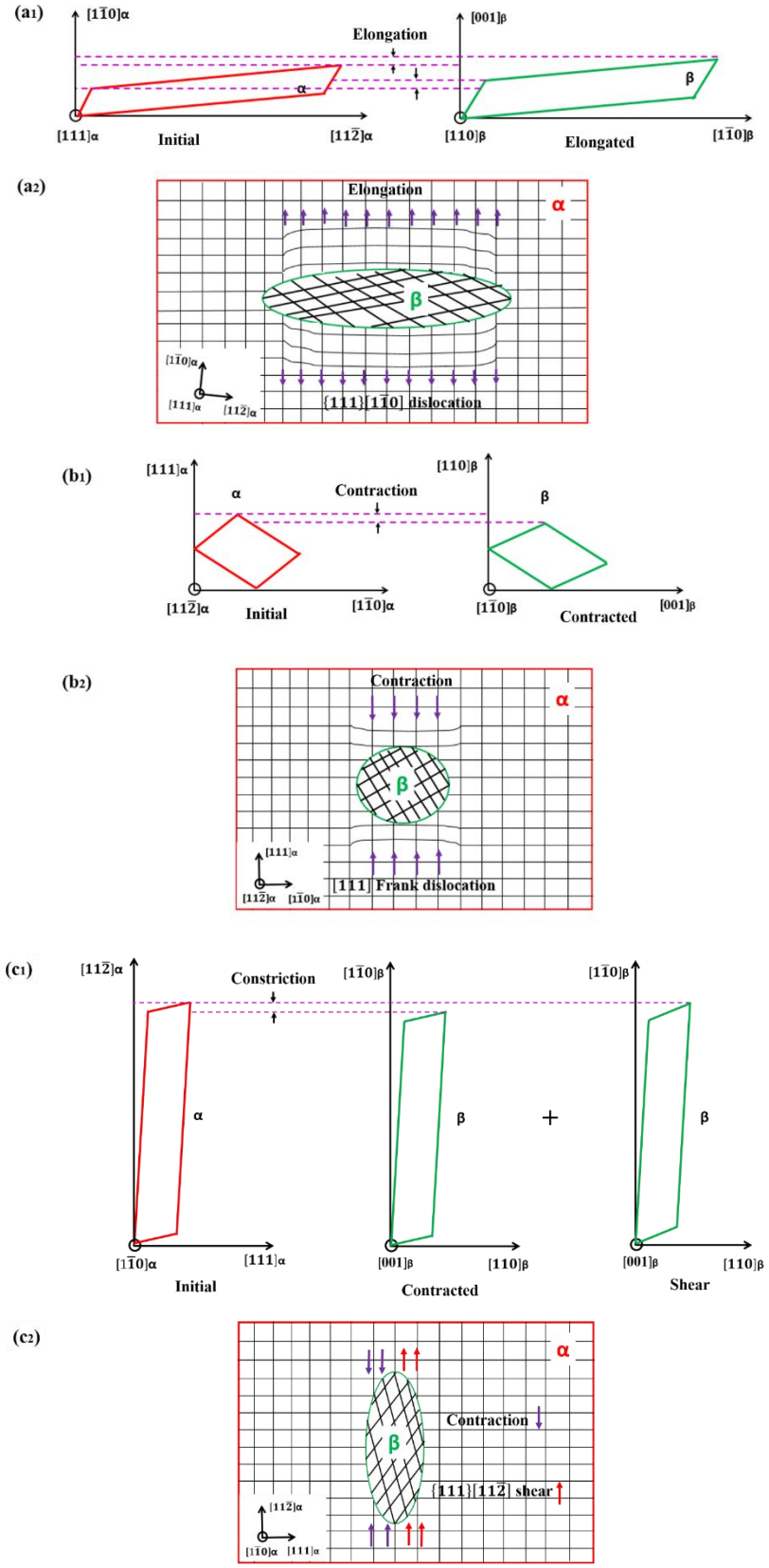


Fig. 4.9 2D projections and illustrations of the β precipitate in the α matrix viewed along the directions of the basis vectors of the N-W OR reference system. Along (a) $[111]_\alpha$ direction, (b) $[11\bar{2}]_\alpha$ direction and (c) $[1\bar{1}0]_\alpha$ direction. The red frame represents the α volume that will transform to the β phase; while the green frame the β precipitate.

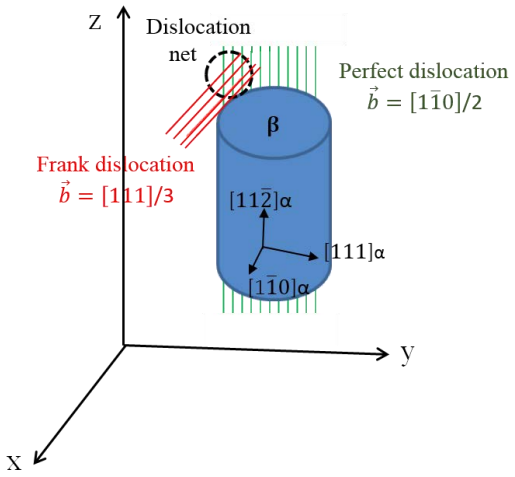


Fig. 4.10 Illustration of dislocation net.

4.5 Summary

In the present chapter, the crystallographic features of defects in the α phase during the α to β phase transformation induced by electric current pulse (ECP) with different densities in an annealed Cu–40%Zn alloy was thoroughly investigated.

For the ECPed sample at j_{max}=15.66 kA/ mm^2, large amount of $\{111\}<11\bar{2}>_\alpha$ stacking faults and nano twins were formed in the α matrix. Experimental and simulation results showed that the Zn atoms enriched on the $\{111\}_\alpha$ shear plane will reduced the stacking fault energy and thus facilitate the formation of the stacking faults and then the twins.

For the ECPed sample at j_{max}=17.01 kA/ mm^2, dislocation nets formed after the α to β phase transformation. Such dislocation nets are composed of perfect $\{111\}<1\bar{1}0>_\alpha$ edge typed dislocations and Frank typed dislocations. The volume misfit between the α and the β phase analyzed with transformation deformation demonstrated that the transformation from α to β required an expansion along the $[1\bar{1}0]_\alpha$ direction and a contraction along the $[111]_\alpha$ direction. The former resulted in the formation of the $\{111\}<1\bar{1}0>_\alpha$ edge typed dislocation arrays in front of the $\{3\bar{1}1\}_\alpha$ broad faces and the latter induced the formation of the Frank typed dislocations in front of the $\{121\}_\alpha$ broad face. Thus, dislocation nets formed along the edges of the broad faces of the β precipitate when the two kinds of dislocation arrays met in these regions.

With the present work, the correlation between the types of crystal defects (stacking faults, nano twins and dislocation nets) and the rapid α to β phase transformation were fully revealed.

Chapter 5 Sub-structure of β precipitates formed by ECP treatment in Cu-40％Zn alloy

5.1 Introduction

The microstructure, phase transformation ORs and the crystallographic features of the α to β heating phase transformation and the crystal defects in α phase related to the formation of the β precipitates induced by the ECP treatments were investigated. In this chapter a thorough crystallographic study on the nano-scaled hexagonal structures in the ECP induced β phase is conducted. The existence of two hexagonal structures is firstly revealed by TEM Selected Area Electron Diffraction (SAED). Then, their lattice constants, the orientation relationships with the β matrix and the atomic scale morphology are fully determined. Finally, the formation strain paths and the transformation mechanisms of the hexagonal structures are fully revealed through crystallographic analyses. The results provide new information on the formation mechanism of the hexagonal structures in a BCC matrix.

5.2 Experimental

In this chapter, an annealed Cu-40%Zn sheet was used. It was further treated by ECP under a current density of about 17.01 kA/ mm^2, with the pulse duration of 125 μs, corresponding to the temperature of about 876°C. The detailed information on sample preparation can be found in §2.1 (p21). The microstructural examinations were performed using the SEM - EBSD. The chemical composition of the constituent phases was analyzed by the electron probe microanalysis using an FEG-EPMA instrument. The nano scaled microstructural and crystallographic features of the β phase was analyzed using the TEM. The atomic scaled microstructures were analyzed by high-resolution STEM. The single-crystal TEM electron diffractions and the atomic correspondences of the different phase were simulated using the Crystal Maker® software and the transformation lattice strains were represented with the deformation gradient tensors.

5.3 Results

5.3.1 Microstructural characteristics

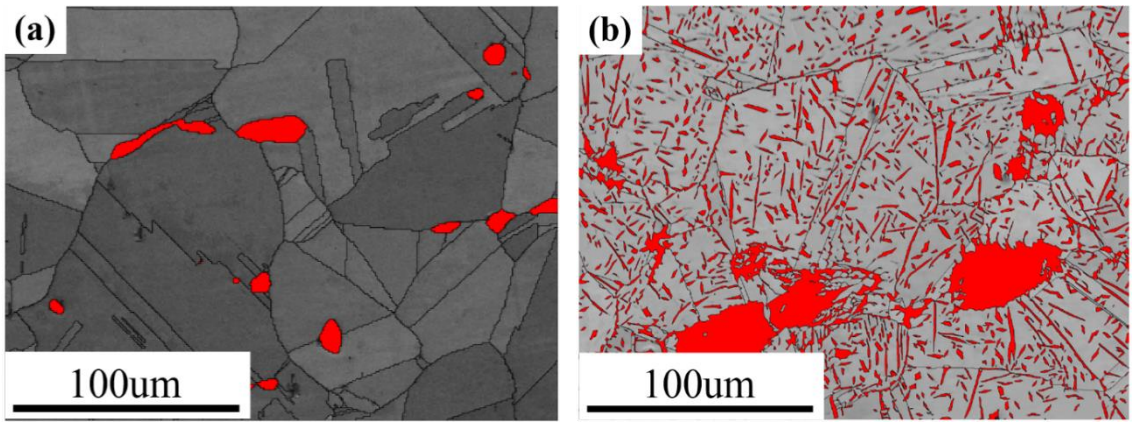


Fig. 5.1 SEM-EBSD micrographs of the annealed Cu-40%Zn alloy before (a) and after (b) ECP treatment, where the β phase is in red and the α phase is in gray according to the EBSD band quality indices.

Figure 5.1 (a) and **(b)** show the EBSD micrographs of the annealed Cu-40%Zn alloy before and after the ECP treatment, where the β phase is in red and the α phase in gray (EBSD band quality index contrast). It is seen from **Fig. 5.1 (a)** that the annealed microstructure is mainly composed of α phase with a slight amount of block shaped β phase that is formed during the solidification process. After the ECP treatment, numerous fine β precipitates with bar shape formed in the α grains, as shown in **Fig. 5.1 (b)**. The concentration of the solute atom, Zn, in the ECP induced β precipitates are given in **Table 5.1**. It can be seen that the repartition of Zn happened with the transformation. The Zn concentration in the α phase and the in the β precipitates are very close to those of their equilibrium state. This demonstrates that atom diffusion happened during the α to β transformation induced by the ECP treatment even though the transformation time is very short. Next only the β phase of the ECPed Cu-40%Zn alloy will be investigated.

Table. 5.1 Chemical concentration of Zn in the β and α phases in the annealed and the ECPed Cu-40%Zn samples. For the ECPed sample, the chemical concentration of Zn of the β phase is from the ECP induced β precipitates.

Zn%	β	α
Heat Treatment	46.23 ± 0.75	38.72 ± 0.31
ECP Treatment	46.71 ± 1.72	39.40 ± 0.56

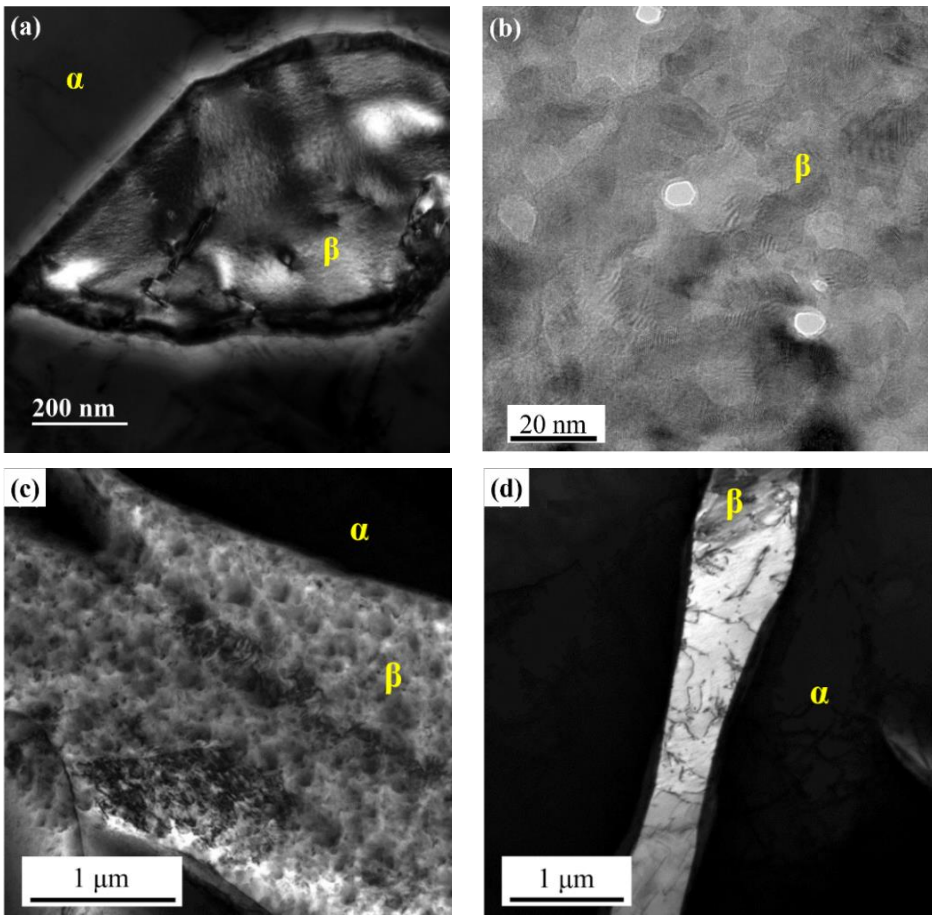


Fig. 5.2 TEM bright-field micrographs of the β precipitates in the ECPed Cu-40%Zn samples.

Figure 5.2 shows the TEM bright-field micrograph of one of the β precipitates in the ECP treated sample. The TEM diffraction contrast reveals the existence of fine and differently oriented striations that are homogeneously distributed throughout the β precipitates, as shown in **Fig. 5.2 (a)** and **(b)**. This suggests that some fine sub structures exist in the β precipitates. In addition, it can also be found that the β phase possess numerous dislocations located in the grain interiors, as shown in **Fig. 5.2 (c)** and **(d)**. That further proves that the β precipitates are not perfect crystals. It should be mentioned that the original β phase before and after the ECP treatment possesses the same characteristics. Thus, only on the β precipitates induced by the ECP treatment will be focused below.

5.3.2 Identification of sub structures in β precipitates

Figure 5.3 (a) shows a typical $[010]_{\beta}$ zone axis TEM Selected Area Electron Diffraction (SAED) pattern of the ECP induced β precipitates. In the $[010]_{\beta}$ zone axis diffraction pattern (**Fig. 5.3** (a)), two sets of diffraction spots are visible. The one is from the high-intensity spots plus the low intensity

but sharp super lattice spots that are from the ordered BCC β phase (B_2), as outlined with the black frame in the figure. This diffraction pattern confirms that the ECP induced β precipitates possess an ordered BCC structure that is typical for the Cu-Zn alloys. The others are composed of low intensity and diffuse spots located at the 1/2 $\{130\}_\beta$ reflection positions, as outlined with the dashed frames in **Fig. 5.3 (a)**. These low-intensity diffraction spots at the 1/2 $\{130\}_\beta$ diffraction positions correspond to the reflections from a crystal structure of the η phase - (Cu_2Zn_{98} that is a known phase in the Cu-Zn alloys) and also correspond to the HCP α structure in the Ti and Zr alloys. Hereafter we denote it η structure instead of α structure to avoid confusion, as in the Cu-Zn alloy system, α phase exists but the structure is FCC. In the $[010]_\beta$ zone axis pattern, two orientation variants of such a structure are visible, as indicated with the blue and green frames. The spots located at the 1/2 $\{110\}_\beta$ reflection positions marked with the red boxes in **Fig. 5.3 (a)** are double reflections from the $(0\bar{1}11)_\eta$ and $(01\bar{1}1)_\eta$ planes of the η structure. The simulated SAED patterns of the two variants are shown in **Fig. 5.3 (b)**. This structure is hexagonal. Further crystallographic examination confirmed that the η structure is related to the β structure with the BOR, i.e., $\{110\}_\beta//\{0001\}_\eta$, $<1\bar{1}1>_\beta//<11\bar{2}0>_\eta$. This result shows that the β precipitates are not purely ordered BCC but each contains other nano-scaled structures.

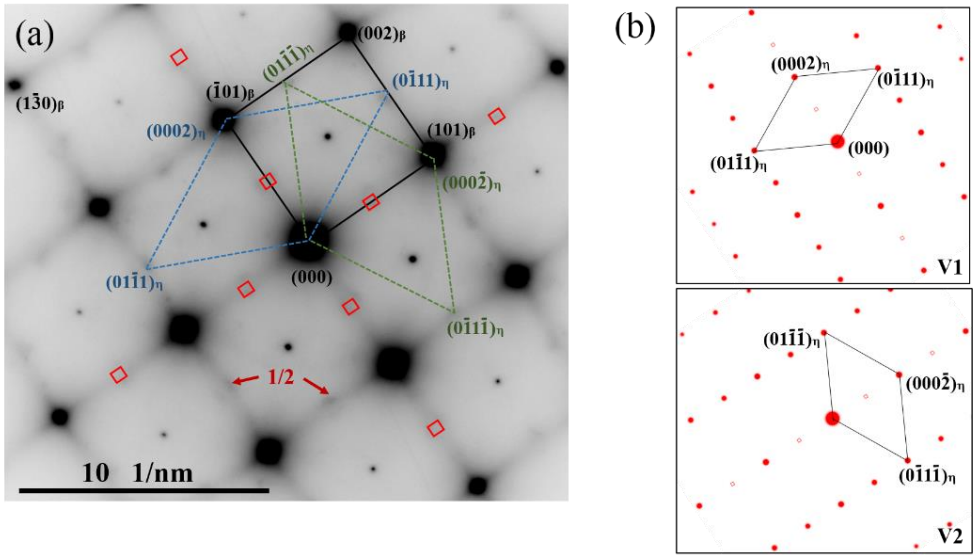


Fig. 5.3 (a) TEM $[010]_\beta$ zone axis Selected Area Electron Diffraction (SAED) pattern of the β precipitates Cu-40％Zn sample after ECP treatments. (b) Simulated SAED patterns of the η structure from two crystallographic orientation variants. Double reflections are marked with the red boxes in (a) and represented with empty squares in (b).

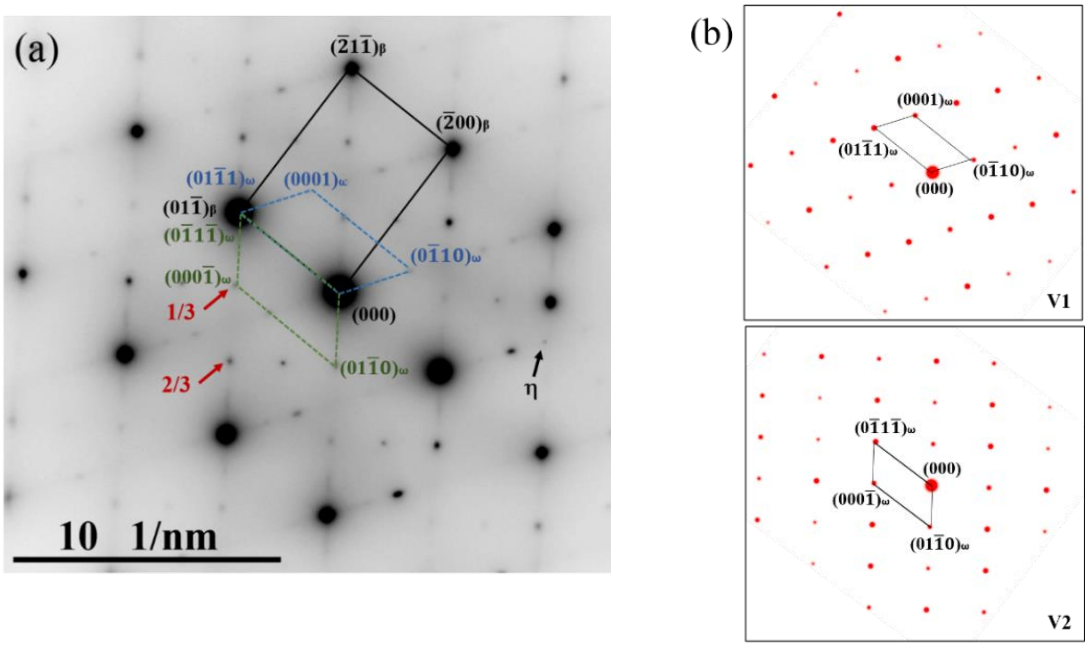


Fig. 5.4 (a) TEM $[011]_\beta$ zone axis SAED pattern of the β precipitates in the Cu-40%Zn samples after ECP treatment. (b) Simulated SAED patterns of the two ω variants.

Figure 5.4 shows a typical $[011]_\beta$ zone axis TEM SAED pattern of the ECP induced β precipitates. Three sets of diffraction spots were observed, as shown in **Fig. 5.4 (a)**. The first set is of high-intensity spots plus the low intensity but sharp super lattice spots from the ordered β structure as outlined with the black frame in the figure. The second set is of low intensity spots, appearing at the 1/3 and 2/3 $\{112\}_\beta$ reflection positions, as outlined with the dashed frames in **Fig. 5.4 (a)**. These spots correspond to the reflections from a ω structure in the BCC ordered β phase in the Cu-Zn alloys. Such a structure corresponds to that of the σ phase ($CuZn_3$) that is stable at high temperature. It has a hexagonal structure. Further crystallographic examination confirmed that the ω structure is related to the β structure with the Blackburn OR, i.e., $\{111\}_\beta//\{0001\}_\omega$, $<1\bar{1}0>_\beta//<11\bar{2}0>_\omega$. In the $[011]_\beta$ zone axis SAED pattern, there are two sets of ω patterns that are from two crystallographic orientation variants, as outlined with the respective blue and green frame in **Fig. 5.4 (a)** and the simulated SAED patterns are shown in **Fig. 5.4 (b)**. This result indicates that in addition to the η structure, the β phase also contains another structure, the ω structure. The third set is of some faint and diffuse spots appearing at the 1/2 $\{112\}_\beta$ reflection positions, as indicated in **Fig. 5.4 (a)**. These spots correspond to the reflections from the η structure that has been observed in **Fig. 5.4 (a)**. It should also be noted that the SAED patterns in **Fig. 5.3 (a)** and **Fig. 5.4 (a)** possess one common feature, i.e., the presence

of fine streaks continuous between the diffraction spots of the two structures and passing through the origin (transmitted beam) of the diffraction pattern. This is the characteristic of the scattering effect arising from crystal size. The fine streaks indicated that the two structures are very small in size. Although the diffraction spots from these structures are visible in the SAED patterns, the dark field micrographs produced using their reflections are very faint and the corresponding structures could not be illuminated. To visualize the atomic arrangements of the two structures, high resolution STEM examinations were conducted.

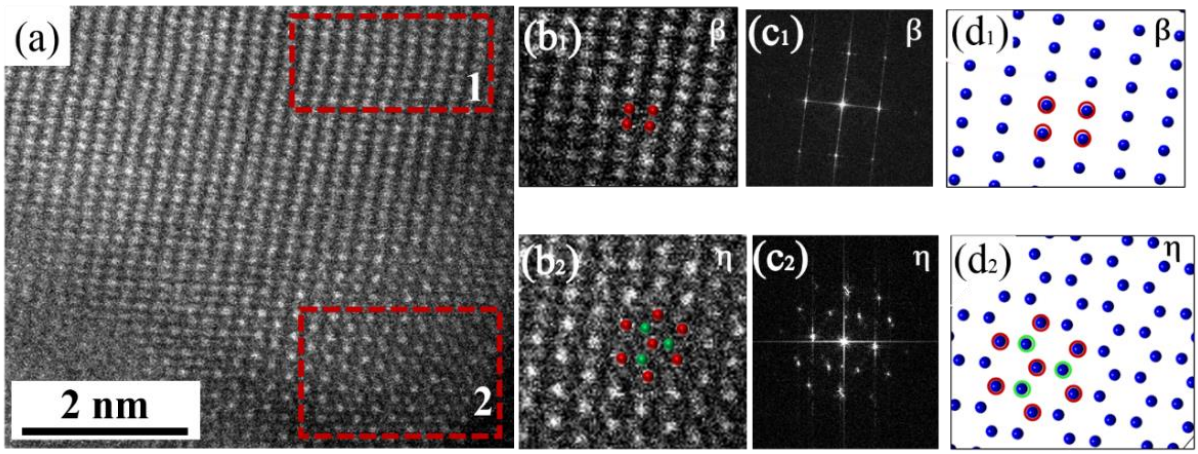


Fig. 5.5 (a) STEM-HAADF micrograph of the ECP induced β precipitates viewed in the $[011]_{\beta}$ direction. (b_1) and (b_2) A typical example of the regions marked with rectangles 1 and 2, respectively. (c_1) and (c_2) The inverse Fourier transforms of the regions marked by rectangles 1 and 2, respectively. (d_1) and (d_2) The simulated projection of the atom columns from the corresponding ideal structures of BCC β and hexagonal η, respectively. For the η structure, the red symbols mark the atomic positions on the upper layer, whereas the green ones outlined the atomic positions in the lower layer.

Figure 5.5 (a) shows the STEM-HAADF micrograph of the ECP induced β precipitate acquired with the $[011]_{\beta}$ parallel to the incident-beam. The atomic arrangement zones corresponding to the BCC β structure (Zone 1) and the η structure (Zone 2) are well visible, as outlined with the red dashed rectangles in **Fig. 5.5 (a)** and further magnified in **Fig. 5.5 (b)** (labeled with the same numbers as in **Fig. 5.5 (a)**). The corresponding fast Fourier transform (FFT) image serving as the diffraction patterns of these zones and the $[011]_{\beta}$ projection of the atom columns of the two structures are given in **Fig. 5.5 (c)** and **(d)** (labeled with the same numbers as in **Fig. 5.5 (a)**). Comparing the FFT images in **Fig. 5.5 (c_2)** with the diffraction pattern of the η structure in **Fig. 5.4 (a)** and the atomic arrangement in **Fig. 5.5 (b_2)** with that in **Fig. 5.5 (d_2)**, the η structure in Zone 2 is confirmed.

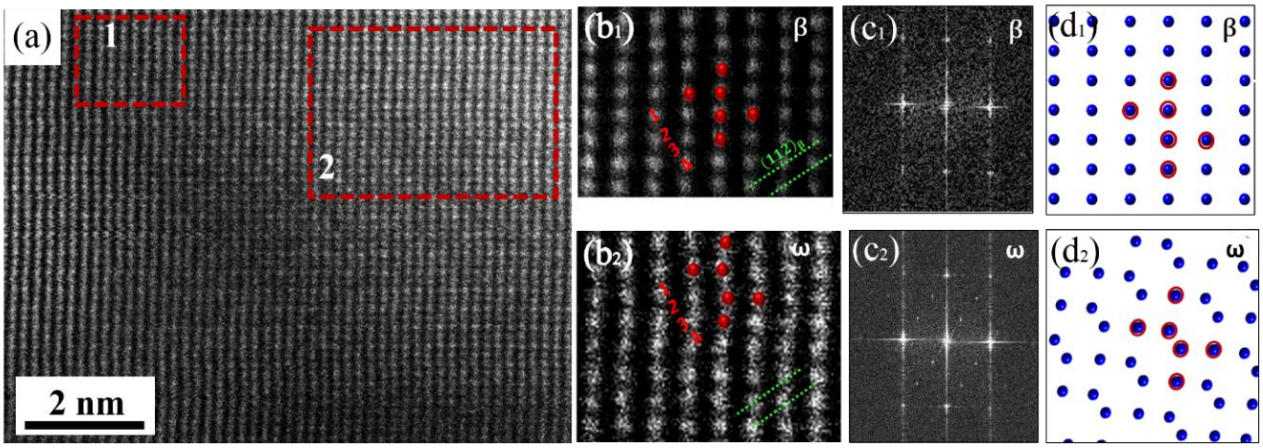


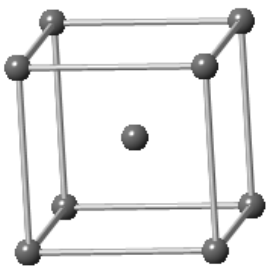
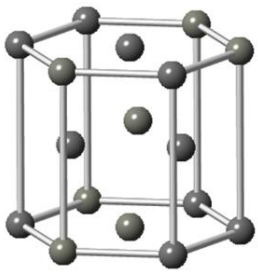
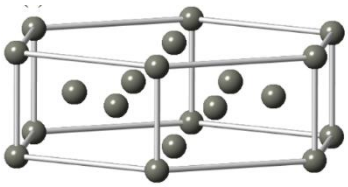
Fig. 5.6 (a) STEM-HAADF micrograph of the β matrix viewed in the $[011]_\beta$ direction in the ECP induced β precipitates. (b_1) and (b_2) typical examples of the regions marked by rectangles 1 and 2, respectively. (c_1) and (c_2) The Fourier transforms from the regions marked with rectangles 1 and 2, respectively. (d_1) and (d_2) The simulated projected atom columns from the corresponding perfect β and ω structures. The atomic cells are marked with the red symbols.

Figure 5.6 (a) shows a STEM-HAADF micrograph of the ECP induced β precipitate acquired in the area with the $[011]_\beta$ parallel to the incident-beam. Two characteristic atomic arrangements possessing the BCC β structure and the ω structure are outlined with the respective red rectangles (Zone 1 and 2) and further magnified in **Fig. 5.6 (b)** with the corresponding FFT image in **Fig. 5.6 (c)** (labeled with the same numbers as in **Fig. 5.6 (a)**). Zone 1 demonstrates the perfect β atomic arrangement in the BCC structure. The FFT image in **Fig. 5.6 (c_1)** well reproduces the $[011]_\beta$ zone axis SAED pattern. For reference, the projected atom columns from the perfect β structure is shown in **Fig. 5.6 (d_1)**. It is seen that the simulated projection of the atom columns (**Fig. 5.6 (d_1)**) well corresponds to the images of the β phase in Zone 1 (**Fig. 5.6 (b_1)**). Zone 2 corresponds to the ω structure. The FFT image in **Fig. 5.6 (c_2)** well reproduces the SAED pattern of the ω structure in the $[011]_\beta$ zone axis SAED pattern, i.e., the appearance of the additional spots at 1/3 and 2/3 $\{112\}_\beta$ reflection positions. For reference, the projected atom columns from the perfect ω structure is also shown in **Fig. 5.6 (d_4)**. From **Fig. 5.6 (b_2)**, it is found that the appearance of the diffraction spots at the 1/3 and 2/3 $\{112\}_\beta$ reflection positions results from the atomic shuffles on every second and third $\{112\}_\beta$ planes, as indicated in **Fig. 5.6 (b_2)**. Comparing the atomic arrangement in **Fig. 5. 6 (b_2)** with that of the ideal atomic arrangement of the ω structure displayed in **Fig. 5.6 (d_2)**, one can find that the structure giving the ω diffraction is in the course of the structure transformation from the BCC β

structure to the hexagonal ω structure.

Furthermore, the lattice constants of the β, η and ω structures were measured from the STEM-HAADF micrographs and listed in **Table 5.2**. The data were measured from 20 atom rows from each of 6 images that were taken with the incident beam either parallel to the $[011]_\beta$ or to the $[001]_\beta$ direction. For the β phase, the $(110)_\beta$, $(200)_\beta$, $(130)_\beta$ and $(112)_\beta$ planes were used to measure the lattice parameters. For the η structure, the $(0002)_\eta$, $(0\bar{1}11)_\eta$, $(10\bar{1}0)_\eta$ and $(1\bar{1}00)_\eta$ planes were used and for the ω structure the $(0001)_\omega$, $(00\bar{1}0)_\omega$ and $(01\bar{1}1)_\omega$ planes were used. It should be noted that the standard deviations displayed in the table indicate rather the lattice constant deviations than measurement errors. The relatively large spread of the lattice constants demonstrates the existence of structure fluctuations in the two hexagonal distortions. During the measurements, we found that the fluctuation zones are very local involving only 2 or 3 atoms in each measured atom row. In the long range over the entire domain of each hexagonal structure, the negative and positive fluctuations tend to cancel out and the lattice constants converge to the average values. These measured lattice constants of the three structures allow accurate analyses of the lattice strains for the structure transformation, as will be demonstrated later.

Table. 5.2 Lattice constants of β, η and ω structures in ECPed Cu-40%Zn sample and the illustration of the crystal structures. The data were measured from 20 atom rows from each of 6 images that were taken with the incident beam either parallel to the $[011]_\beta$ or to the $[001]_\beta$ direction. The standard deviations indicate rather the spread of the lattice constants than measurement errors.

	β	**η**	**ω**
a	2.91 ± 0.06 Å	2.53 ± 0.05 Å	4.09 ± 0.11 Å
c	/	4.47 ± 0.31 Å	2.51 ± 0.07 Å
Average c/a	/	1.76	0.61
Structure			

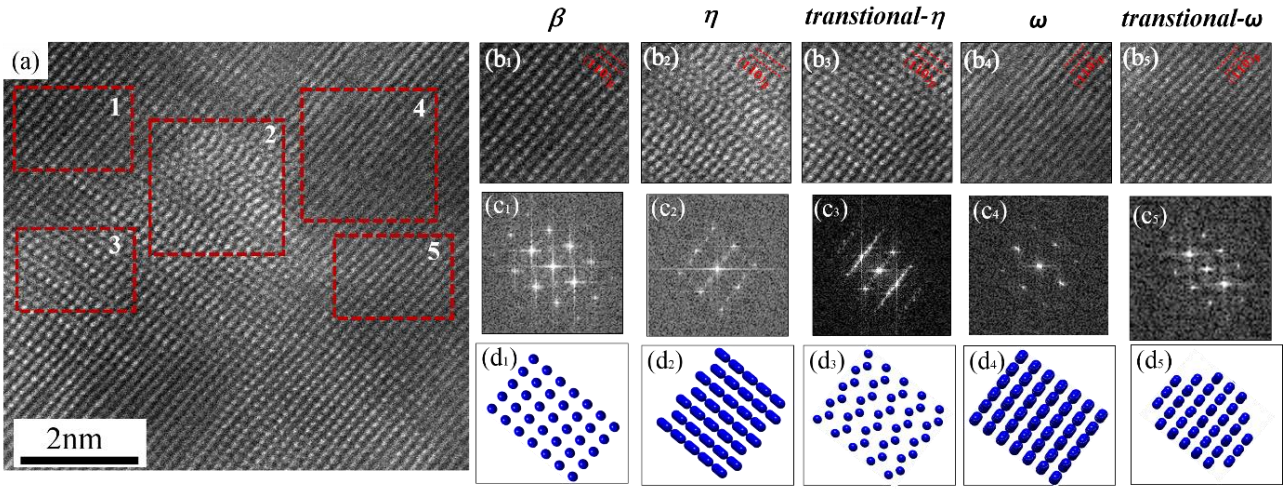


Fig. 5.7 (a) STEM-HAADF micrograph of the matrix viewed in the $[001]_\beta$ direction in the ECP induced β precipitates of the Cu-40%Zn alloy after ECP treatment. (b_1), (b_2), (b_3), (b_4) and (b_5) typical examples of the regions marked by rectangles 1, 2, 3, 4 and 5, respectively. (c_1), (c_2), (c_3), (c_4) and (c_5) FFTs performed in the regions marked by rectangles 1, 2, 3, 4 and 5, respectively. (d_1), (d_2), (d_3), (d_4) and (d_5) The simulated projected atom columns from the corresponding perfect structures, respectively.

To further analyze the transition of the atomic shuffles or displacements from the β structure to the two hexagonal structures and their spatial relation, the atomic arrangements of the two hexagonal structures in the $[001]_\beta$ zone axis STEM-HAADF micrographs were examined. **Fig. 5.7 (a)** shows an example of the STEM-HAADF micrograph of the ECP induced β precipitate acquired in the area with the $[001]_\beta$ parallel to the incident-beam where the two structures co-exist with the β matrix. The characteristic atomic arrangement zones of the BCC β structure (Zone 1), the η structure (Zone 2) and the near ω structure (Zone 4), and the zones presenting the lattice deformation in the course to change from the BCC β to the respective two structures (Zone 3 and 5) are well visible, as outlined with the red dashed rectangles in **Fig. 5.7 (a)** and further magnified in **Fig. 5.7 (b)** (labeled with the same numbers as in **Fig. 5.7 (a)**). The corresponding FFT images serving as the diffraction patterns of these zones are given in **Fig. 5.7 (c)** (labeled with the same numbers as in **Fig. 5.7 (a)**). For reference, the projected atom columns from the perfect β, η and ω structures are shown in **Fig. 5.7 (d_1)**, **(d_2)** and **(d_4)**. Analysis showed that Zone 2 corresponds to the atomic positions of the η structure, whereas Zone 4 to that of the ω structure. It should be noted that when the incident beam is in the $[010]_\beta$ direction of the β phase, the parallel direction of the ω structure is the $[\overline{0.1103}\ \ 0.1103\ 0\ 0.2229]_\omega$. This zone axis diffraction pattern is superimposed with the $[010]_\beta$ zone

axis pattern. Thus in the $[010]_\beta$ zone axis SAED pattern in **Fig. 5.3 (a)**, we could not identify the existence of the ω structure. However, in the STEM-HAADF micrograph in **Fig. 5.7 (a)** we can easily find this structure. Moreover, we can find that the two structures (η and ω) have neither fixed borders nor constant shape but they are always located next to each other, suggesting that they are concomitant. In either of the zone, the two hexagonal structures are also not constant. With the spread-out of the two structures, the atom positions change from the more or less perfect hexagonal structures to the perfect BCC structure of the β phase. Thus, the transition regions between the β structure and either of the two structures can be regarded as structure transition regions that can also be considered as specifically deformed β structure. For example, Zone 3 in **Fig. 5.7 (a)** can be regarded as the transition structure toward the η structure, as it is in the continuity of the corresponding structure. Zone 5 in the **Fig. 5.7 (a)** can be regarded as the transition structure toward the ω structure, as it is in the continuity of the corresponding structure. As the transitional zones are specifically deformed β structure, their lattice deformation features will be analyzed by examining the streaking features of the β diffraction spots in the SAED patterns, as detailed in the next section.

5.3.3 Identification of atomic shuffling and displacement system to realize the structure change

As the formation of the two structures is realized by atomic displacement or shuffle, it is important to identify the displacement or shuffle systems (plane and direction) to understand the formation of the transitional structures and the final structure change. The transitional regions that can be regarded as the deformed β structure would modify the shape of the diffraction spots of the β phase and thus the shape characters of the β diffraction spots allow obtaining the required information. **Fig. 5.8** and **Fig. 5.9** display several characteristic β zone axis TEM SAED patterns ($[010]_\beta$-$[011]_\beta$ in **Fig. 5.8** and $[111]_\beta$-$[113]_\beta$ in **Fig. 5.9**). It is seen that apart from the fine streaks passing through all the diffraction spots including the origin (the transmitted beam) there are two features associated with the diffraction spots of the β phase. The first is that the β diffraction spots are all elongated in certain reciprocal directions, forming the so-called relrods and the elongation increases with the increasing order of diffraction, as indicated by the yellow arrow in **Fig. 5.9 (a)**, as an example. The second is that the relrods exhibit characteristic extinction. These features suggest that the appearance of the

relrods is from planar crystal defects [220] that that should be related to the atomic shuffle or displacement. Systematic examination revealed that the β spots are elongated in two families of reciprocal directions <110>$_\beta$ and <112>$_\beta$, as indicated with the respective red and green bars in **Fig. 5.8** and **5.9**. It has well been established that the atomic displacement or shuffle in certain directions on the atomic planes will result in the extension of diffracted intensity along the normal to the shear planes [230]. The two reciprocal directions in the present work correspond to the normal of two crystalline planes of the β phase, i.e., the $\{110\}_\beta$ and $\{112\}_\beta$ plane, as the β phase possesses a cubic structure. This evidences that there exists atomic displacement or shuffle on the $\{110\}_\beta$ and $\{112\}_\beta$ planes in the β phase.

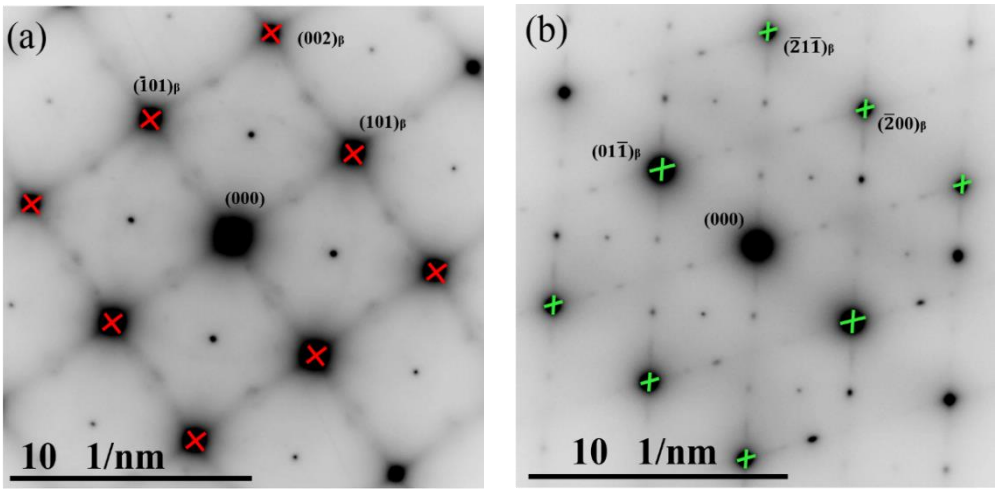


Fig. 5.8 TEM SAED patterns of (a) $[010]_\beta$ and (b) $[011]_\beta$ zone axis of the ECP induced β precipitates. The <110>$_\beta$ relrods are marked in red and the <112>$_\beta$ relrods are marked in green.

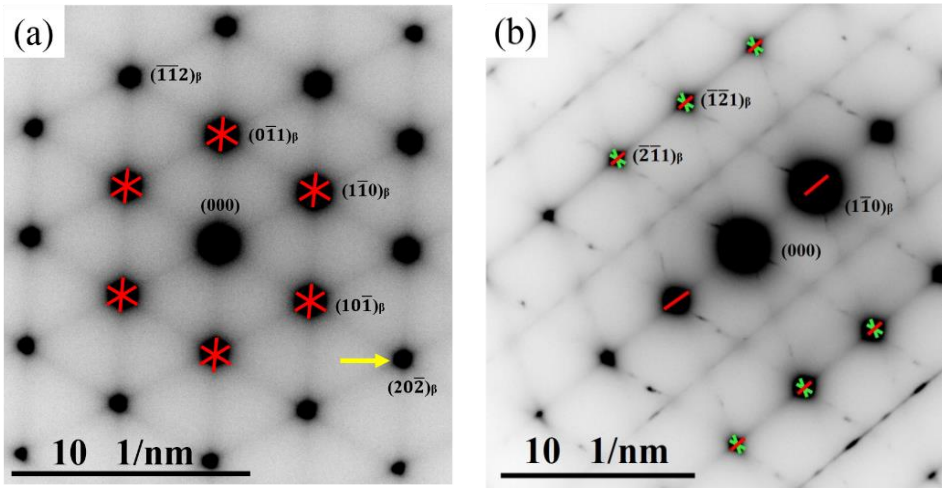


Fig. 5.9 TEM SAED patterns of (a) $[111]_\beta$ and (b) $[113]_\beta$ zone axis of ECP induced β precipitates. The <110>$_\beta$ relrods are marked in red and the <112>$_\beta$ relrods are marked in green. The yellow arrow in (a) indicates an example of the increased streaking of the $(20\bar{2})_\beta$ spot.

It is also well established in the theory of electron diffraction that if the vector of the atomic displacement (resembling dislocation Burgers vector) on the plane (denoted ***u*** in the present work) is lying on the planes of the operating reflections, the extended diffraction intensity (corresponding to the relrod) from the faulted plane disappears, i.e., the relrod that is parallel to the normal of the shear plane disappear from the diffraction spots. So the characteristic extinction of the relrods allow finding the displacement vectors or the displacement directions. In the two zone axis patterns in **Fig. 5.8** the $<110>_\beta$ relrods exist in the $[010]_\beta$ pattern but not in the $[011]_\beta$ pattern although in the two patterns the $<110>_\beta$ reciprocal direction exist (the $\pm [01\bar{1}]_\beta$ reciprocal direction in **Fig. 5.9 (b)**), evidencing the extinction of the $[01\bar{1}]_\beta$ relrod. However, in the two zone axis patterns in **Fig. 5.9**, the $<112>_\beta$ relrods are present in the $[113]_\beta$ pattern but not in the $[111]_\beta$ pattern although the $<112>_\beta$ reciprocal directions present in the two patterns. This evidences the extinction of the $<112>_\beta$ relrods. To find out the possible displacement vectors on the two defaulted planes, the invisibility of all the dislocation Burgers vectors published in the literature (<112>, <101>, <111>) in BCC crystals for the reflections in the two zone axes (the $[011]_\beta$ zone axis reflections for the $\{110\}_\beta$ extinctions and the $[111]_\beta$ zone axis reflections for the $\{112\}_\beta$ extinctions) are verified. The results show that the extinction of the $<110>_\beta$ relrods at the reflections in the $[011]_\beta$ axis zone (**Fig. 5.8 (b)** is from the $<011>_\beta$ displacement on the $\{110\}_\beta$, as shown in **Table 5.3**. The $\boldsymbol{g \cdot u}=0$ is fulfilled for all the reflections in the $[011]_\beta$ zone axes (highlighted in bold) but is not for those in the $[010]_\beta$ zone axes. This indicates that the formation of the $<110>_\beta$ relrods is originated from the atomic shuffle or displacement on the $(01\bar{1})_\beta$ plane in the $[011]_\beta$ direction. This result evidences the activation of the $\{110\}_\beta <1\bar{1}0>_\beta$ shuffle or shear system in the β precipitates. However, the extinction of the $<112>_\beta$ relrods at the reflections in the $[111]_\beta$ zone axes (**Fig. 5.9 (a)**) is from the atomic displacement in the $[111]_\beta$ direction, as shown in **Table 5.4**. The $\boldsymbol{g \cdot u}=0$ is fulfilled for all the reflections in the $[111]_\beta$ axis zone (highlighted in bold) but not for those in the $[113]_\beta$ zone axes. This indicates that the formation the $<112>_\beta$ relrods is originated from the atomic shuffle or displacement on the $(11\bar{2})_\beta$ plane in the $[111]_\beta$ direction. This result evidences the activation of the $\{112\}_\beta <1\bar{1}1>_\beta$ shuffle or shear system in the β precipitates. The atomic shuffles or displacement on these two systems should be related to the low energy or soft phonon modes in the BCC structure, as have been revealed by many experimental and theoretical investigations. Thus

the two kinds of atomic shuffle or displacement in the present work should be in relation to the formation of the η and ω structures in the β precipitates.

Table 5.3 g·u for the reflections in the $[010]_\beta$ and $[011]_\beta$ zone axis diffraction patterns in ECP induced β phase.

	Zone axis	$[010]_\beta$			$[011]_\beta$		
Shear plane	**u** \ **g**	$(101)_\beta$	$(002)_\beta$	$(\bar{1}01)_\beta$	$(\bar{2}1\bar{1})_\beta$	$(\bar{2}00)_\beta$	$(01\bar{1})_\beta$
$(01\bar{1})_\beta$	$[011]_\beta$	≠0	≠0	≠0	**=0**	**=0**	**=0**
$(1\bar{1}0)_\beta$	$[110]_\beta$	≠0	=0	≠0	≠0	≠0	≠0
$(110)_\beta$	$[\bar{1}10]_\beta$	≠0	=0	≠0	≠0	≠0	≠0
$(011)_\beta$	$[0\bar{1}1]_\beta$	≠0	=0	≠0	≠0	=0	≠0
$(10\bar{1})_\beta$	$[101]_\beta$	≠0	≠0	=0	≠0	≠0	≠0
$(101)_\beta$	$[\bar{1}01]_\beta$	=0	≠0	≠0	≠0	≠0	≠0

Table 5.4 g·u for reflections in the $[111]_\beta$ and $[113]_\beta$ zone axis diffraction patterns in ECP induced β phase.

	Zone axis	$[111]_\beta$				$[113]_\beta$		
Shear plane	**u** \ **g**	$(10\bar{1})_\beta$	$(1\bar{1}0)_\beta$	$(0\bar{1}1)_\beta$	$(\bar{1}\bar{1}2)_\beta$	$(1\bar{1}0)_\beta$	$(\bar{2}\bar{1}1)_\beta$	$(\bar{1}\bar{2}1)_\beta$
$(11\bar{2})_\beta$	$[111]_\beta$	**=0**	**=0**	**=0**	**=0**	=0	≠0	≠ 0
$(\bar{2}11)_\beta$	$[\bar{1}11]_\beta$	≠0	≠0	=0	≠0	≠0	≠0	=0
$(121)_\beta$	$[1\bar{1}1]_\beta$	=0	≠0	≠0	≠0	≠0	=0	≠0
$(112)_\beta$	$[11\bar{1}]_\beta$	≠0	=0	≠0	≠0	=0	≠0	≠0

Based on the revealed shuffle systems and the orientation relationships between the parent β precipitates and the two structures, i.e., the Burgers OR ($\{110\}_\beta//\{0001\}_\eta$, $<1\bar{1}1>_\beta//<11\bar{2}0>_\eta$) between the β structure and the hexagonal η structure and the Blackburn OR ($\{111\}_\beta//\{0001\}_\omega$, $<1\bar{1}0>_\beta//<11\bar{2}0>_\omega$) between the β and the ω structure, the atomic correspondences of the transition structures or the deformed β structure to form the two hexagonal structures (η and ω) were further established, as shown in **Fig. 5.10** and **Fig. 5.11**, where the two end structures (the perfect β structure and the perfect hexagonal structure are also displayed as references). Careful examination of the

lattice distortion, we can find that each structure change involves two steps of atomic displacement.

For the β to η structure change, the first step is the atomic displacement of each second basal layer, the $\{110\}_\beta$ (circled in yellow in **Fig. 5.10** (a) and (b)), in the $<1\bar{1}0>_\beta$ direction by an amount of a/4 $<1\bar{1}0>_\beta$. Thus an intermediate structure can be obtained that is orthorhombic, as shown in **Fig. 5.10 (b)**. The second step is the atomic displacement of the two neighboring $\{110\}_\beta$ planes (parallel to the yellow circled planes in **Fig. 5.10 (a)**) to the hexagonal structure (**Fig. 5.10 (c)**). Then the intermediate η structure is projected along the $<001>_\beta$ direction and displayed in **Fig. 5.7 (d_3)**. Comparing the projected atom columns in **Fig. 5.7 (d_3)** with the STEM-HAADF images in **Fig. 5.7 (b_3)**, one can find the good coincidences between the two. This confirms that the formation of the transitional structure of η is indeed realized by the atomic displacement on every second $\{110\}_\beta$ and in the $<1\bar{1}0>_\beta$ direction and validates the two step structure change.

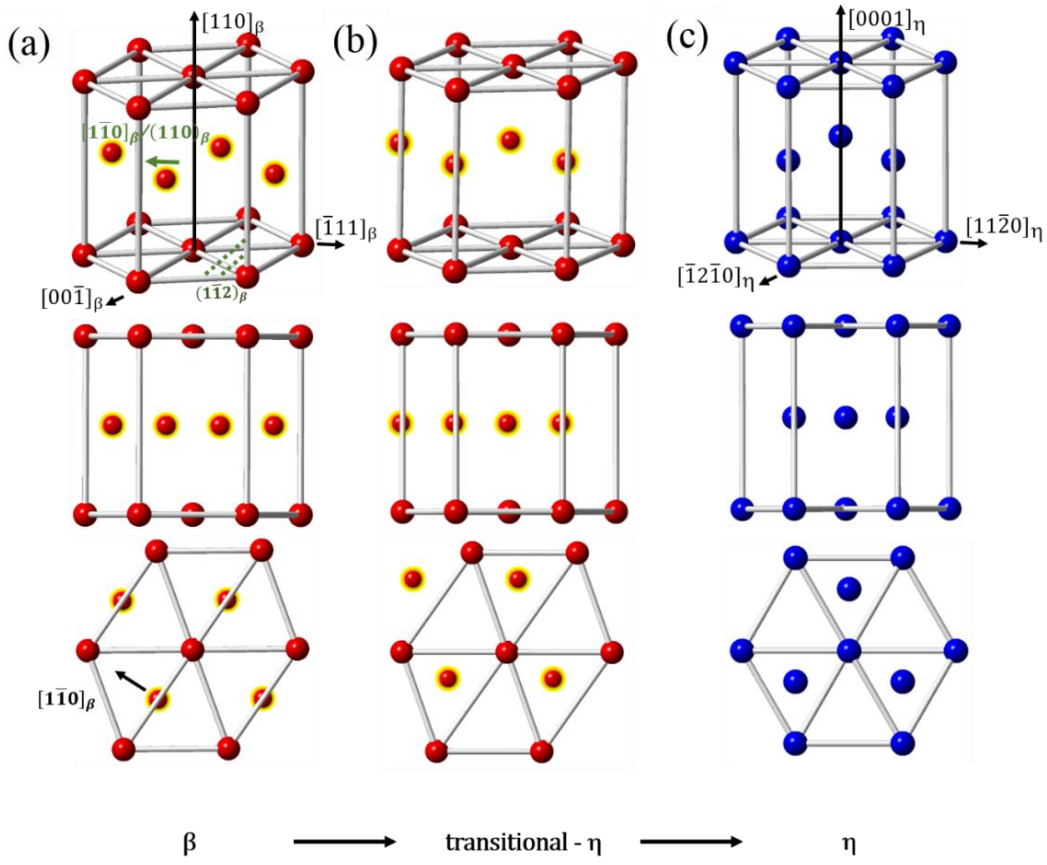


Fig. 5.10 3D, front view and top view of the lattice correspondences from β (a) to η (c) structure under the Burgers OR. The atoms of the parent β structure are in red and those of the product structure η in blue. The displaced atoms are marked with yellow circles. The $\{1\bar{1}2\}_\beta$ are shaded with the green dotted lines.

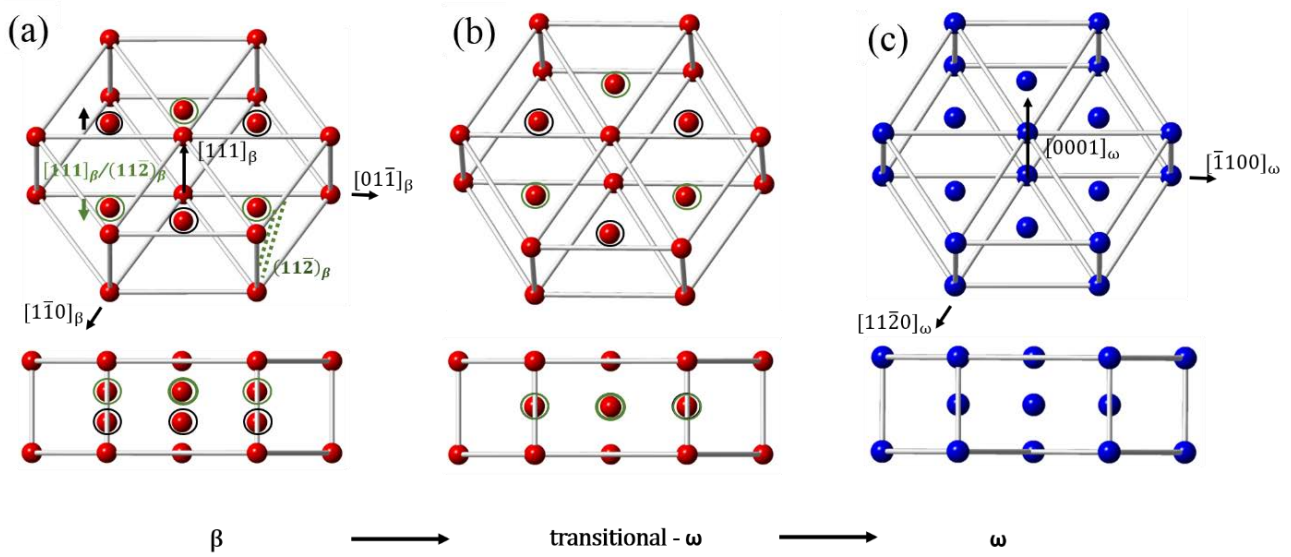


Fig. 5.11 3D and front view of the lattice correspondences from β (a) to ω structure (c) under the Blackburn OR. The atoms of the parent β structure are in red and those of the product structure ω in blue. The displaced atoms are marked with green (for the second $\{11\bar{2}\}_\beta$ layer) and black (for the third $\{11\bar{2}\}_\beta$ layer) circles. The first $\{11\bar{2}\}_\beta$ plane is shaded with the green dotted lines.

The similar analysis was also conducted for the β to ω structure change. This structure change also progresses in two steps. The first step is the atomic shuffle of each second and third $\{11\bar{2}\}_\beta$ plane (circled in green for the second layer and circled in black for the third layer in **Fig. 5.11 (a)** and **(b)**), in the $\pm[111]_\beta$ direction by an amount of a/12 $[111]_\beta$. The second step is the further atomic distortions of the two neighboring $\{11\bar{2}\}_\beta$ planes (the prismatic planes marked with green dotted lines in **Fig. 5.11 (a)**) to the hexagonal structure (**Fig. 5.11 (c)**). Then the intermediate ω structure is projected along the $<001>_\beta$ direction and displayed in **Fig. 5.7 (d_5)**. Comparing the projected atom columns in **Fig. 5.7 (d_5)** with the STEM-HAADF image in **Fig. 5.7 (b_5)**, one can find the good coincidences between the atomic arrangement in the STEM-HAADF image and the simulated projection. This further validates the two-stepped structure change.

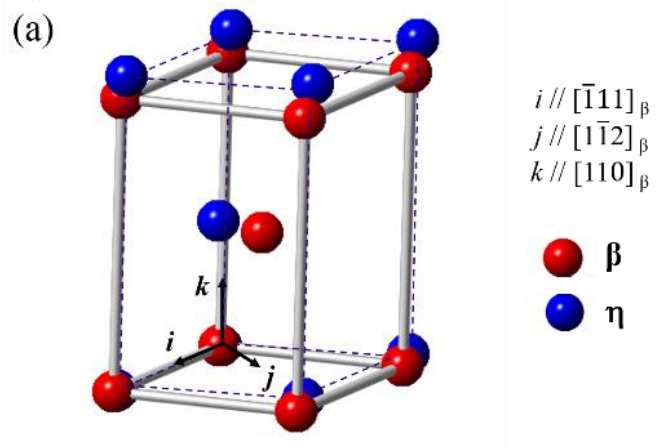
5.3.4 Origin of concomitant formation of the two hexagonal structures

As the formation of the two structures is realized by atomic shuffle or displacement, the co-existence of the two structures should be related to the lattice deformation associated to the structure transformation. Thus, the lattice strains to form the η structure and the ω structure under the respective OR ($\{110\}_\beta//\{0001\}_\eta$, $<1\bar{1}1>_\beta//<11\bar{2}0>_\eta$; $\{111\}_\beta//\{0001\}_\omega$, $<1\bar{1}0>_\beta//<11\bar{2}0>_\omega$) were analyzed using

the lattice constants list in **Table 5.2** and represented with the deformation gradient tensor expressed in the corresponding OR reference system (*i*-*j*-*k*) (as illustrated in **Fig. 5.12**) and displayed in **Table 5.5**. It should be mentioned that the lattice deformation described by the tensors for the two structures is only applicable to the second step of the structure change. This further confirms that the formation of the two new structures progresses in two steps. The first step is realized by the atomic shuffle on the two shear systems other than the deformation described by the tensors in **Table 5.5**.

Table. 5.5 Deformation gradient tensors of structure deformation in the second-step to form the two structures expressed in the corresponding OR reference frame. The strain components in each tensor were calculated using the averge lattice constants of each concerned structure.

Structure change	**OR**	**Deformation Gradient Tensor**	**Volume change**
β → η	$\{110\}_\beta$ // $\{0001\}_\eta$ $\langle\bar{1}11\rangle_\beta$ // $\langle11\bar{2}0\rangle_\eta$	$i\|\|[\bar{1}11]$ $j\|\|[1\bar{1}2]$ $k\|\|[110]$ $\begin{bmatrix}1.0039 & -0.1775 & 0\\ 0 & 0.9222 & 0\\ 0 & 0 & 1.0862\end{bmatrix}$	0.55%
β → ω	$\{111\}_\beta$ // $\{0001\}_\omega$ $\langle1\bar{1}0\rangle_\beta$ // $\langle11\bar{2}0\rangle_\omega$	$i\|\|[1\bar{1}0]$ $j\|\|[11\bar{2}]$ $k\|\|[111]$ $\begin{bmatrix}0.9941 & 0 & 0\\ 0 & 0.9941 & 0\\ 0 & 0 & 0.9960\end{bmatrix}$	-0.15%



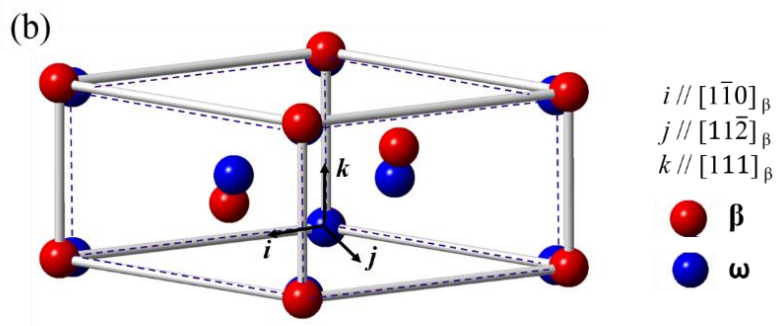


Fig. 5.12 Lattice correspondences (a) between β and η structure under the Burgers OR and (b) between β and ω structure under the Blackburn OR. The OR reference systems (*i*-*j*-*k*) are set with direction *i* parallel to the OR direction, *k* to the direction normal to the OR plane and *j* to the vector cross product of *k* and *i*. The lattice points of the parent β phase are in red and those of the product structures (η, ω) in blue.

It is seen from **Table 5.5** that for the formation of the η structure it requires an respective elongation in the $[\bar{1}11]_\beta$ direction (by 0.39%), and in the $[110]_\beta$ direction (by 8.62%), and a contraction in the $[1\bar{1}2]_\beta$ direction (by 7.78%). The transformation also requires a shear of -0.1175 on the $(1\bar{1}2)_\beta$ plane and in the $[\bar{1}11]_\beta$ direction. Thus the soft $\{110\}_\beta<1\bar{1}0>_\beta$ system allows the atomic shuffle to form the transition structure of the η structure (**Fig. 5.12 (b)**) and the soft shear system $\{1\bar{1}2\}_\beta<\bar{1}11>_\beta$ allows finalizing the structure transformation. However, the formation of the η structure yields an volume increase by 0.55% that is unfavorable during the cooling process, as by thermal dilatation, the overall volume of the material diminishes. For the ω structure, the transformation requires the β lattice to contract in the three principle directions: the $[1\bar{1}0]_\beta$ direction (by 0.59%), $[11\bar{2}]_\beta$ direction (by 0.59%) and the $[111]_\beta$ direction (by 0.40%), as summarized in **Table 5.5**. No shear is required. However, the formation of the ω structure yields a volume shrinkage (by 0.15%). This volume shrinkage should effectively cancel the volume increase of the formation of the η structure that is unfavorable during the cooling process. Clearly, the soft shear system $\{11\bar{2}\}_\beta<111>_\beta$ allows the atomic shuffle on this system to achieve the first step of the ω structure change. Thus the ω structure should be formed accompanying the formation of the η structure to minimize the overall lattice distortion energy in the β precipitates.

5.4 Summary

In the present work, the formation mechanisms of two nano-sized hexagonal structures (η and ω) in the ECP induced β precipitates in the ECPed Cu-40%Zn alloy was thoroughly investigated. The

results demonstrate that two kinds of hexagonal structures are formed in the ECP induced β precipitates by pure atomic shuffle and shear. The two structures are commonly featured with atomic clusters without fixed shape nor clear boundary with the β matrix and connected with the β matrix by structural transition regions.

For the η structure, it possess the crystal structure of the Cu_2Zn_{98} phase and obeys the Burgers OR ($\{110\}_\beta//\{0001\}_\eta$, $<1\bar{1}1>_\beta//<11\bar{2}0>_\eta$) with the β matrix. The formation of this structure involves two steps of lattice deformation. The first is the atomic shuffle on each second $\{110\}_\beta$ plane in the $<\bar{1}10>_\beta$ direction. Such atomic shuffle transforms the BCC structure of the β phase to an orthorhombic structure that exists in the transition regions between the matrix β and the η structure and produces the $<\bar{1}10>_\beta$ relrods in the TEM SAED patterns. The second step is to realize the structure change from the transitional orthorhombic structure to the hexagonal structure by mainly a shear on the $\{1\bar{1}2\}_\beta$ plane in the $<\bar{1}11>_\beta$ direction accompanied by small normal strains in the shear plane normal direction ($<112>_\beta$), in the shear direction ($<1\bar{1}1>_\beta$) and in the direction normal to this two ($<110>_\beta$).

For the ω structure, it possess the crystal structure of the $CuZn_3$ phase and obeys the Blackburn OR ($\{111\}_\beta//\{0001\}_\omega$, $<1\bar{1}0>_\beta//<11\bar{2}0>_\omega$) with the β matrix. The formation of this structure involves also two steps of lattice deformation. The first is the atomic shuffle on each second and third $\{11\bar{2}\}_\beta$ plane in the $\pm[111]_\beta$ direction, which creates an hexagonal structure. Such a structure constitutes of the transition regions between the matrix β and the ω structure and produces the $<112>_\beta$ relrods in the TEM SAED patterns. The second step is to realize the structure change from the transitional hexagonal structure to the final hexagonal structure by three normal strains in the $<111>_\beta$, $<11\bar{2}>_\beta$ and $<1\bar{1}0>_\beta$ directions. As the formation of the η structure yields a volume increase whereas that of the ω structure a volume decrease, the concomitant formation of the ω structures is to cancel the volume increase of the η structure and to minimize the overall lattice distortion energy.

The results of the present work, deepens the understanding of the formation mechanisms of the two hexagonal structures in B_2 β phase in Cu-Zn alloys that is a common feature of high temperature BCC phase in many other alloys systems, such as Ti alloys and Zr alloys.

Chapter 6 Conclusions and Perspectives

6.1 Conclusions

In the present work, a through experimental and theoretically crystallographic study on the microstructural evolution, the phase transformation orientation relationships (ORs), the crystal defects, the nanoscaled substructures of the product phase and the corresponding phase transformation path has been conducted on an annealed Cu-40%Zn alloy by the Electric Current Pulses (ECP) treatment. From the above experimental and calculation results, the main conclusions are drawn as follows:

(1) The microstructural evolution of the α to β heating phase transformation

Substantially fine β precipitates were retained to room temperature during the α to β phase transformation induced by ECP. With the increase of the electric current density, the amount of the β precipitates drastically increased. The formation sites of the β precipitates also increased from the random high angle α grain boundaries to the α grain interiors, and then to the K_1-Σ3 boundaries. The β precipitates in the α grain interiors are monolithic in bar shape that are encased in two pairs of parallel planes, $\{211\}_\alpha$ and $\{311\}_\alpha$ of α phase as the prismatic planes.

(2) Crystal defect associated selection of phase transformation ORs

The ECP induced β precipitates formed in the annealed α matrix follow different ORs depending on the formation site. The β precipitates obeys the K-S OR when formed along the α grain boundaries or in their vicinities, or the N-W OR when formed in the α grain interiors. In the former sites, the $\{111\}_\alpha/<1\bar{1}0>_\alpha$ dislocation arrays were frequently observed, whereas in the latter, the $\{111\}_\alpha/<11\bar{2}>_\alpha$ stacking faults were often found. Transformation strain analyses revealed that under the K-S OR the maximum lattice deformation required is a shear on the $\{111\}_\alpha$ plane in the $<1\bar{1}0>_\alpha$ direction, whereas under the N-W OR the maximum deformation is a shear on the $\{111\}_\alpha$ plane in the $<11\bar{2}>_\alpha$ direction. Thus the existing $\{111\}_\alpha/<1\bar{1}0>_\alpha$ dislocation arrays provide the favorable pre-strains to facilitate the formation of the β precipitates via the K-S path, whereas the $\{111\}_\alpha/<11\bar{2}>_\alpha$ stacking faults offer the favorable pre-strains for the formation of the β precipitates via the N-W path, resulting in the selection

of ORs for the α to β transformation.

(3) Crystal defects in α phase induced by ECP treatments

Various types of crystal defects were produced in the α matrix by the ECP treatments depending on the applied current density. For the ECPed sample at low current density, large amount of $\{111\}_\alpha$ /$<11\bar{2}>_\alpha$ stacking faults and then nano twins were formed in the α matrix. For the ECPed sample at high current density, dislocation nets appeared near the β precipitates that were composed of the $\{111\}_\alpha$/$<1\bar{1}0>_\alpha$ typed perfect dislocations and the Frank typed dislocations.

(4) The correlation between the dislocation nets and β precipitates

The formation reasons of the dislocations are related to the volume misfit during the rapid α to β phase transformation. The α to β transformation required an expansion along the $[1\bar{1}0]_\alpha$ direction and a contraction along the $[111]_\alpha$ direction. For the former, it resulted in the formation of the $\{111\}_\alpha<1\bar{1}0>_\alpha$ edge typed dislocation arrays in front of the $\{3\bar{1}1\}_\alpha$ broad faces. For the later, it induced the formation of the Frank typed dislocations in front of the $\{121\}_\alpha$ broad face. So, dislocation nets were formed along the edges of the broad faces of the β precipitate when the two kinds of dislocation arrays met in these regions.

(5) Two kinds nano-sized structures in the β precipitates

Two kinds of nano-sized hexagonal structures (η and ω) formed in the ECP induced β precipitates by pure atomic shuffle and shear without chemical repartition during the cooling process. The two structures are commonly featured with atomic clusters without fixed shape nor clear boundary with the β matrix and connected with the β matrix by structural transition regions.

For the η structure, it possess the crystal structure of the Cu_2Zn_{98} phase and obeys the Burges OR ($\{110\}_\beta//\{0001\}_\eta$, $<1\bar{1}1>_\beta//<11\bar{2}0>_\eta$) with the β matrix, giving rise to the additional diffraction spots at 1/2 β reflection positions. For the ω structure, it possess the crystal structure of the $CuZn_3$ phase and obeys the Blackburn OR ($\{111\}_\beta//\{0001\}_\omega$, $<1\bar{1}0>_\beta//<11\bar{2}0>_\omega$) with the β matrix, giving rise to the additional diffraction spots at 1/3, 2/3 β reflection positions.

(6) Atomic displacement and shuffle systems to realize the structure transition

The η and ω structures formed through a two-stepped atomic displacement. For the η structure,

the first step is the atomic shuffle of each second $\{110\}_\beta$ plane in the $<\bar{1}10>_\beta$ direction to an orthorhombic structure and the second step is to realize the structure change from the transitional orthorhombic structure to the hexagonal structure by mainly a shear on the $\{1\bar{1}2\}_\beta$ plane in the $<\bar{1}11>_\beta$ direction accompanied by small normal strains in the shear plane normal direction ($<112>_\beta$), in the shear direction ($<1\bar{1}1>_\beta$) and in the direction normal to this two ($<110>_\beta$). For the ω structure, the first is an atomic shuffle on each second and third $\{211\}_\beta$ plane in the opposite $\pm[\bar{1}11]_\beta$ directions to an hexagonal structure and the second step is to realize the structure change from the transitional hexagonal structure to the final hexagonal structure by three normal strains in the $<111>_\beta$, $<11\bar{2}>_\beta$ and $<1\bar{1}0>_\beta$ directions.

(7) Origin of concomitant formation of the two hexagonal structures

As the formation of the η structure provokes an volume increase whereas that of the ω structure a volume decrease, the concomitant formation of the ω structures is to cancel out the volume increase of the η structure and to minimize the overall lattice distortion energy.

6.2 Perspectives

The present PhD work thoroughly investigated the α (FCC) to β (BCC) heating phase transformation mechanism and the β to the η/ ω hexagonal structure transition mechanism in an annealed Cu-40%Zn alloys by comprehensively analyzing the microstructure evolution, the crystal defects characters and the phase transformation orientation relationships during these processes. The phase transformation mechanisms revealed in this study could provide new perspectives on further investigations of external field treatment on the Cu-40%Zn alloys which could be summarized as follows:

(1) As different ORs obeyed by the β precipitates depending on the formation site during the heating phase transformation were revealed, the variant selections of the β precipitates under different ORs (the K-S or the N-W) at different formation sites (grain boundary or grain interior) could be further studied.

(2) As the interaction between the types of crystal defects and the β precipitates was confirmed, the roles of crystal defects contribute to other micro processes could be further revealed, such

as the recrystallization process.

(3) Based on the understanding of formation mechanisms of the two hexagonal structures in B_2 β phase in Cu-Zn alloys, the formation mechanism of the two hexagon structures in a BCC matrix could be further studied in many other alloys systems, such as Ti alloys and Zr alloys.

References

[1] Hummel R E, Huntington H B. Electro-and thermo-transport in metals and alloys[M]. New York: Metallurgical Society of AIME, 1977, 326-330.

[2] Geradin M, Rend Comp. Investigation of diffusion and electromigration of hydrogen in palladium and PdAg alloy[J]. Journal of Alloys and Compounds, 1999, 282(1-2):130-136.

[3] Troitskii O A, Spitsyn V I, Stashenko. The influence of an elecreic current on stress relaxation in Crystallizers[J]. Doklady Akademii Nauk SSSR, 1978, 241: 349-352.

[4] Troitskii O A. Pressure shaping by the application of a high energy[J]. Materials Science and Engineering, 1985, 75: 37-50.

[5] Okazaki K, Kagawa M, Conrad H. An evaluation of the contributions of skin, pinch and heating effects on the eletroplastic effect in titanium[J]. Materials Science and Engineering, 1980, 45(6): 109-120.

[6] Troitskii O A, Likhtman V L. The effect of the anisotropy of electron and γ radiation on the deformation of zinc single crystals in the brittle state[J]. Doklady Akademii Nauk SSSR. 1963, 148: 332-336.

[7] Xiao S H, Guo J D, Wu S D, et al. Recrystallization in fatigued copper single crystals under electropulsing[J]. Scripta Materialia, 2002, 46(1): 1-6.

[8] Xu Z, Tang G, Tian S, et al. Research on the engineering application of multiple pulses treatment for recrystallization of fine copper wire[J]. Materials Science and Engineering: A, 2006, 424(1-2): 300-306.

[9] Hu G, Tang G, Zhu Y, et al. Electropulsing induced texture evolution in the recrystallization of Fe-3 Pct Si alloy strip[J]. Metallurgical and Materials Transactions A, 2011, 42(11): 3484-3490.

[10] Samuel E I, Bhowmik A, Qin R. Accelerated spheroidization induced by high intensity electric pulse in a severely deformed eutectoid steel[J]. Journal of Materials Research, 2010, 25(6): 1020-1024.

[11] Hui S, Wang Z J, Gao T J. Effect of high density electropulsing treatment on formability of TC4 titanium alloy sheet[J]. Transactions of Nonferrous Metals Society of China, 2007, 17(1): 87-92.

[12] Wang Z, Song H. Effect of high-density electropulsing on microstructure and mechanical properties of cold-rolled TA15 titanium alloy sheet[J]. Journal of Alloys and Compounds, 2009, 470(1-2): 522-530.

[13] Teng G Q, Chao Y S, Lai Z H, et al. Rapid nanocrystallization from amorphous Fe 78 B 13 Si 9 by high current density electropulsing[J]. Journal of Materials Science Letters, 1995, 14(2): 144-145.

[14] Lai Z H, Conrad H, Teng G Q, et al. Nanocrystallization of amorphous Fe–Si–B alloys using high current density electropulsing[J]. Materials Science and Engineering: A, 2000, 287(2): 238-247.

[15] Shengru Q, Yanli L, Yun L, et al. Damage healing of aluminum alloys by DC electropulsing and evaluation by resistance[J]. Rare Metal Materials and Engineering, 2009, 38(4): 570-573.

[16] Xu Z, Tang G, Ding F, et al. The effect of multiple pulse treatment on the recrystallization behavior of Mg-3Al-1Zn alloy strip[J]. Applied Physics A, 2007, 88(2): 429-433.

[17] Guan L, Tang G, Jiang Y, et al. Texture evolution in cold-rolled AZ31 magnesium alloy during electropulsing treatment[J]. Journal of Alloys and Compounds, 2009, 487(1-2): 309-313.

[18] Takemoto R, Mizubayashi H. Effects of passing electric current on structural relaxation, crystallization and elastic property in amorphous Cu50 Ti50[J]. Acta Metallurgica et Materialia, 1995, 43(4): 1495-1504.

[19] Chao Y, Lai Z, He K, et al. Microstructural relaxation of amorphous alloy Fe79Si7B14 during electropulsing[J]. Materials Science and Engineering: A, 1994, 181: 982-985.

[20] Conrad H. Some effects of an electric field on the plastic deformation of metals and ceramics[J]. Material Research Innovations, 1998, 2(1): 1-8.

[21] Conrad H. Effects of electric current on solid state phase transformations in metals[J]. Materials Science and Engineering: A, 2000, 287(2): 227-237.

[22] Okazaki K, Kagawa M, Conrad H. An evaluation of the contributions of skin, pinch and heating effects to the electroplastic effect in titatnium[J]. Materials Science and Engineering, 1980, 45(2): 109-116.

[23] Sandström R. On recovery of dislocations in subgrains and subgrain coalescence[J]. Acta Metallurgica, 1977, 25(8): 897-904.

[24] To S, YH Z, WB L, et al. Dynamic electropulsing induced phase transformations in a furnace cooled Zn-Al based alloy (ZA22)[J]. Materials Transactions, 2010, 51(11): 1997-2004.

[25] Zhang D, To S, Zhu Y H, et al. Static electropulsing-induced microstructural changes and their effect on the ultra-precision machining of cold-rolled AZ91 alloy[J]. Metallurgical and Materials Transactions A, 2012, 43(4): 1341-1346.

[26] Xu Q, Guan L, Jiang Y, et al. Improved plasticity of Mg–Al–Zn alloy by electropulsing tension[J]. Materials Letters, 2010, 64(9): 1085-1087.

[27] Xu Q, Tang G, Jiang Y, et al. Accumulation and annihilation effects of electropulsing on dynamic recrystallization in magnesium alloy[J]. Materials Science and Engineering: A, 2011, 528(7-8): 3249-3252.

[28] Conrad H, White J, Cao W D, et al. Effect of electric current pulses on fatigue characteristics of polycrystalline copper[J]. Materials Science and Engineering: A, 1991, 145(1): 1-12.

[29] Okazaki K, Kagawa M, Conrad H. An evaluation of the contributions of skin, pinch and heating effects to the electroplastic effect in titatnium[J]. Materials Science and Engineering, 1980, 45(2): 109-116.

[30] Xu Z S, Chen Y X. Effect of electric current on the recrystallization behavior of cold worked α-Ti[J]. Scripta Metallurgica, 1988, 22(2): 187-190.

[31] Conrad H. Effects of electric current on solid state phase transformations in metals[J]. Materials Science and Engineering: A, 2000, 287(2): 227-237.

[32] Koppenaal T J, Simcoe C R. Effect of electric current on aging of an A1-4 PCT CU alloy[J]. Transactions of the Metallurgical Society of AIME, 1963, 227(3): 615-619.

[33] Onodera Y, Hirano K I. The effect of direct electric current on precipitation in a bulk Al-4 wt% Cu alloy[J]. Journal of Materials Science, 1976, 11(5): 809-816.

[34] Dolinsky Y, Elperin T. Thermodynamics of phase transitions in current-carrying conductors[J]. Physical Review B (Condensed Matter), 1993, 47(22): 14778-14785.

[35] Dolinsky Y, Elperin T. Thermodynamics of nucleation in current-carrying conductors[J]. Physical Review B (Condensed Matter), 1994, 50(1): 52-58.

[36] Dolinsky Y, Elperin T. Thermal and electrodynamic effects in melting current-carrying conductors[J]. Journal of Applied Physics, 1996, 80(1): 38-45.

[37] Dolinsky Y, Elperin T. Peculiarities of coexistence of phases with different electric conductivities under the influence of electric current[J]. Material Science and Engineering: A, 2000, 287(2): 219-226.

[38] Dolinsky Y, Elperin T. Phase transitions in fractal clusters in the presense of electric fields[J]. Physical Review B, 2000, 62(3): 12656-12659.

[39] Qin R, Yan H, He G, et al. Exploration on the fabrication of bulk nanocrystalline materials by direct-nanocrystallizing method. Nucleation in Disordered Metallic Media by Electropulsing[J]. Chinese Journal of Material Research, 1995 (9): 219-222.

[40] Qin R, Zhou B. Exploration on the fabrication of bulk nanocrystalline materials by direct-nanocrystallizing method. Theoretical Calculation of Grain size of Metals sondified under Electropulsing[J]. Chinese Journal of Material Research, 1997 (11): 69-72.

[41] Qin R S, Zhou B L. Effect of electric current pulses on grain size in castings[J]. International Journal of Non-Equilibrium Processing, 1998, 11(1): 7-86.

[42] Zhou Y Z, Zhang W, Wang B, et al. Grain refinement and formation of ultrafine-grained microstructure in a low-carbon steel under electropulsing[J]. Journal of Materials Research, 2002, 17(8): 2105-2111.

[43] Zhou Y Z, Zhang W, Sui M L, et al. Formation of a nanostructure in a low-carbon steel under high current density electropulsing[J]. Journal of Materials Research, 2002, 17(5): 921-924.

[44] Zhou Y Z, Guo J D, Zhang W, et al. Influence of electropulsing on nucleation during phase transformation[J]. Journal of Materials Research, 2002, 17(12): 3012-3014.

[45] Wang X L. Mechanisms of microstructural evolution in metallic materials by electric current pulses[D]. Institute of Metal Research Chinese Academy of Sciences, 2007.

[46] Zhang W, Sui M L, Hu K Y, et al. Formation of nanophases in a Cu–Zn alloy under high current density electropulsing[J]. Journal of Materials Research, 2000, 15(10): 2065-2068.

[47] Zhang W, Sui M L, Zhou Y Z, et al. Orientated nanometer-sized fragmentation of TiC particles by electropulsing[J]. Advanced Engineering Materials, 2002, 4(9): 697-700.

[48] Zhang W, Sui M L, Zhou Y Z, et al. Evolution of microstructures in materials induced by electropulsing[J]. Micron, 2003, 34(3-5): 189-198.

[49] Zhou Y Z, Zhang W, Wang B, et al. Ultrafine-grained microstructure in a Cu–Zn alloy produced by electropulsing treatment[J]. Journal of Materials Research, 2003, 18(8): 1991-1997.

[50] Zhou Y Z, Qin R S, Xiao S, et al. Reversing effect of electropulsing on damage of 1045 steel[J]. Journal of Materials Research, 2000, 15(5): 1056-1061.

[51] Zhang W, Zhao W S, Li D X, et al. Martensitic transformation from α-Ti to β-Ti on rapid heating[J]. Applied Physics Letters, 2004, 84(24): 4872-4874.

[52] Zhou Y Z, Zhang W, Guo J D, et al. Diffusive phase transformation in a Cu–Zn alloy under rapid heating by electropulsing[J]. Philosophical Magazine Letters, 2004, 84(5): 341-348.

[53] Du X N, Wang B Q, Guo J D. Formation of nanocrystalline surface of a Cu–Zn alloy under electropulsing surface treatment[J]. Journal of Materials Research, 2007, 22(7): 1947-1953.

[54] Wang X L, Wang Y, Wang Y, et al. Oriented nanotwins induced by electric current pulses in Cu–Zn alloy[J]. Applied Physics Letters, 2007, 91(16): 163112-163112-3.

[55] Dai W B, Wang X L, Zhao L, et al. Formation of nanotwins in cold-rolled Cu-Zn alloy by electric current pulses[J]. Materials Transactions, 2011, 52(11): 2022-2026.

[56] Wang X L, Dai W B, Wang R, et al. Enhanced phase transformation and variant selection by electric current pulses in a Cu–Zn alloy[J]. Journal of Materials Research, 2014, 29(8): 975-980.

[57] Wang X L, Liu M S, Dai W B, et al. Effect of electric current direction on the microstructural evolution and mechanical properties of a cold-rolled Cu–Zn alloy during the phase transformation induced by electric current pulses[J]. Journal of Materials Research, 2015, 30(16): 2500-2507.

[58] Zhou Y Z, Xiao S, Guo J D. Recrystallized microstructure in cold worked brass produced by electropulsing treatment[J]. Materials Letters, 2004, 58(12-13): 1948-1951.

[59] Qin R S. Study on the non-equilibrium transformation by Electropulsing[M]. Chinese Academy of Sciences Institute of Metal Research. 1996.

[60] Jiang Y, Tang G Y, Guan L, et al. Effect of electropulsing treatment on solid solution behavior of an aged Mg alloy AZ61 strip[J]. Journal of Materials Research, 2008, 23(10): 2685-2691.

[61] Jiang Y, Tang G Y, Shek C, et al. On the thermodynamics and kinetics of electropulsing induced dissolution of β-Mg17Al12 phase in an aged Mg–9Al–1Zn alloy[J]. Acta Materialia, 2009, 57(16): 4797-4808.

[62] Zhu Y, To S, Lee W B, et al. Electropulsing-induced phase transformations in a Zn–Al-based alloy[J]. Journal of Materials Research, 2009, 24(8): 2661-2669.

[63] Zhang D, To S, Zhu Y, et al. Dynamic electropulsing induced phase transformations and their effects on single point diamond turning of AZ91 alloy[J]. Journal of Surface Engineered Materials and Advanced Technology, 2012, 2(1): 16-21.

[64] Zhang D, To S, Zhu Y H, et al. Static electropulsing-induced microstructural changes and their effect on the ultra-precision machining of cold-rolled AZ91 alloy[J]. Metallurgical and Materials Transactions A, 2012, 43(4): 1341-1346.

[65] Kelly A, Knowles K M. Crystallography and crystal defects[M]. John Wiley and Sons, 2012.

[66] Bogers A J, Burgers W G. Partial dislocations on the {110} planes in the BCC lattice and the transition of the FCC into the BCC lattice[J]. Acta Metallurgica, 1964, 12(2): 255-261.

[67] Lecroisey F, Pineau A. Martensitic transformations induced by plastic deformation in the Fe-Ni-Cr-C system[J]. Metallurgical and Materials Transactions B, 1972, 3(2): 391-400.

[68] Olson G B, Cohen M. A general mechanism of martensitic nucleation: Part I. General concepts and the FCC→ HCP transformation[J]. Metallurgical Transactions A, 1976, 7(12): 1897-1904.

[69] Olson G B, Cohen M. A general mechanism of martensitic nucleation: Part II. FCC→ BCC and other martensitic transformations[J]. Metallurgical Transactions A, 1976, 7(12): 1905-1914.

[70] Lozano-Perez S, Jenkins M L, Titchmarsh J M. Evidence for deformation-induced transformations of Cu-rich precipitates in an aged FeCu alloy[J]. Philosophical Magazine Letters, 2006, 86(6): 367-374.

[71] Simon T, Kröger A, Somsen C, et al. On the multiplication of dislocations during martensitic transformations in NiTi shape memory alloys[J]. Acta Materialia, 2010, 58(5): 1850-1860.

[72] Fukuda T, Saburi T, Doi K, et al. Nucleation and self-accommodation of the R-phase in Ti–Ni alloys[J]. Materials Transactions, JIM, 1992, 33(3): 271-277.

[73] Denquin A, Naka S. Phase transformation mechanisms involved in two-phase TiAl-based alloys—I. Lambellar structure formation[J]. Acta Materialia, 1996, 44(1): 343-352.

[74] Nakai K, Ono T, Ohtsubo H, et al. Formation process of lamellar γ phase in a Ti-40at. % Al alloy[J]. Materials Transactions, JIM, 1996, 37(4): 813-820.

[75] Mahon G J, Howe J M. Transmission electron microscopy investigation of interfaces in a two-

phase TiAl alloy[J]. Metallurgical Transactions A, 1990, 21(6): 1655-1662.

[76] Inui H, Nakamura A, Oh M H, et al. High-resolution electron microscope study of lamellar boundaries in Ti-rich TiAl polysynthetically twinned crystals[J]. Ultramicroscopy, 1991, 39(1-4): 268-278.

[77] Zhao L, Tangri K. TEM investigation on the interfacial boundaries in as-cast Ti3Al+ TiAl alloy[J]. Acta Metallurgica et Materialia, 1991, 39(10): 2209-2224.

[78] Zhao L, Tangri K. Transmission electron microscopy characterization of interfacial boundaries in heat-treated Ti3Al+TiAl two-phase alloy[J]. Philosophical Magazine A, 1991, 64(2): 361-386.

[79] Singh S R, Howe J M. High-resolution electron microscopy of γ-α_2 interfaces in titanium aluminide[J]. Philosophical Magazine A, 1992, 66(5): 739-771.

[80] Yang Y S, Wu S K, Wang J Y. A study by high-resolution electron microscopy of an $\alpha_2+\gamma$ two-phase Ti–40 at. % Al alloy[J]. Philosophical Magazine A, 1993, 67(2): 463-478.

[81] Ibarra A, Caillard D, San Juan J, et al. Martensite nucleation on dislocations in Cu–Al–Ni shape memory alloys[J]. Applied Physics Letters, 2007, 90(10): 101907.

[82] Furuhara T, Maki T. Variant selection in heterogeneous nucleation on defects in diffusional phase transformation and precipitation[J]. Materials Science and Engineering: A, 2001, 312(1-2): 145-154.

[83] Hilliard J E, Cahn J W. On the nature of the interface between a solid metal and its melt[J]. Acta Metallurgica, 1958, 6(12): 772-774.

[84] Thomas G, Nutting J. Mechanism of Phase Transformations in Metals, Inst[J]. MetiUs Mon, 1956, 18: 57-61.

[85] Lee T H, Kim S D, Ha H Y, et al. Screw dislocation driven martensitic nucleation: A step toward consilience of deformation scenario in fcc materials[J]. Acta Materialia, 2019, 174: 342-350.

[86] Knapp H, Dehlinger U. Mechanik und Kinetik der diffusionslosen Martensitbildung[J]. Acta Metallurgica, 1956, 4(3): 289-297.

[87] Harry T, Bacon D J. Computer simulation of the core structure of the screw dislocation in α-iron containing copper precipitates: I. structure in the matrix and a precipitate[J]. Acta Materialia, 2002, 50(1): 195-208.

[88] Bacon D J, Osetsky Y N. Modelling dislocation–obstacle interactions in metals exposed to an irradiation environment[J]. Materials Science and Engineering: A, 2005, 400-401: 353-361.

[89] Bacon D J, Osetsky Y N. Hardening due to copper precipitates in α-iron studied by atomic-scale modelling[J]. Journal of Nuclear Materials, 2004, 329-333: 1233-1237.

[90] Nam S W. Investigation of a2 Phase Transformation mechanism under the interaction of

dislocation with lamellar interface[C]//International Conference on Structural and Functional Intermetallics. 2000.

[91] Korzhenevskii A L, Bausch R, Schmitz R. Kinetic wetting of a moving planar defect by a new phase[J]. Physical Review Letters, 2003, 91(23): 236101.

[92] Boulbitch A A, Toledano P. Phase nucleation of elastic defects in crystals undergoing a phase transition[J]. Physical Review Letters, 1998, 81(4): 838.

[93] Reid A C E, Olson G B, Moran B. Dislocations in nonlinear nonlocal media: martensitic embryo formation[J]. Phase Transitions, 1999, 69(3): 309-328.

[94] Zhang W, Jin Y M, Khachaturyan A G. Phase field microelasticity modeling of heterogeneous nucleation and growth in martensitic alloys[J]. Acta Materialia, 2007, 55(2): 565-574.

[95] Shim J H, Cho Y W, Kwon S C, et al. Screw dislocation assisted martensitic transformation of a bcc Cu precipitate in bcc Fe[J]. Applied Physics Letters, 2007, 90(2): 021906-021906-3.

[96] Nishiyama Z, Kajiwara S. Electron microscope study of the crystal structure of the martensite in a copper-aluminium alloy[J]. Japanese Journal of Applied Physics, 1962, 2(8): 478-486.

[97] Harry T, Bacon D J. Computer simulation of the core structure of the <111> screw dislocation in α-iron containing copper precipitates: I. structure in the matrix and a precipitate[J]. Acta Materialia, 2002, 50(1): 195-208.

[98] Osetsky Y N, Bacon D J, Mohles V. Atomic modelling of strengthening mechanisms due to voids and copper precipitates in α-iron[J]. Philosophical Magazine, 2003, 83(31-34): 3623-3641.

[99] Ibarra A, San Juan J, Bocanegra E H, et al. Evolution of microstructure and thermomechanical properties during superelastic compression cycling in Cu–Al–Ni single crystals[J]. Acta Materialia, 2007, 55(14): 4789-4798.

[100] Levitas V I, Javanbakht M. Phase field approach to interaction of phase transformation and dislocation evolution[J]. Applied Physics Letters, 2013, 102(25): 251904.

[101] Sort J, Nogués J, Suriñach S, et al. Microstructural aspects of the hcp-fcc allotropic phase transformation induced in cobalt by ball milling[J]. Philosophical Magazine, 2003, 83(4): 439-455.

[102] Louidi S, Bentayeb F-Z, Tebib J, et al. Stacking faults and phase transformations study in ball milled $Co_{100-x}Cr_x$ alloys[J]. Materials Chemistry and Physics, 2012, 132(2-3): 761-765.

[103] Hoshino Y, Nakamura S, Ishikawa N, et al. In-situ observation of γ= ε transformation in Fe-Mn-Si shape memory alloys[C]//Materials Science Forum. Trans Tech Publications, 1990, 56: 643-648.

[104] Christian J W. A theory of the transformation in pure cobalt[J]. Proceedings of the Royal Society of London. Series A. Mathematical and Physical Sciences, 1951, 206(1084): 51-64.

[105] Xu Z. Thermodynamics of the martensitic transformation Beta(Gamma)-> Epsilon[J]. Acta. Metall. Sin., 1980, 16(4): 430-434.

[106] Olson G B, Cohen M. A general mechanism of martensitic nucleation: Part I. General concepts and the FCC→ HCP transformation[J]. Metallurgical Transactions A, 1976, 7(12): 1897-1904.

[107] Mahajan S, Green M L, Brasen D. A model for the FCC→ HCP transformation, its applications, and experimental evidence[J]. Metallurgical Transactions A, 1977, 8(2): 283-293.

[108] Smith T M, Esser B D, Good B, et al. Segregation and phase transformations along superlattice intrinsic stacking faults in Ni-Based superalloys[J]. Metallurgical and Materials Transactions A, 2018, 49(9): 4186-4198.

[109] Wang M, Li Z, Raabe D. In-situ SEM observation of phase transformation and twinning mechanisms in an interstitial high-entropy alloy[J]. Acta Materialia, 2018, 147: 236-246.

[110] Olson G B, Cohen M. A general mechanism of martensitic nucleation: Part II. FCC→ BCC and other martensitic transformations[J]. Metallurgical Transactions A, 1976, 7(12): 1905-1914.

[111] Remy L, Pineau A. Twinning and strain-induced FCC→HCP transformation in the FeMnCrC system[J]. Materials Science and Engineering, 1977, 28(1): 99-107.

[112] Olson G B, Cohen M. A mechanism for the strain-induced nucleation of martensitic transformations[J]. Journal of the Less Common Metals, 1972, 28(1): 107-118.

[113] Bogers A J, Burgers W G. Partial dislocations on the {110} planes in the BCC lattice and the transition of the FCC into the BCC lattice[J]. Acta Metallurgica, 1964, 12(2): 255-261.

[114] Lecroisey F, Pineau A. Martensitic transformations induced by plastic deformation in the Fe-Ni-Cr-C system[J]. Metallurgical and Materials Transactions B, 1972, 3(2): 391-400.

[115] Curtze S, Kuokkala V T, Oikari A, et al. Thermodynamic modeling of the stacking fault energy of austenitic steels[J]. Acta Materialia, 2011, 59(3): 1068-1076.

[116] Bogers A J, Burgers W G. Partial dislocations on the {110} planes in the BCC lattice and the transition of the FCC into the BCC lattice[J]. Acta Metallurgica, 1964, 12(2): 255-261.

[117] Olson G B, Cohen M. A mechanism for the strain-induced nucleation of martensitic transformations[J]. Journal of the Less Common Metals, 1972, 28(1): 107-118.

[118] Christian J W. A theory of the transformation in pure cobalt[J]. Proceedings of the Royal Society of London. Series A. Mathematical and Physical Sciences, 1951, 206(1084): 51-64.

[119] Anantharaman T R, Christian J W. The existence of a macroscopic shear in the transformation in cobalt[J]. The London, Edinburgh, and Dublin Philosophical Magazine and Journal of Science, 1952, 43(347): 1338-1342.

[120] Votava E. Electron microscopic investigation of the phase transformation of thin cobalt samples[J]. Acta Metallurgica, 1960, 8(12): 901-904.

[121] Waitz T, Karnthaler H P. The fcc to hcp martensitic phase transformation in CoNi studied by TEM and AFM methods[J]. Acta Materialia, 1997, 45(2): 837-847.

[122] Olson G B, Owen W S. Martensite[M]. Materials Park, OH: ASM International, 1992.

[123] Hitzenberger C, Karnthaler H P. Weak-beam TEM study of the hcp to fcc martensitic phase transformation lamellae in CoNi[J]. Philosophical Magazine A, 1991, 64(1): 151-163.

[124] Aufrecht J, Leineweber A, Duppel V, et al. Transformation–dislocation dipoles in Laves phases: A high-resolution transmission electron microscopy analysis[J]. Journal of Materials Research, 2010, 25(10): 1983-1991.

[125] Seeger A. Versetzungen und allotrope umwandlungen[J]. Zeitschrift Fur Metallkunde, 1953, 44(6): 247-253.

[126] Surendra K, Ankit K, Malte L, et al. On the diffusive phase transformation mechanism assisted by extended dislocations during creep of a single crystal CoNi-based superalloy[J]. Acta Materialia, 2018, 155: 362-371.

[127] Bollmann W. On the phase transformation of cobalt[J]. Acta Metallurgica, 1961, 9(10): 972-975.

[128] Mahajan S, Green M L, Brasen D. A model for the FCC→ HCP transformation, its applications, and experimental evidence[J]. Metallurgical Transactions A, 1977, 8(2): 283-293.

[129] Johnson R T, Dragsdorf R D. The martensitic transformation in cobalt[J]. Journal of Applied Physics, 1967, 38(2): 618-626.

[130] Fujita H, Ueda S. Stacking faults and fcc (γ)→ hcp (ϵ) transformation in 188-type stainless steel[J]. Acta Metallurgica, 1972, 20(5): 759-767.

[131] Asgari S, El-Danaf E, Shaji E, et al. The secondary hardening phenomenon in strain-hardened MP35N alloy[J]. Acta Materialia, 1998, 46(16): 5795-5806.

[132] Hsiung L M, Lassila D H. Shock-induced omega phase in tantalum[J]. Scripta Materialia, 1998, 38(9): 1371-1376.

[133] Hsiung L M, Lassila D H. Shock-induced deformation twinning and omega transformation in tantalum and tantalum–tungsten alloys[J]. Acta Materialia, 2000, 48(20): 4851-4865.

[134] Lai M J, Tasan C C, Raabe D. Deformation mechanism of ω-enriched Ti–Nb-based gum metal: Dislocation channeling and deformation induced ω–β transformation[J]. Acta Materialia, 2015, 100: 290-300.

[135] Niu C, LaRosa C R, Miao J, et al. Magnetically-driven phase transformation strengthening in high entropy alloys[J]. Nature Communications, 2018, 9(1): 1363.

[136] Suzuki H. Mechanisms for the development of martensitic transformation of a face-centred cubic structure into a body-centred tetragonal structure[J]. Science reports of the Research

Institutes, Tohoku University. Ser. A, Physics, chemistry and metallurgy, 1954, 6: 30-49.

[137] Lecroisey F, Pineau A. Martensitic transformations induced by plastic deformation in the Fe-Ni-Cr-C system[J]. Metallurgical and Materials Transactions B, 1972, 3(2): 391-400.

[138] Dash S, Brown N. Nucleation and growth of martensite in Fe-32.3%Ni alloy[J]. Acta Metallurgica, 1966, 14(5): 595-603.

[139] Lagneborgj R. The martensite transformation in 18%Cr-8%Ni steels[J]. Acta Metallurgica, 1964, 12(7): 823-843.

[140] Magee L. Phase Transformations[M]. American Society for Metals, Metals Park, 1970, 115.

[141] Burgers W G, Klostermann J A. Influence of the direction of deformation on the transition of austenite into martensite[J]. Acta Metallurgica, 1965, 13(5): 568-572.

[142] Shimizu K, Oka M, Wayman C M. The association of martensite platelets with austenite stacking faults in an Fe-8Cr-1C alloy[J]. Acta Metallurgica, 1970, 18(9): 1005-1011.

[143] Lai M J, Li T, Raabe D. ω phase acts as a switch between dislocation channeling and joint twinning-and transformation-induced plasticity in a metastable β titanium alloy[J]. Acta Materialia, 2018, 151: 67-77.

[144] Jonas J J, Aranas Jr C, Fall A, et al. Transformation softening in three titanium alloys[J]. Materials and Design, 2017, 113: 305-310.

[145] Li T, Kent D, Sha G, et al. New insights into the phase transformations to isothermal ω and ω-assisted α in near β-Ti alloys[J]. Acta Materialia, 2016, 106: 353-366.

[146] Zheng Y, Williams R E A, Nag S, et al. The effect of alloy composition on instabilities in the β phase of titanium alloys[J]. Scripta Materialia, 2016, 116: 49-52.

[147] Fan J, Li J, Zhang Y, et al. The origin of striation in the metastable β phase of titanium alloys observed by transmission electron microscopy[J]. Journal of Applied Crystallography, 2017, 50(3): 795-804.

[148] Lai M J, Tasan C C, Zhang J, et al. Origin of shear induced β to ω transition in Ti–Nb-based alloys[J]. Acta Materialia, 2015, 92: 55-63.

[149] Xing H, Sun J. Mechanical twinning and omega transition by <111>{112} shear in a metastable β titanium alloy[J]. Applied Physics Letters, 2008, 93(3): 031908.

[150] De Fontaine D, Paton N E, Williams J C. The omega phase transformation in titanium alloys as an example of displacement controlled reactions[J]. Acta Metallurgica, 1971, 19(11): 1153-1162.

[151] Bennett J M, Barnard J S, Stone H J, et al. On the nature of the omega tri-layer periodicity in rapidly cooled Ti-15Mo[J]. Scripta Materialia, 2015, 107: 79-82.

[152] Bönisch M, Waitz T, Calin M, et al. Tailoring the Bain strain of martensitic transformations in

TiNb alloys by controlling the Nb content[J]. International Journal of Plasticity, 2016, 85: 190-202.

[153] Bönisch M, Calin M, Waitz T, et al. Thermal stability and phase transformations of martensitic Ti–Nb alloys[J]. Science and Technology of Advanced Materials, 2013, 14(5): 055004.

[154] Bönisch M, Calin M, Giebeler L, et al. Composition-dependent magnitude of atomic shuffles in Ti–Nb martensites[J]. Journal of Applied Crystallography, 2014, 47(4): 1374-1379.

[155] Wanjara P, Dalgaard E, Gholipour J, et al. Effect of pre-and post-weld heat treatments on linear friction welded Ti-5553[J]. Metallurgical and Materials Transactions A, 2014, 45(11): 5138-5157.

[156] Devaraj A, Nag S, Srinivasan R, et al. Experimental evidence of concurrent compositional and structural instabilities leading to ω precipitation in titanium–molybdenum alloys[J]. Acta Materialia, 2012, 60(2): 596-609.

[157] Sukedai E, Kitano Y, Ohnishi A. Investigation of initial structures of aged ω-phase crystals in β-titanium alloys using high resolution electron microscopy[J]. Micron, 1997, 28(4): 269-277.

[158] Jones N G, Dashwood R J, Jackson M, et al. β Phase decomposition in Ti–5Al–5Mo–5V–3Cr[J]. Acta Materialia, 2009, 57(13): 3830-3839.

[159] Furuhara T, Maki T, Makino T. Microstructure control by thermomechanical processing in β-Ti–15–3 alloy[J]. Journal of Materials Processing Technology, 2001, 117(3): 318-323.

[160] Nag S, Devaraj A, Srinivasan R, et al. Novel mixed-mode phase transition involving a composition-dependent displacive component[J]. Physical Review Letters, 2011, 106(24): 245701.

[161] Jeong H W, Yoo Y S, Lee Y T, et al. Elastic softening behavior of Ti–Nb single crystal near martensitic transformation temperature[J]. Journal of Applied Physics, 2010, 108(6): 063515.

[162] Sun J, Yao Q, Xing H, et al. Elastic properties of β, α″ and ω metastable phases in Ti–Nb alloy from first-principles[J]. Journal of physics: condensed matter, 2007, 19(48): 486215.

[163] Burgers W G. On the process of transition of the cubic-body-centered modification into the hexagonal-close-packed modification of zirconium[J]. Physica, 1934, 1(7-12): 561-586.

[164] De Fontaine D. Mechanical instabilities in the bcc lattice and the beta to omega phase transformation[J]. Acta Metallurgica, 1970, 18(2): 275-279.

[165] Nagasawa A, Nakanishi N, Enami K. The nature of special-mode softening and the mechanism of martensitic phase transition in β-phase alloys[J]. Philosophical Magazine A, 1981, 43(6): 1345-1357.

[166] Prasetyo A, Reynaud F, Warlimont H. Omega phase in quenched β brass and its relation to elastic anomalies[J]. Acta Metallurgica, 1976, 24(11): 1009-1016.

[167] Srinivasa Rao S, Anantharaman T R. The occurrence of a hexagonal phase in quenched 60: 40 brass[J]. Naturwissenschaften, 1961, 48(23): 712-712.

[168] Suryanarayana C, Anantharaman T R. Formation of hexagonal phases in α–β brasses[J]. Metallurgical and Materials Transactions B, 1971, 2(11): 3237-3237.

[169] Troiani H E, Pelegrina J L, Ahlers M. The bcc-to-fcc phase transformation during dezincification of β-phase Cu-Zn[J]. Philosophical Magazine A, 1998, 78(6): 1253-1267.

[170] Troiani H E, Tolley A, Ahlers M. High-resolution transmission electron microscopy study of small hexagonal precipitates produced during the dezincification of β-CuZn[J]. Philosophical Magazine A, 2000, 80(6): 1379-1391.

[171] Troiani H E, Ahlers M. The formation of an intermediate structure during the dezincification of β Cu–Zn alloys and its relevance for the martensitic transformation[J]. Materials Science and Engineering: A, 1999, 273: 200-203.

[172] Baruj A, Granada M, Larochette P A, et al. Primordial hexagonal phase formation during the bcc dezincification of the β Cu–Zn single crystalline surface: Matrix instabilization and transformation path[J]. Journal of Alloys and Compounds, 2009, 481(1-2): 129-134.

[173] Gong W, Tomota Y, Adachi Y, et al. Effects of ausforming temperature on bainite transformation, microstructure and variant selection in nanobainite steel[J]. Acta Materialia, 2013, 61(11): 4142-4154.

[174] Yoshinaga N, Inoue H, Kawasaki K, et al. Factors affecting texture memory appearing through α→ γ→ α transformation in IF steels[J]. Materials Transactions, 2007, 48(8): 2036-2042.

[175] He Y, Jonas J J, Godet S, et al. Crystallographic features of theγ-to-α transformation in a Nb-added transformation-induced plasticity steel[J]. Metallurgical and Materials Transactions A, 2006, 37(9): 2641-2653.

[176] Song H Y, Liu H T, Wang G D, et al. formation of widmanstätten austenite in strip cast grain-oriented silicon steel[J]. Metallurgical and Materials Transactions A, 2017, 48(4): 1959-1968.

[177] Bracke L, Kestens L, Penning J. Transformation mechanism of α′-martensite in an austenitic Fe–Mn–C–N alloy[J]. Scripta Materialia, 2007, 57(5): 385-388.

[178] Watanabe T, Obara K, Tsurekawa S, et al. A mechanism of plane matching boundary-assisted α/γ phase transformation in Fe–Cr alloy based on in-situ observations[J]. Zeitschrift für Metallkunde, 2005, 96(10): 1196-1203.

[179] Kestens L, Petrov R, Houbaert Y. Orientation selective martensite transformation in an Fe-28Ni alloy[J]. ISIJ international, 2003, 43(9): 1444-1452.

[180] Stanford N, Bate P S. Crystallographic variant selection in α–β brass[J]. Acta Materialia, 2005, 53(3): 859-867.

[181] Brückner G, Köntges A, Gottstein G. Microstructure and texture development during the phase

transformation in an Fe-Ni-Co-Ti shape memory alloy[J]. Steel Research, 1999, 70(4-5): 188-192.

[182] He Y, Godet S, Jacques P J, et al. Crystallographic relations between face-and body-centred cubic crystals formed under near-equilibrium conditions: Observations from the Gibeon meteorite[J]. Acta Materialia, 2006, 54(5): 1323-1334.

[183] Van Bohemen S M C, Kamp A, Petrov R H, et al. Nucleation and variant selection of secondary α plates in a β Ti alloy[J]. Acta Materialia, 2008, 56(20): 5907-5914.

[184] Cao G H, Russell A M, Oertel C G, et al. Microstructural evolution of TiAl-based alloys deformed by high-pressure torsion[J]. Acta Materialia, 2015, 98: 103-112.

[185] Bönisch M, Calin M, Giebeler L, et al. Composition-dependent magnitude of atomic shuffles in Ti–Nb martensites[J]. Journal of Applied Crystallography, 2014, 47(4): 1374-1379.

[186] Bönisch M, Waitz T, Calin M, et al. Tailoring the Bain strain of martensitic transformations in TiNb alloys by controlling the Nb content[J]. International Journal of Plasticity, 2016, 85: 190-202.

[187] Li Z B, Zhang Y D, Esling C, et al. Determination of the orientation relationship between austenite and incommensurate 7M modulated martensite in Ni–Mn–Ga alloys[J]. Acta Materialia, 2011, 59(7): 2762-2772.

[188] Li Z B, Yang B, Zhang Y D, et al. Crystallographic insights into the intermartensitic transformation in Ni–Mn–Ga alloys[J]. Acta Materialia, 2014, 74: 9-17.

[189] De Knijf D, Nguyen-Minh T, Petrov R H, et al. Orientation dependence of the martensite transformation in a quenched and partitioned steel subjected to uniaxial tension[J]. Journal of Applied Crystallography, 2014, 47(4): 1261-1266.

[190] Jonas J J, He Y, Godet S. The possible role of partial dislocations in facilitating transformations of the Nishiyama–Wassermann type[J]. Scripta Materialia, 2005, 52(3): 175-179.

[191] Wittridge N J, Jonas J J, Root J H. A dislocation-based model for variant selection during the γ-to-α′ transformation[J]. Metallurgical and Materials Transactions A, 2001, 32(4): 889.

[192] Bunge H J, Weiss W, Klein H, et al. Orientation relationship of Widmannstätten plates in an iron meteorite measured with high-energy synchrotron radiation[J]. Journal of Applied Crystallography, 2003, 36(1): 137-140.

[193] Luo C P, Weatherly G C. The invariant line and precipitation in a Ni-45 wt% Cr alloy[J]. Acta Metallurgica, 1987, 35(8): 1963-1972.

[194] Bullough R, Bilby B A. Continuous distributions of dislocations: Surface dislocations and the crystallography of martensitic transformations[J]. Proceedings of the Physical Society. Section B, 1956, 69(12): 1276.

[195] Ameyama K, Maki T. Precipitation of austenite at deformation twin boundaries of ferrite in two

phase stainless steel[J]. Scripta Metallurgica et Materialia, 1990, 24(1): 173-178.

[196] Alloying: understanding the basics[M]. ASM international, 2001.

[197] Li S, Imai H, Atsumi H, et al. Characteristics of high strength extruded BS40CrFeSn alloy prepared by spark plasma sintering and hot pressing[J]. Journal of Alloys and Compounds, 2010, 493(1-2): 128-133.

[198] Li S, Imai H, Kondoh K. Microstructure, phase transformation, precipitation behavior and mechanical properties of P/M Cu40Zn–1.0wt%Ti brass alloy via spark plasma sintering and hot extrusion[J]. Journal of Materials Science and Technology, 2013, 29(11): 1018-1024.

[199] Peng K, Su L, Shaw L L, et al. Grain refinement and crack prevention in constrained groove pressing of two-phase Cu–Zn alloys[J]. Scripta Materialia, 2007, 56(11): 987-990.

[200] Zhang Z J, Duan Q Q, An X H, et al. Microstructure and mechanical properties of Cu and Cu–Zn alloys produced by equal channel angular pressing[J]. Materials Science and Engineering: A, 2011, 528(12): 4259-4267.

[201] Cornelis I, Wayman C M. Phase transformations in metastable β′ CuZn alloys—I. Martensitic transformations[J]. Acta Metallurgica, 1974, 22(3): 291-300.

[202] Cornelis I, Wayman C M. Phase transformations in metastable β′ CuZn alloys—II. Isothermal transformations[J]. Acta Metallurgica, 1974, 22(3): 301-311.

[203] Dames G J, Kallend J S, Morris P P. The quantitative prediction of transformation textures[J]. Acta Metallurgica, 1976, 24(2): 159-172.

[204] Yasuda H Y, Sakata T, Umakoshi Y. Variant selection in transformation texture from the β to α phase in Cu–40 mass% Zn alloy[J]. Acta Materialia, 1999, 47: 1923-1933.

[205] Sakata T, Yasuda H Y, Umakoshi Y. Formation process of transformation texture from the β to α phase in Cu-42mass% Zn alloy[J]. Scripta materialia, 2000, 5(43): 411-416.

[206] Stanford N, Bate P S. Crystallographic variant selection in α–β brass[J]. Acta Materialia, 2005, 53(3): 859-867.

[207] Troiani H E, Pelegrina J L, Ahlers M. The bcc-to-fcc phase transformation during dezincification of β-phase Cu-Zn[J]. Philosophical Magazine A, 1998, 78(6): 1253-1267.

[208] Hu H, Smith C S. The formation of low-energy interfaces during grain growth in alpha and alpha-beta brasses[J]. Acta Metallurgica, 1956, 4(6): 638-646.

[209] Mapelli C, Venturini R. Dependence of the mechanical properties of an α/β brass on the microstructural features induced by hot extrusion[J]. Scripta Materialia, 2006, 54(6): 1169-1173.

[210] Troiani H E, Baruj A. In situ optical microscopy study of a phase transformation induced by the dezincification of beta Cu–Zn[J]. Materials Science and Engineering: A, 2007, 454: 441-445.

[211] Hsu Y F, Wang W H. The effect of α1 plates on the martensitic transformation and shape

memory effect in a β Cu–Zn alloy[J]. Materials Characterization, 2001, 46(5): 381-388.

[212] Baruj A, Larochette P A, Sommadossi S, et al. Surface phase transformation induced by the dezincification of a beta Cu–Zn alloy on highly deformed systems[J]. Applied Surface Science, 2007, 254(1): 72-75.

[213] Liu M S, Wang X L, Zhao X. Effect of high-density electric current pulses on precipitation and mechanical properties of a Cu–Zn alloy[J]. Materials Science and Technology, 2017, 33(12): 1411-1416.

[214] Fundenberger J J, Morawiec A, Bouzy E, et al. Polycrystal orientation maps from TEM[J]. Ultramicroscopy, 2003, 96(2): 127-137.

[215] Morawiec A, Fundenberger J J, Bouzy E, et al. EP–a program for determination of crystallite orientations from TEM Kikuchi and CBED diffraction patterns[J]. Journal of Applied Crystallography, 2002, 35(2): 287-287.

[216] Bunge H J, Esling C, Muller J. The role of the inversion centre in texture analysis[J]. Journal of Applied Crystallography, 1980, 13(6): 544-554.

[217] Bunge H J, Esling C, Muller J. The influence of crystal and sample symmetries on the orientation distribution function of the crystallites in polycrystalline materials[J]. Acta Crystallographica Section A: Crystal Physics, Diffraction, Theoretical and General Crystallography, 1981, 37(6): 889-899.

[218] Zhang Y, Wang S, Esling C, et al. A method to identify dislocations in a known crystal structure by transmission electron microscopy[J]. Journal of Applied Crystallography, 2011, 44(6): 1164-1168.

[219] Crystal Maker software, http://www.crystalmaker.com/

[220] Tanner L E. Diffraction contrast from elastic shear strains due to coherent phases[J]. The Philosophical Magazine: A Journal of Theoretical Experimental and Applied Physics, 1966, 14(127): 111-130.

[221] Beausir B, Fundenberger J J, Université de Lorraine - Metz, 2017, ATEX - software, Analysis Tools for Electron and X-ray diffraction , www.atex-software.eu.

Publication list

I: Publications in international journals

[1] **Meishuai Liu**, Yudong Zhang, Xinli Wang, Benoit Beausir, Xiang Zhao, Liang Zuo, Claude Esling. Crystal defect associated selection of phase transformation orientation relationships (ORs). Acta Materialia, Vol. 152, pp 315-326, 2018.

[2] **Meishuai Liu**, Yudong Zhang, Xinli Wang, Benoit Beausir, Maolin Liu, Xiang Zhao, Liang Zuo, Claude Esling. Microstructure and Crystallography of β Phase formed through Electric Current Pulse (ECP) treatment in cold-rolled Cu-40%Zn Alloy. Materials Science Forum, Vol. 941, pp 1117-1122, 2018.

[3] **Meishuai Liu**, Xinli Wang, Xiang Zhao. Effect of high-density electric current pulses on precipitation and mechanical properties of a Cu–Zn alloy. Materials Science and Technology, Vol. 33, pp 1411-1416, 2017.

[4] **Meishuai Liu**, Nan Wu, Xinli Wang, Xiang Zhao. Effect of refined precipitated phase induced by electric current pulses on the mechanical properties in a Cu-Zn alloy. Book of the International Workshop Articles, 2015.

[5] Xinli Wang, **Meishuai Liu**, Nan Wu, Wenbin Dai, Xiang Zhao. Microstructural evolution of AZ31 under the application of high density electric current pulses. Materials Science Forum, Vol. 879, pp 2055-2060, 2016.

[6] Xinli Wang, **Meishuai Liu**, Wenbin Dai, Nan Wu, Xiang Zhao. Effect of electric current direction on the microstructural evolution and mechanical properties of a cold-rolled Cu-Zn alloy during the phase transformation induced by electric current pulses. Journal of Materials Research. Vol. 30, pp 2500-2507, 2015.

[7] **Meishuai Liu**, Yudong Zhang, Xinli Wang, Benoit Beausir, Xiang Zhao, Liang Zuo, Claude Esling. Formation mechanism of nano-sized ω and η structures in B_2 β phase in ECP treated Cu-40%Zn alloy. Under review.

II: Contributions to International Conferences

[1] **Meishuai Liu**, Yudong Zhang, Xinli Wang, Xiang Zhao. Microstructure and Crystallography of β Phase formed through Electric Current Pulse (ECP) treatment in cold-rolled Cu-40Zn Alloy. Poster presented in the THERMEC 2018, International Conference on Processing and Manufacturing of Advanced Materials and received a *Student Grant*, France, July 2018.

[2] **Meishuai Liu**. Attended in the 11th European Symposium on "Martensitic Transformations" as volunteer student. France, Aug. 2018.

[3] **Meishuai Liu**, Xinli Wang, Xiang Zhao. Effect of refined precipitated phase induced by electric current pulses on the mechanical properties in a Cu-Zn alloy. Oral presented in the 6th International Seminar on "Effect of external influences on the strength and plasticity of metals and alloys". Russia, Sep. 2015.

[4] Xinli Wang, **Meishuai Liu**, Xiang Zhao. Attended in the 5th International Seminar on "Effect of external influences on the strength and plasticity of metals and alloys". China, Sep. 2014.

Acknowledgements

My PhD work is completed at the Laboratoire d'Étude des Microstructures et de Mécanique des Matériaux (LEM3), UMR CNRS 7239, Université de Lorraine, Metz, France, and the Key Laboratory for Anisotropy and Texture of Materials (ATM), Northeastern University, Shenyang, China. It is my honor to study with the colleagues of the laboratories in France and in China. I would like to express my sincere thanks to my colleagues and my friends who help me in my study and in my live.

This work is supported by the China Scholarship Council (Grant No.201606080054), the National Natural Science Foundation of China (Grant No. 51471047) and the Fundamental Research Funds for the Central Universities of China (Grant No. N130418001).

I sincerely gratitude to my supervisors, Dr. Yudong ZHANG and Dr. Benoît Beausir at Université de Lorraine, France, and Professor Xiang Zhao and Associate Professor Xinli Wang at Northeastern University, China, for their constant guidance and selfless help in my PhD work and in my daily life. I have benefited greatly from their academic aptitude. I would like to express my deepest gratitude to Professor Claude ESLING for his help in my research work and in my daily life in France.

I would like to thank all the jury members for taking time out of their schedules to achieve my dissertation defense, and special gratitude to Professor Werner Skrotzki and Professor Zhanjie Wang to review my dissertation and provide the suggestions and comments.

I would like to express my thanks to all the staffs and students at the laboratory of LEM3 in France and at the laboratory in China. They shared their experiences with me and offered help to my PhD work, especially to Mr. Jérôme SLOWENSKY, Ms. Auriane MANDRELLI, Ms. Jacqueline DECKER, Ms. Nathalie KASPRZAK, Ms. Anne-martine BLUM, Ms. Arlette JACQUIERRE, Dr. Haile YAN, Dr. Bo YANG, Dr. Zongbin LI, Dr. Chunyang ZHANG, Dr. Shun XU, Dr. Cai CHEN, Dr. Yajun ZHAO, Dr. Jing WEN, Dr. Naifu ZOU, Dr. Ke HUA, Mr. Hailong SHI, Ms. Xiaomeng LIU, Ms. Qian WANG, Ms. Fengming QIANG, Mr. Zhenzhuang LI, Ms. Shuang JIANG, Dr. Na XIAO, Dr. Yan WU, Ms. Ning ZHANG. Special thanks to Ms. Wei SI and Ms. Pengru ZHAO for their

patiently help in my daily life.

Last but not least, I would like to express my deep love and gratitude to my parents and to my brother for their generous love and support to me in my life.